UNIVERSITY OF OSLO
Department of Physics

Modeling of a resistive contact RF-MEMS switch fabricated using DRIE

Master Thesis

Per Gisle Dalsjø

1 December 2006

Acknowledgements

First and foremost I would like to thank Geir Uri Jensen for taking the time to supervise me on this thesis. I have especially appreciated his critical comments and our discussions. I am also very grateful to the others at SINTEF MiNaLab who have helped me along the way, and especially Anders Hanneborg who introduced me to the exciting field of MEMS. I am looking forward to continuing the cooperation when I start work at FFI.

I would also like to thank the Physical Electronics group at MiNaLab for the good working environment and converting me into a LaTeX fan.

A special thanks to all my friends who get me away from all the scientific stuff and help me reset my brain, my parents for their support and my brother for proof reading this thesis.

1 December, 2006

Per Gisle Dalsjø

Summary

In recent years there has been a dramatic increase in the number of wireless applications in both commercial and markets such as defense. Radio Frequency (RF) Micro Electro Mechanical Systems (MEMS) with its low power consumption and excellent RF characteristics has a potential of creating new, flexible and cost efficient wireless systems for these markets.

In this thesis a set of methods to analyze the characteristics of a novel series resistive contact switch concept are presented. The switch concept is based on the fabrication of a laterally actuated cantilever beam using Deep Reactive Ion Etching (DRIE) and a conformal metal deposition process.

The majority of methods presented are analytical but different modules of CoventorWare® and especially ARCHITECT have also been used for verification and supporting analyses.

The switch concept offers the possibility to fabricate complex switch geometries with few process steps and potentially no stiction problems during release. The resulting cross-section of the fabricated cantilever beam consists of a single crystal silicon core with a metal cladding layer. This makes the beam less sensitive to residual stress in the metal film. The layered beam can also potentially improve characteristics such as switching time. However, the fabrication process has several disadvantages that for instance apply unfortunate limitations to certain geometric dimensions of the switch.

As a result of the lateral actuation configuration, the switch can be incorporated into a coplanar transmission line structure. This offers the possibility to design a switch with good matching to its surrounding circuitry and improved high frequency characteristics.

The switch concept is also compared to the more traditional layered surface micromachining approach.

A chapter presenting a model to estimate the contact resistance is also include, which also functions as an introduction into the complex contact physics for resistive contact MEMS switches.

Contents

1 Introduction **1**
- 1.1 General introduction to MEMS . . . 1
- 1.2 Objectives and methodology . . . 2
- 1.3 Structure of this thesis . . . 4

2 RF MEMS switches **5**
- 2.1 Background . . . 5
- 2.2 Switch configurations . . . 6
- 2.3 Applications . . . 9
  - 2.3.1 Mobile phones . . . 10
  - 2.3.2 Phase shifters . . . 11

3 Fabrication **15**
- 3.1 Introduction . . . 15
- 3.2 Process steps . . . 15
  - 3.2.1 Reactive Ion Etching . . . 15
  - 3.2.2 Physical Vapor Deposition . . . 16
- 3.3 Fabrication of switch concept . . . 17
  - 3.3.1 SOI based process . . . 17
  - 3.3.2 Silicon on glass based process . . . 18
  - 3.3.3 Discussion . . . 20
- 3.4 Layered surface micromachining . . . 22

4 Contact modeling **25**
- 4.1 Introduction . . . 25
- 4.2 Modeling approach . . . 26
- 4.3 Material deformation . . . 26
  - 4.3.1 Elastic model . . . 27
  - 4.3.2 Plastic model . . . 28
  - 4.3.3 Elastic-Plastic . . . 29
  - 4.3.4 Multiple asperities . . . 30

4.4 Contact resistance . . . 30
4.5 Parameter sensitivity . . . 35
4.6 Discussion . . . 40

5 Modeling of beam mechanics 41
5.1 Introduction . . . 41
5.2 Modeling approach . . . 41
5.2.1 Analytical method . . . 41
5.2.2 System level simulations . . . 43
5.2.3 Finite Element Modeling . . . 43
5.3 Modeling methods . . . 47
5.3.1 Electrostatic Actuation . . . 47
5.3.2 Beam deflection and equivalent spring constant . . . 50
5.3.3 Effective Young's modulus for a layered cross-section . 52
5.3.4 Pull-In voltage . . . 56
5.3.5 Restoring force . . . 57
5.3.6 Contact force . . . 57
5.3.7 Resonance frequency . . . 61
5.3.8 Damping and quality factor . . . 63
5.3.9 Switching time . . . 68

6 RF modeling 75
6.1 Introduction . . . 75
6.2 Modeling approach . . . 77
6.2.1 Analytical methods . . . 78
6.2.2 Numerical methods . . . 78
6.3 Equivalent circuit . . . 78
6.3.1 Beam series resistance . . . 80
6.3.2 Series capacitance . . . 80
6.3.3 Shunt coupling capacitance . . . 84
6.3.4 Inductance . . . 85
6.3.5 Contact resistance . . . 88
6.4 S-Parameters . . . 88
6.4.1 Return loss . . . 89
6.4.2 Isolation . . . 90
6.4.3 Insertion loss . . . 91

7 Design example 95
7.1 Introduction . . . 95
7.2 Calculations . . . 96

8 Comparison of two switch concepts **103**
8.1 Introduction 103
8.2 Fabrication 103
8.3 Mechanical properties 104
8.4 RF properties 106

9 Conclusion **109**

10 Future work **111**

Appendices **112**

A MATLAB code **113**
A.1 Contact modeling 113
A.2 S-Parameter modeling 117

List of Tables

4.1 The properties of the Au contact used in this chapter. Values from [12, 19] 28
4.2 The number of asperities in contact at a contact force, $F_c = 100\ \mu N$. 39
4.3 Summary of values for contact resistance for different contact metals. Contact force is $F_c \approx 100 \mu N$. 40

5.1 The characteristics of the cantilever beam used in this chapter. Any variations from this is commented in the respective calculations. 42

6.1 Capacitance between two electrodes. 85
6.2 Calculated distributed inductance. ($t_m = 0.6\ \mu m$) 87
6.3 The values of the equivalent circuit components used in this chapter. Any variations from this are commented in the respective calculations. 90

7.1 Performance requirement for the SMIDA RF MEMS switch. . 95
7.2 Geometry of two designs. 97
7.3 Estimated values for the equivalent circuit parameters. 100

8.1 Cross-section used as an example to demonstrate advantages of using a layered cross-section 105

List of Figures

1.1 Example of Micro Electro Mechanical Systems. (From [34]) . . 2
1.2 SEM micrograph of a laterally actuated series switch fabricated in the device layer of an SOI wafer. G=Ground, S=Signal (From [11]) 3

2.1 Approximate theoretical frequency range of RF MEMS switches [37] 7
2.2 A series metal (resistive) contact switch and a shunt capacitive switch. (From [33]) 8
2.3 Simplified equivalent circuit for two switch configurations. . . 8
2.4 Multiband switch for various mobile standards/ frequency bands. (From [28]) 11
2.5 Principle of a phased array antenna using phase shifters. (From [22]) 12
2.6 Schematic of switched line phase designs. (From [37]) 13

3.1 SEM micrograph of trenches fabricated using DRIE. (From [41]) 16
3.2 SOI fabrication process of a lateral series switch. (From [11]) . 19
3.3 Lateral and longitudinal cross-section of structure fabricated using process DRIE and glass substrate. (From [14]) 20
3.4 SEM image showing the undercut after HF vapor etching of the exposed oxide layer. (From [31]) 20
3.5 Deposition of conformal metal layer. (Dimensions not to scale) 21
3.6 Shadow mask used in a commercial process. (From [31]) . . . 22
3.7 SEM micrograph of a defined contact. (From [16]) 23
3.8 Surface micromachining of a serial metal contact switch. (From [37]) 24

4.1 SEM micrograph of a MEMS switch contact. (From [19]) . . . 26
4.2 A rough surface contacting a smooth surface. 27
4.3 Contact radius of a single Au asperity. 30

4.4 Modeled contact radius of the individual asperities for the contact specified in table 4.1. 31
4.5 Illustration of the Maxwell spreading resistance (a) and Sharvin resistance (b). 32
4.6 The two $\Gamma(K_n)$ functions used in litterature. 33
4.7 The calculated contact resistance for a single asperity. 34
4.8 Illustration of the multi asperity (left) and the single effective asperity (right) contact area models. (From [18]) 35
4.9 Modeled contact resistance for the Au specified in table 4.1. . 36
4.10 Modeled contact resistance for MEMS switch contact force range. 36
4.11 Calculated contact force for two values of R. 37
4.12 Calculated contact force for two values of H. 38
4.13 Calculated contact force for two different surface topologies. . 39

5.1 SEM micrograph of a microswitch showing the principle of variable cross section. The fixed end of the double cantilever beam is on the right.[19] 42
5.2 Illustration of the different modulus of CoventorWare 44
5.3 System model schematic. 45
5.4 Process file used for FEM analysis. 46
5.5 The additional elements introduced by the thin metal film (a). Different mesh densities for beam and electrode (b) 47
5.6 Electrostatic actuated cantilever beam with two cross-sections. 48
5.7 Schematic of an electrostatic actuator with a supporting spring force. 49
5.8 Schematic view of the beam. 51
5.9 Cross section of a single crystal beam with a Au cladding layer. 53
5.10 Implementation of an equivalent moment of inertia [9]. 53
5.11 Cross-section of a symmetrical three layered beam. The cross-section has been rotated 90° compared to figure 5.9. 54
5.12 Calculated pull-in voltage V_{pi}. 56
5.13 Calculated restoring force F_R. 57
5.14 Cantilever beam in contact with the lower contact. 58
5.15 Calculated contact force F_{cmax}. $(t_m = 0)$ 60
5.16 Calculated actuation voltage V_{cmax}. $(t_m = 0)$ 61
5.17 The contact force F_{Con} as a function of the actuation voltage. $(t_m = 0)$ 62
5.18 Schematic view of the structure used to estimate the effective mass m_{eff} 62

5.19 The calculated resonance frequency using analytical method and Architect 63
5.20 The effective viscosity, μ_{eff}, and the Knudsen number, K_n, as a function of gap height, g. 65
5.21 Calculated quality factor Q using eq. (5.43) (Method # 1) and eq. (5.43) (Method # 2). ($h_1 = 3\mu m$, $t_m = 0\mu m$) 66
5.22 Correction function for the damping coefficient given a large displacement 67
5.23 The small displacement quality factor Q_{nom} (eq. 5.45) and the corrected quality factor Q_{eff}. 67
5.24 A laterally actuated RF MEMS switch fabricated in a SOI process 68
5.25 A schematic view of a simplified model of a electrostatic actuated switch 69
5.26 Actuation time simulated using eq.(5.48) and Architect. 70
5.27 Simulated actuation time for three effective beam widths, w_{eff}. ($V_a = 1.5V_{pi}$) 71
5.28 Simulated release time. 72
5.29 Simulated release time for two different effective beam widths, w_{eff}. 73

6.1 Coplanar waveguide (a) and a coplanar strip transmission line (b). (From [3]) 76
6.2 The concept of the series switch incorperated in a CPW transmission line. 76
6.3 Current distribution for CPW, CPS and microstrip transmission lines. 77
6.4 Refinement of the volume of the conductor. (From [8]) 79
6.5 Equivalet circuit of the switch. 79
6.6 Skin depth of Au. 81
6.7 Cross-section of the beam showing current density. 81
6.8 The distributed contact resistance as a function of frequency.($w =$ 35 μm, $t_m = 0.6$ μm) 82
6.9 Cantilever beam tip and surrounding structure. 83
6.10 Series capacitance as function of the overlap l_0. 83
6.11 Series capacitance as function of the distance, X_{end} between the beam tip and main signal line. 84
6.12 Total beam inductance. 86
6.13 Cross-section variation of the cantilever beam. 87
6.14 Cantilever beam with reduced mass. 87
6.15 Two-port S-parameter network. (From [30]) 88

6.16 Calculated down state return loss, S_{11}, for three inductance values. 91
6.17 Calculated isolation, S_{S1}, for various series capacitances, C_s . 92
6.18 Calculated insertion loss, S_{21}, for various contact resistances, R_c. 93

7.1 Resonance frequency for the two designs given in table 7.2. . . 97
7.2 Pull-in voltage and equivalent spring force for the two designs given in table 7.2. 98
7.3 Contact forces for two different electrode lengths, l_2. 99
7.4 Calculated actuation and release time. 99
7.5 Beam series resistance for the two beam designs. 100
7.6 Calculated isolation for design #1 for three series capacitance values. 101
7.7 Calculated insertion loss for for design #1 for three contact resistance values. 102
7.8 Calculated return loss for design #1 for a range of inductance values. 102

8.1 SEM-picture of a tri-stable single pole double throw switch with three beams actuated using curved electrodes. (From [14]) 106

Chapter 1

Introduction

1.1 General introduction to MEMS

The term MEMS is an acronym for Micro Electro Mechanical Systems. The first MEMS devices developed were pressure sensors, accelerometers and other sensor devices. Today the term has grown and refers to devices such as ink-dispensing nozzles used in printer heads, micro mirrors for displays and projectors and micro fluidic devices used in biochemical analysis, to mention a few.

MEMS devices are fabricated using lithography-based processes, initially borrowed from the IC industry, that have been enhanced and specialized into fabrication techniques such as bulk- and surface micromachining. Bulk micromachining make use of wet or dry etching techniques to form membranes, trenches and other structures in a substrate. The anisotropic etching rates for i.e. single crystal silicon are often utilized. Surface micromachining creates structures on a substrate by depositing thin films of sacrificial layers and structural layers. Deposition techniques such as Chemical Vapor Deposition (CVD), Physical Vapor Deposition (PVD) are used in addition to etching techniques to pattern layers and remove sacrificial layers.

Traditionally MEMS devices are fabricated using materials such as single crystal silicon, polysilicon, silicon dioxide and silicon nitride, in addition to different metal films. However, devices using a number of other materials have also been demonstrated. Polymers, for example, are used for disposable biochemical MEMS devices.

Applications range through many fields of engineering and science. As a result, branches of MEMS with a specific focus have emerged (Figure 1.1). Radio Frequency (RF) MEMS focuses on solving many of the intriguing problems related to microwave applications. The last five years there have

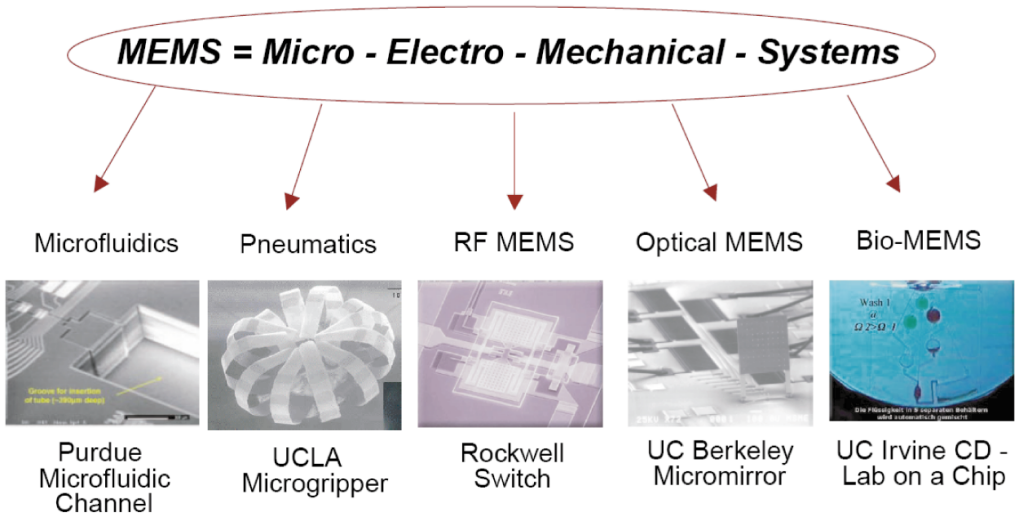

Figure 1.1: Example of Micro Electro Mechanical Systems. (From [34])

been a dramatic increase in the number of wireless applications. Current and future requirements for these applications are the driving force for the development of RF MEMS.

The focus of the RF MEMS research is on several key components and areas. These components include switches, variable capacitors, inductors, micromechanical filters etc. The successful development of these components will allow the design of new, flexible and cost efficient wireless systems.

The most mature RF MEMS component is the switch. The first MEMS switch developed for microwave frequencies was demonstrated in the early 90s [37]. Since then a number of different switches have been demonstrated with excellent RF performance. However, due to cost and reliability problems very few of these switches have made it to the market.

1.2 Objectives and methodology

In recent years, several laterally actuated switches fabricated using Deep Reactive Ion Etching (DRIE) and a conformal metal deposition process, have been presented [11, 14, 16]. This fabrication concept offers the possibility of fabricating complex switch geometries using only a few process steps. Figure 1.2 shows an example of such a switch and the concept of the fabrication process.

The objective of this thesis is to present a set of methods to analyze

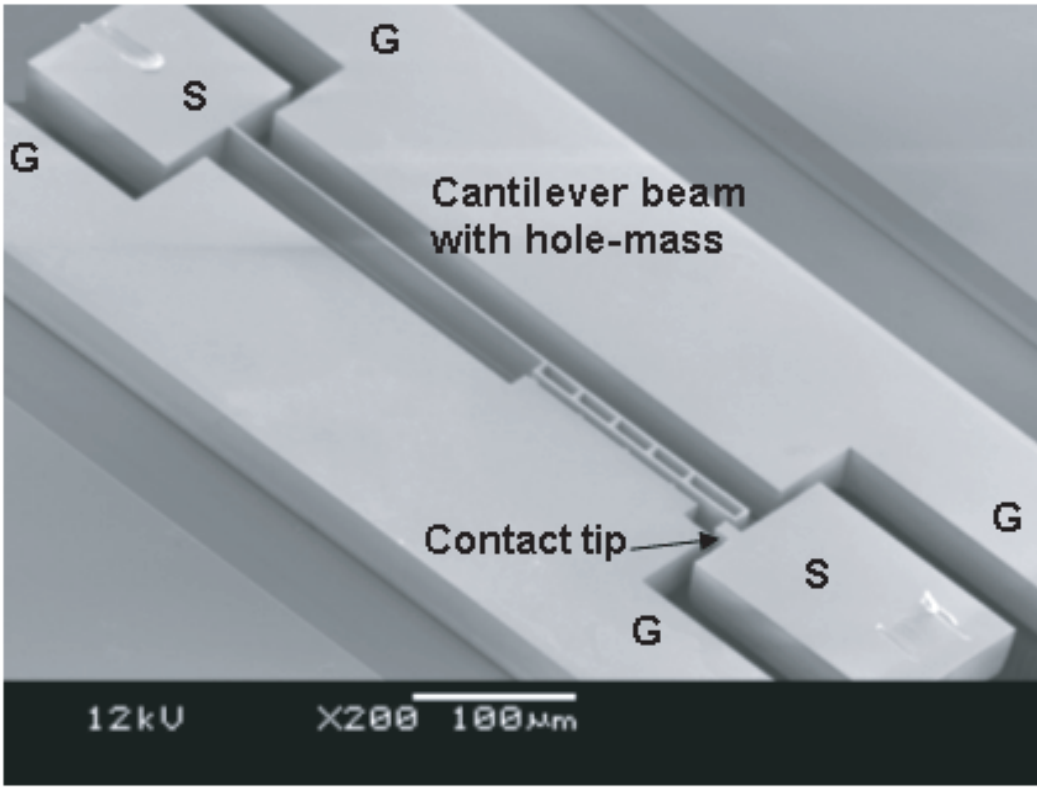

Figure 1.2: SEM micrograph of a laterally actuated series switch fabricated in the device layer of an SOI wafer. G=Ground, S=Signal (From [11])

the characteristics of a laterally actuated series resistive contact RF MEMS switch, fabricated using DRIE and a conformal metal deposition process. The majority of the presented methods will be analytical methods but different modules of CoventorWare® [27] will also be used for verification and supporting analyses.

By using these analytical models the parameter dependency of the different design characteristics will be investigated. An example of one design approach will also be included to provide an overview of how the different design characteristics are related.

To understand the switch concept, the fabrication process will be presented. In addition, the most important processes steps will be described, in order to discuss the limitations and advantages of the fabrication process.

Based on the presented material, the general characteristics of the DRIE fabricated switch will be compared to the more traditional switch concept fabricated using layered surface micromachining.

The contact of the switch is of paramount importance for the performance and reliability of a series resistive switch. A chapter is therefore dedicated to the contact physics and the modeling of the contact resistance.

1.3 Structure of this thesis

The structure and depth of this thesis allows for a natural progression through the thesis.

A general introduction to RF MEMS switches is given in Chapter 2. The thesis continues by describing the fabrication process implemented.

Chapter 4 discusses the importance of the switch contact and presents an analytical method to estimate the contact resistance. The modeling section continues by presenting methods to model the beam mechanics. Similarly chapter 6 presents methods to analyze the RF characteristics of the switch.

Chapter 7 is a design example meant to give an overview of how the different design characteristics are related.

Finally, chapter 8 compares the implemented design concept to the more traditional approach, followed by conclusions and suggestions for future work.

Chapter 2

RF MEMS switches

2.1 Background

The fundamental task of a switch is to complete or break a conduction path. However, at RF frequencies ($\sim> 500MHz$) this simple task becomes more complicated due to the electromagnetic wave nature of the signal. In order for the switch to perform its fundamental task it must be designed for the specific frequency band and match the characteristic impedance of the system. Failure to do so will introduce losses, reflections of the signal or transmission of signal when it is not intended.

In 2001 there were around 30 companies working on developing RF MEMS devices [37]. Among these were some of the large consumer electronic companies. The research has been fueled by the very promising performance of the devices at high frequencies and in 2005 it was reported that around 60 companies where developing RF MEMS components [4].

The PIN diode and the GaAs MOSFET are the typical solid state counterparts to the RF MEMS switch. As the frequency increases past a few gigahertz the performance of these solid state devices drop [22]. For low to medium power applications at a few GHz, the isolation of RF MEMS switches is superior to solid state devices. The low power consumption, low insertion loss and linearity of the devices are other parameters that motivate the development of RF MEMS switches. As a result of this unmatched performance, RF MEMS shows promise for new complex communication and radar systems [34].

The power handling capabilities of RF MEMS devices are typically lower than solid state devices. However, advances have been made in this area the last couple of years [38].

The main challenges for RF MEMS are related to the actuation voltage,

switching time, reliability and the packaging of the devices.

As long as the actuation voltage is within $20 - 60V$, CMOS voltage up-converters can be easily be implemented to raise the $3V$, typically available in a circuit [39]. However, for a number of designs the actuation voltages may exceed this level requiring additional measures.

The typical switching times for electrostatic actuated RF MEMS switches are in the range $1 - 300\ \mu s$, compared to $1 - 100\ ns$ for their solid state counterparts, the PIN diode and MOSFET [22, 37]. Reducing the switching time is an area of active research in order to satisfy specific RF applications. However, for some applications the available switching time is sufficient.

The reliability of a switch is generally indicated by the number of cycles that can be achieved before the switch fails, and is a complex function of power transferred, contact material/ dielectric used etc. Large improvements have been made in this area to meet the requirement of the applications.

The packaging of the device affects both the performance and reliability. As a result, special packaging techniques need to be developed for the specific device. This increases the price of the RF MEMS switch substantially [37].

2.2 Switch configurations

Numerous configurations of a RF MEMS switch are possible depending on actuations mechanism, contact type and the circuit configuration. Electrostatic actuation is the most popular actuation mechanism [37]. This is due to its virtually zero power consumption, small size and the shortest switching time (compared to the other actuation methods). Other actuation mechanisms are thermal, piezoelectric and magnetostatic, which are typically implemented in niche applications. Thermal actuation, for example, can produce relatively high contact forces and therefore low contact resistance, but consumes power [29, 37].

In the electrical circuit the switch can be implemented either in a series or shunt configuration and can have either a resistive contact or a capacitive contact. This results in four different switch configurations. The approximate theoretical frequency bands for these configurations are given in figure 2.1.

About 80 % the switches demonstrated so far are either an electrostatically actuated capacitive contact shunt design or an electrostatically actuated metal (resistive) contact series switch [33]. This is due to the achievable frequency band of operation and other advantages and limitations related to the different switch configurations. The capacitive series switch design, for instance, has typically a large contact area and a low restoring force. As a result the design is prone to not release from the downstate due to adhesion

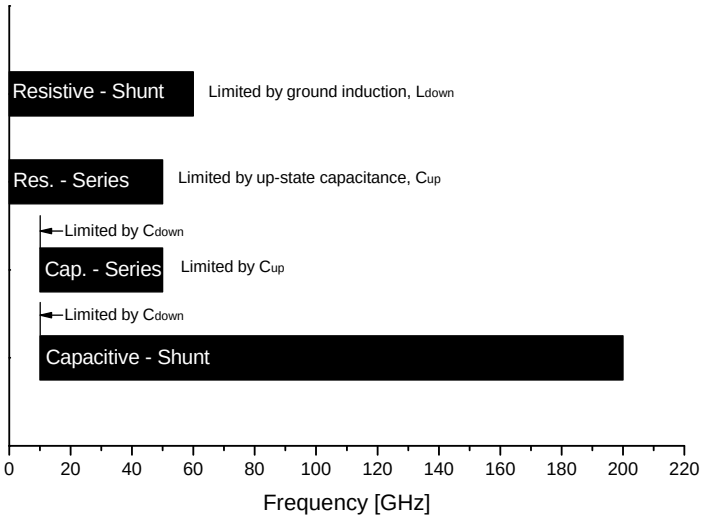

Figure 2.1: Approximate theoretical frequency range of RF MEMS switches [37]

forces at the contact.

Figure 2.2 shows a sketch of an electrostatically activated capacitive shunt switch and a metal contact series switch. Only these two switch configurations will be discussed here. For an overview of different switch configuration consult [33, 37].

The series switch is typically a normally-off switch[1] and uses a cantilever beam or membrane to complete the signal transmission line in the downstate. The configuration shown in figure 2.2 uses a metal contact bar on the tip of the cantilever to complete the transmission line. However, in another widely used configuration, the cantilever itself is the transmission line and the signal propagates the length of the cantilever when the switch is transmitting.

Figure 2.3 shows the equivalent circuit for the two states of the two switches. At high frequencies the capacitive coupling, due to the up-state capacitance, C_{up}, drastically reduces the switch isolation. As a result, the metal contact switch has an upper operation frequency. The switch has however no lower operation frequency and can be used for DC signals.

The shunt switch is a normally-on switch and often implemented with a coplanar wave guide (CPW) transmission line (Figure 2.2). In the downstate the shunt switch reroutes the signal. This is only possible if down state

[1]Normally on switches have also been demonstrated [34]

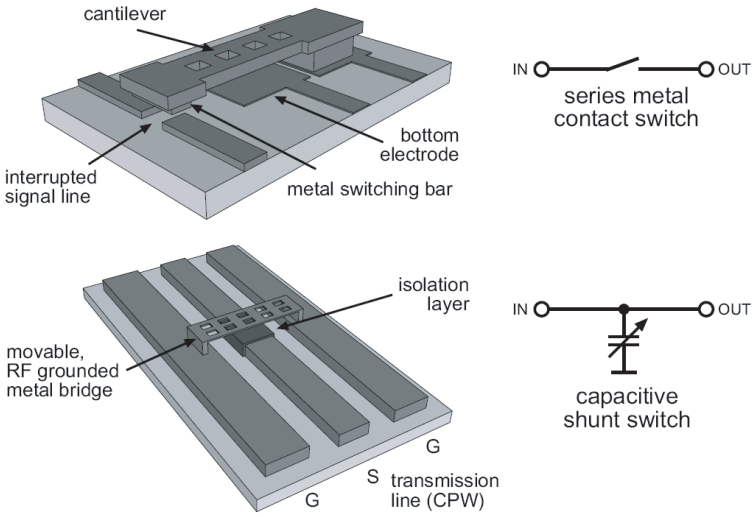

Figure 2.2: A series metal (resistive) contact switch and a shunt capacitive switch. (From [33])

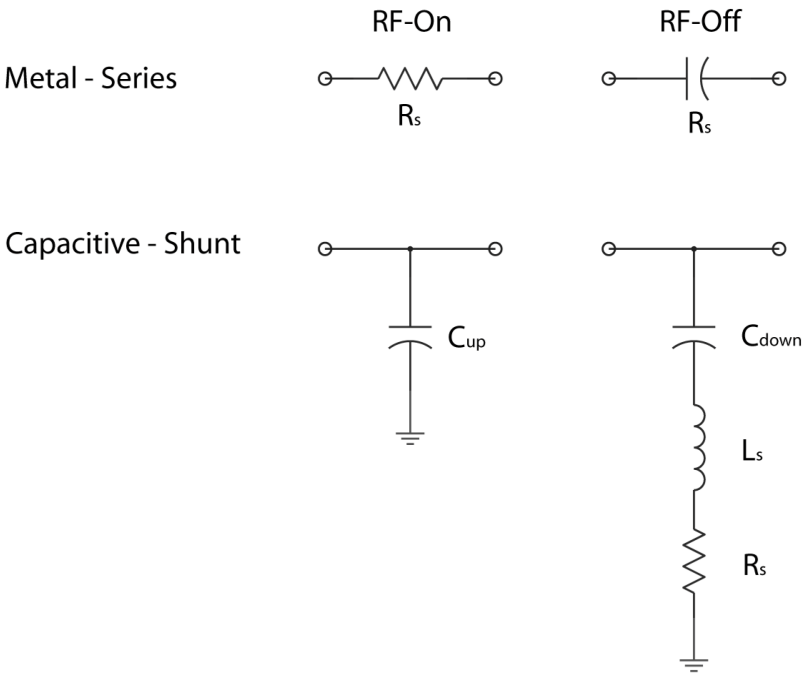

Figure 2.3: Simplified equivalent circuit for two switch configurations.

capacitance, C_{down} is sufficiently large. The shunt switch therefore has a lower frequency limit. The bridge/ membrane is actuated either by applying a DC bias on the signal line or by using separate actuation electrodes on either sides of the signal line.

Comparing the switch characteristics of the two generic configurations is difficult since the characteristics of a switch are closely related to the specific design. There are however some general characteristics that are typical for the two switches.

The main failure mechanisms for metal contact RF MEMS switches are related to the contact. The contact physics is complex and depend on a number of parameter. An important parameter is the power transmitted [37]. For low power levels a metal contact switch typically fails due to changes to the contact surface, resulting in increased resistance. For higher power levels the failure mechanisms change and are related to the increased temperature at the contact. This results in material transfer between the contacts and microwelding, which can cause the switch to remain in the down position even after the actuation voltage is removed.

For capacitive switches the main failure mechanisms are related to charging of the dielectric [37] (Figure 2.2). This can result in the bridge remaining in the downstate after the actuation voltage is removed or the bridge releasing once contact is made with the dielectric. The bridge can also become insensitive to the actuation voltage, remaining in the up-state.

As a result, the reliability of both switch configurations is reduced if the power transferred is increased. However, solving the dielectric charging problem, the capacitive switch is said to be more suited for medium ($10 - 100\ mW$) to high ($> 100\ mW$) power levels [37], partially due to the larger contact area.

2.3 Applications

The use of RF MEMS in wireless applications is motivated by the low power consumption, low loss and high isolation characteristics of RF MEMS devices. Because of these characteristics, the performance and functionality of a large number of wireless applications can be improved. In this section two different applications for RF MEMS will be discussed.

The mobile phone is an example of a consumer electronics application fabricated in large quantities for a cost competitive marked. The phase shifter, on the other hand, sees applications typically in the defense and aerospace industry where i.e. the acceptable cost is much higher.

2.3.1 Mobile phones

Today's mobile phones are not just phones but incorporate a number of additional functions e.g. cameras, music players, Internet browser etc. With this increased functionality, the requirements for data transfer are changed dramatically. In addition to the basic mobile phone data transfer standards, e.g. GSM, 3G, a number of other wireless standards must be supported. The communication between devices is achieved using e.g. Bluetooth and Zigbee, while local connection to Internet can be performed using i.e. a WLAN protocol. All this functionality must be achieved without increasing the size of the mobile phone, maintaining the battery capacity and price.

A miniaturization of the different radio modules is seen as part of the solution. In this regard, RF MEMS components are predicted to replace some of the bulky off-chip components currently used, such as inductors and crystals. Ideally these RF MEMS components should be fully integrated with the integrated circuit.

The different radio modules will also need to converge into one or a few reconfigurable radios [13]. By incorporating RF MEMS components, passive networks such as impedance-matching networks and tank circuits can be made reconfigurable. Figure 2.4 shows a band switch used to switch the antenna between several mobile phone frequency bands. The band switch module could also include matching circuitry for the different frequency bands. In such a configuration the switches are additional components in the signal path. The low loss characteristics of a RF MEMS switch makes an ideal candidate [28].

The RF MEMS switches have also been considered for T/R (Transceive and Receive) switching, due to the excellent RF characteristics. However, the cost of RF MEMS, with its current packaging techniques, is too high for this application [28, 36]. In addition, the number of switching cycles required is in the order $10^8 - 10^9$ [28]. This has been demonstrated using RF MEMS [38] but not with continuous current condition (hot switching). The required switching time is in the tens of nanoseconds, which is also much faster than published RF MEMS devices.

The typical frequency range for the above mentioned data transfer standards is 890 MHz to 5.9 GHz [28]. As a result, only metal contact switches are acceptable for this application (Figure 2.1). The required actuation voltage is a drawback for the RF MEMS switch. Voltage up-converters from the typical 3 V available to $20-60$ V can easily be implemented [39], but results in higher cost and increased required circuit area.

The mobile phone market is potentially the largest market for RF MEMS [13]. The integration of RF MEMS in mobile phones is however held back

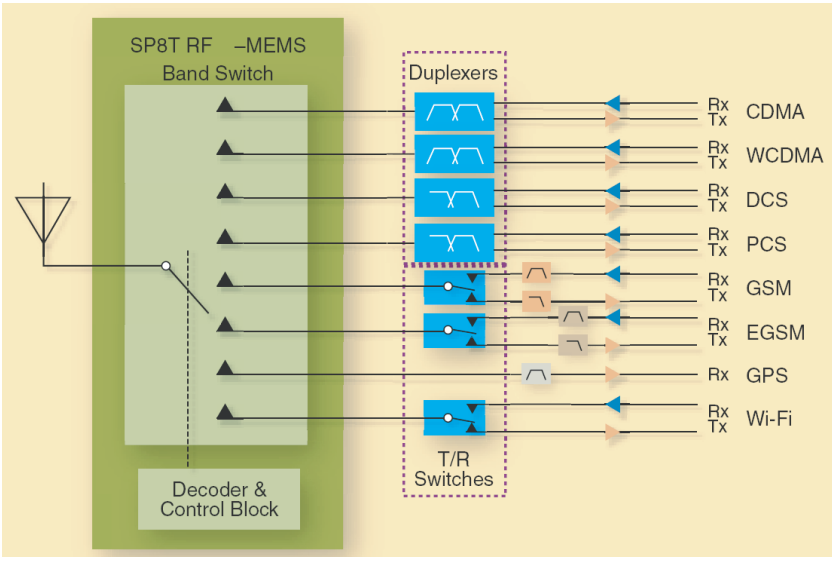

Figure 2.4: Multiband switch for various mobile standards/ frequency bands. (From [28])

somewhat due to the different fabrication processes used. The mainstream fabrication process for mobile phones is CMOS, while RF MEMS utilizes specialized processes and non-CMOS compatible metals i.e. Au. Devices fabricated using CMOS processes have been demonstrated and is an active field of research [38]. There are also several methods to integrate RF MEMS components with CMOS. This includes, flip chip mounting and fabrication of the RF MEMS device on an already CMOS processed wafer (post-CMOS) [13, 37].

2.3.2 Phase shifters

Another application that has received a lot of attention is the MEMS based phase shifter [13, 22, 37]. Phase shifters are essential in phase array antennas used in telecommunications and radar systems, found in defense, aerospace and satellite applications.

Figure 2.5 shows the principle of a phased array antenna using phase shifters. By controlling the phase of the signal at each antenna element, the antenna beam can be shaped and directed without moving the antenna system. The phase shifters control the phase by changing the effective path of the transmission line.

The effective path of the transmission line can be altered using several methods. The switch line type phase shifter (Figure 2.6) controls the phase

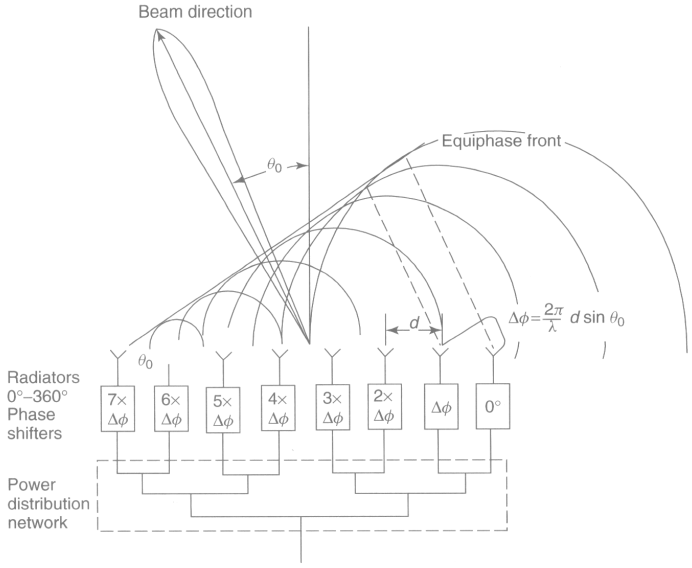

Figure 2.5: Principle of a phased array antenna using phase shifters. (From [22])

by including or bypassing a transmission line section that introduces a given delay e.g. $180°, 90°, 45°$. This is an example of a digital phase shifter. An analog phase shifter however does not have a finite resolution. In this case the phase is changed by controlling the permeability, μ (changes the phase velocity, v_p), of a section of the transmission line.

There are several types of phase shifters each with their pros and cons [22, 39]. The ferrite phase shifter can either be digital or analog. It has excellent RF characteristics but requires manual tuning and has high power consumption. The use of FETs results in digital phase shifters that can be easily fabricated and integrated together with the antenna. The power consumption is also low but the insertion loss is high. Replacing the FETs with PIN diodes results in a lower insertion loss but higher power consumption.

MEMS phase shifters combines excellent RF characteristics with the best properties of the PIN and FET based phase shifters. The resulting low mass, low power consumption and excellent RF characteristics are very interesting e.g. aerospace and satellite applications [13].

Both metal contact series switches and capacitive shunt switches are being used in MEMS phase shifters [37]. However, for high frequencies and some phase shifter types capacitive shunt switches are needed.

For phase shifters, the fabrication methods used can be highly specialized

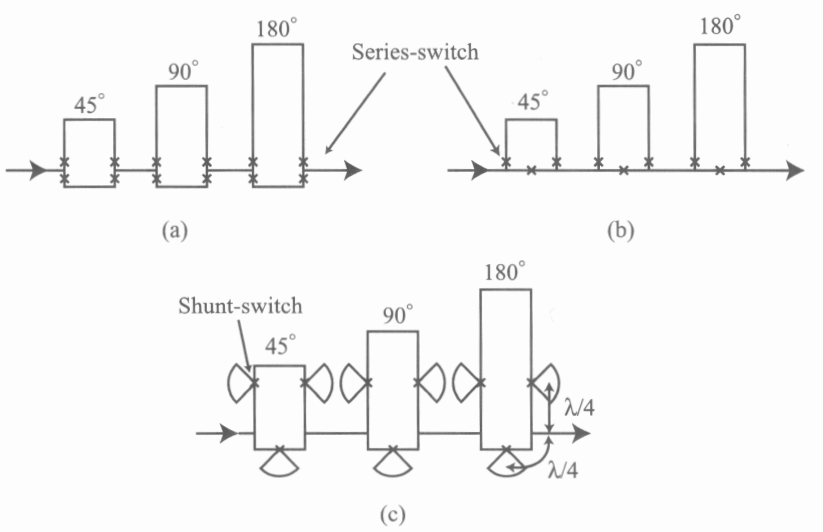

Figure 2.6: Schematic of switched line phase designs. (From [37])

due to the higher acceptable cost and smaller production series. The typical high actuation voltage $(20 - 90V)$ of RF MEMS switches is also easily met in these applications [38].

Chapter 3

Fabrication

3.1 Introduction

To understand the switch concept to be analyzed in this thesis, it is important to understand the fabrication process. In this chapter, two fabrication processes used to fabricate laterally actuated RF MEMS switches [11, 14, 16] are presented and discussed. In order to do this effectively the fundamentals of the essential process steps are also presented.

The more traditional layered surface micromachining process will also be presented briefly, as the two switch concepts will be compared later in the thesis.

3.2 Process steps

3.2.1 Reactive Ion Etching

Reactive Ion Etching (RIE) is a highly anisotropic etching technique with high selectivity [5, 41]. The wafer to be etched is placed in a low pressure (10^{-3} - 10^{-2} torr) chamber where gases are introduced (Chlorine or Flour-based) and an RF source is used to create a plasma. The resulting etch consist of two mechanisms. At the wafer surface, ions react with the material resulting in a chemical isotropic etch. At the same time, ions with high energy strike the wafer surface knocking atoms out the the wafer lattice. These high energy ions are accelerated vertically toward the wafer, resulting in a highly anisotropic etch.

This process has been further developed to achieve nearly vertical sidewalls through a depth of hundreds of microns. Deep Reactive Ion Etching (DRIE) [41] refers to two methods. The Bosch process alternates the gases

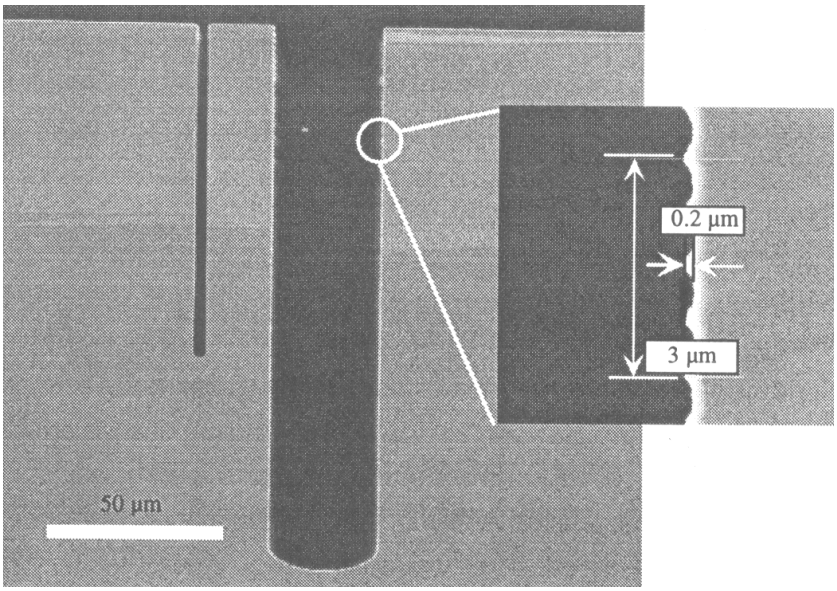

Figure 3.1: SEM micrograph of trenches fabricated using DRIE. (From [41])

introduced into the reaction chamber. One cycle deposits a passivating polymer, while the following cycle etches. Due to the highly directional ions, the passivating polymer remains on the vertical sidewalls but is quickly removed on the horizontal surfaces.

Another process called cryo-DRIE, is based on a similar principle [1]. In this process, the wafer is cooled to approximately $-110°C$. As a result, a passivating thin oxide ($SiFrO_2$) is grown on the vertical sidewalls.

The altering gas feed used in the Bosch process, can results in a scalloping effect on the sidewalls of the etched feature (Figure 3.1). The cryo process however, produces smooth sidewalls but at the expense of a much lower etch rate.

In order for the etch to be effective, the etched material must be transported away to make room for etch agents. As a result, narrow trenches etch slower compared to wide trenches. The effect is shown in figure 3.1.

3.2.2 Physical Vapor Deposition

Evaporation and sputtering are two physical vapor deposition processes used to deposit thin metal films [5]. In thermal evaporation the material to be deposited is heated until it evaporates. This is performed in a chamber where the wafers are placed in a hemispherical cage around the evaporating source. In order for the atoms of the vapor to reach the wafers, a high vacuum

($< 10^{-}3$ torr) is used. This results in relatively poor step coverage as the atoms are subjected to little spreading and are therefore very directional. Another form of evaporation uses an electron gun to evaporate the material to be deposited.

Sputtering is somewhat similar to RIE, using a plasma (noble gas e.g. Argon) to knock atoms out of a target. Here however, the target is the material to be deposited. The flux of released material is deposited on the wafers. The process is performed at a fairly rough vacuum, resulting in better step coverage due to more spreading of the deposits. As the target material does not melt, sputtering is better suited for the deposition of alloys and metals with high melting temperature.

In recent years, several laterally actuated switches fabricated in the device layer of a silicon-on-insulator (SOI) wafer, have been presented [11, 14, 16]. This SOI fabrication concept offers some interesting features i.e. fabrication of complex switch geometries using only a few process steps. Figure 1.2 shows an example of a switch and the concept of the SOI fabrication process.

3.3 Fabrication of switch concept

Several lateral RF MEMS switches have been demonstrated that have been fabricated using DRIE and a conformal metal deposition process [11, 14, 16]. To the author's knowledge, the processes used in these publications are not commercially available. There are however several commercially available silicon-on-insulator (SOI) fabrication processes that are based on the same principle [31, 42], but these are not directly applicable due to the conformal metal deposition process needed for RF MEMS switches.

3.3.1 SOI based process

The fabrication process presented in [11, 16] is based on an SOI wafer consisting of sandwich of a handle wafer, a buried oxide and a device layer. High resistivity Silicon (HR Si, $\rho > 4000\ \Omega cm$) is used for the handle wafer to reduce loss through the substrate. The buried oxide (SiO_2) functions as a sacrificial layer and isolation between the device layer and the handle wafer. Low resistivity Silicon (LR Si, $\rho < 0.1\ \Omega cm$) is used in the device layer.

The thickness of the device layer is determined by the mechanical and RF design but is also limited by the fabrications processes used and available SOI wafers. In [11, 16] the device layer is 35 μm thick, while the buried oxide is 2 μm. The required thickness of the buried oxide is discussed later in this section.

Figure 3.2 shows the principle of the fabrication process.

a) A masking layer is deposited/ grown and pattered, using lithography [5], defining the geometry of the switch and the transmission lines.

b) DRIE is used to etch through the device layer with the buried oxide functioning as an etch stop. The exposed buried oxide is then etched using a buffered oxide etchant. This effectively releases the thin structural elements as a result of a limited under etch.

c) A shadow mask is then temporarily bonded to the wafer using e.g. photoresist [11, 16]. An aluminum film is then deposited over the areas defined by the shadow mask. To achieve good microwave performance the metal must also be deposited on the vertical sidewalls of the structure.

d) The shadow mask is then removed and any residue is cleaned off.

In this process the aluminum is deposited using evaporation. It is stated that a thickness of $0.5-0.6\ \mu m$ and $1.2-1.5\ \mu m$ is deposited on respectively the sidewalls and the horizontal surface.

In order for sections to be electrically isolated, the thickness of the buried oxide must be thicker than the metal layer deposited in the bottom of the trenches. The capacitive coupling between different structures, is also effected by the amount of metal deposited in the bottom of the trenches (w_f in figure 3.2). An increased capacitive coupling effects the RF characteristics and is addressed in [11].

3.3.2 Silicon on glass based process

The process implemented in [14] is somewhat different compared to figure 3.2. In this case, the structure is fabricated on a normal Silicon wafer using DRIE. The patterned side of the wafer is then bonded to a glass wafer using anodic bonding [41]. The backside of the wafer is then thinned/ etched until the patterned structure becomes exposed. Similarly to the above process, the thin structures are then released using an isotropic wet etch. Here however, the glass substrate is etched instead of the buried oxide (Figure 3.3). Finally, a conformal thin metal film of Cr/Au is deposited using sputtering.

Using this process, a thickness of $0.45\ \mu m$ and $0.7\ \mu m$ is deposited on respectively the vertical sidewalls and the horizontal plane. This is achieved even though the silicon layer, bonded to the glass wafer, is $60\ \mu m$ thick. It is also stated that a metal thickness of $0.4\ \mu m$ is achieved on the sidewalls for a trench width $< 5\mu m$.

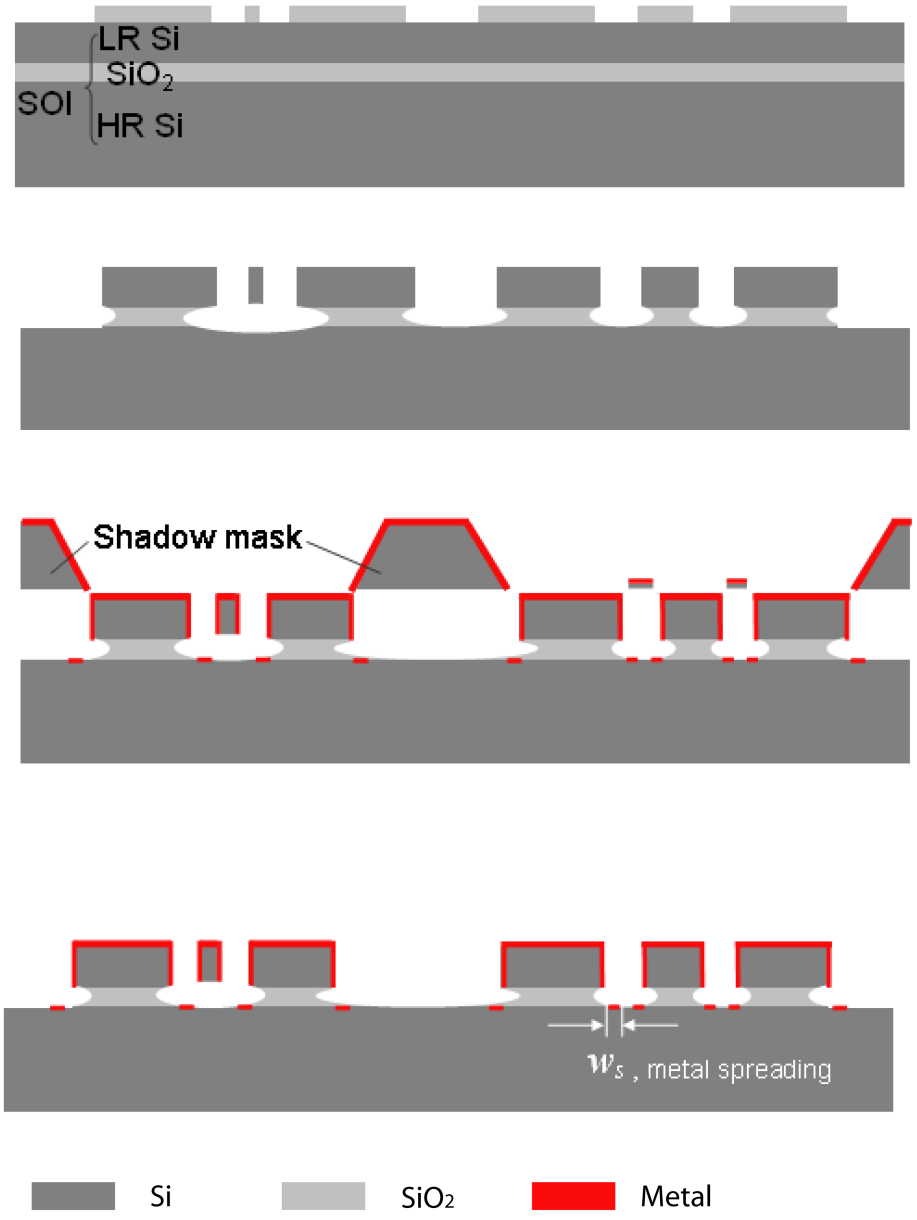

Figure 3.2: SOI fabrication process of a lateral series switch. (From [11])

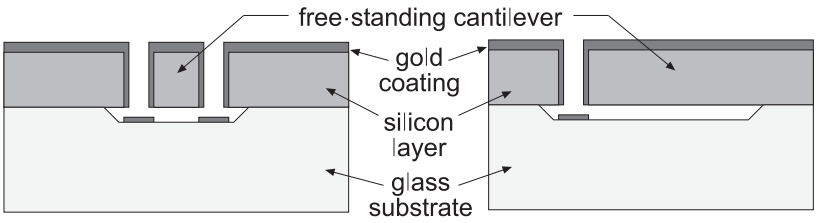

Figure 3.3: Lateral and longitudinal cross-section of structure fabricated using process DRIE and glass substrate. (From [14])

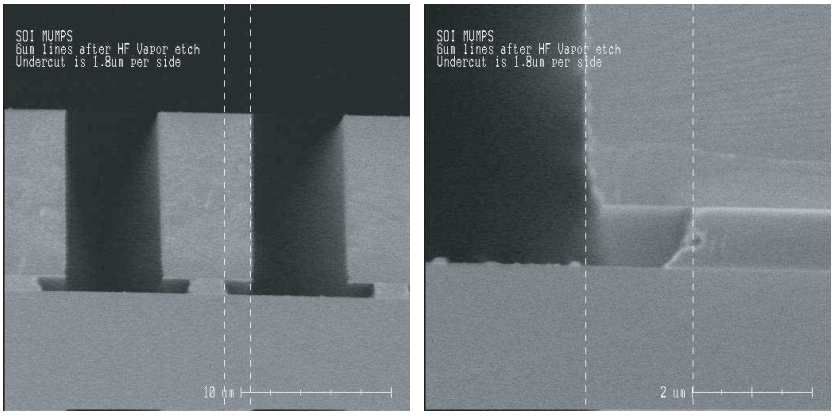

Figure 3.4: SEM image showing the undercut after HF vapor etching of the exposed oxide layer. (From [31])

3.3.3 Discussion

The fabrication processes presented in section 3.3.1 and 3.3.2, both use a wet etch to release the structures. As a result, the processes may require special release methods to avoid stiction problems (Section 3.4). The commercial SOI process offered by MEMScAP [31] however, uses a HF vapor etch process to etch the buried oxide isotropically (Figure 3.4). This is assumed to be a better alternative avoiding/ reducing stiction problems.

An important parameter for the switch design is the minimum feature size. The minimum feature size for the SOI process presented in section 3.3.1 is 2.5 um. In the design rules for the MEMScAP SOI processes, the minimum feature size is given as 2 um [31]. The accuracy and the minimum feature size of the DRIE etch is very dependent on the lithography process and mask used.

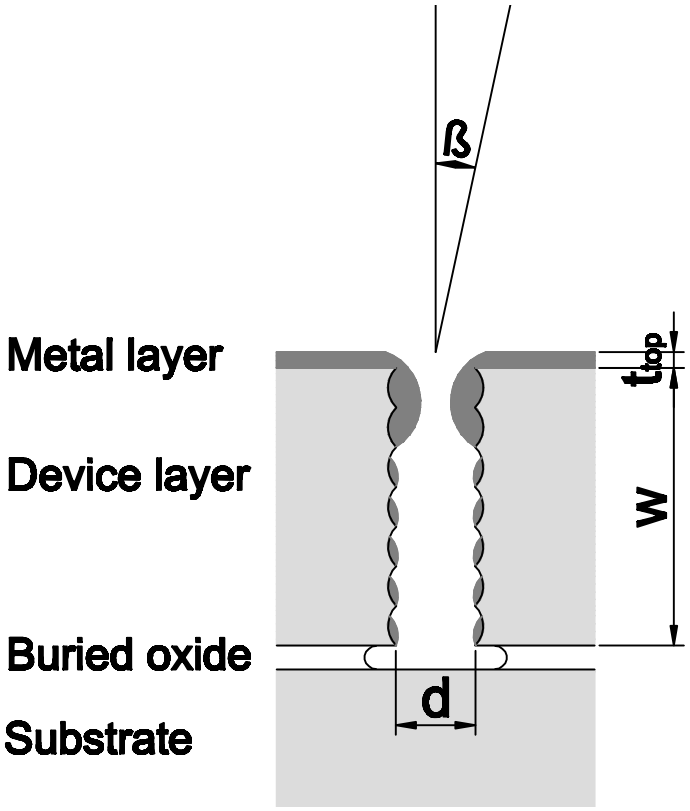

Figure 3.5: Deposition of conformal metal layer. (Dimensions not to scale)

The deposition of the conformal metal layer is complicated and depends on a number of parameters. An illustration of a trench with deposited metal is given in figure 3.5. The angle β indicates the angle of the incoming deposits. In order for the metal to be deposited evenly on the vertical walls, the angle β must vary and be sufficiently low. This can be achieved by continually varying the angle of the wafers relative to the source. As a result, the design of the shadow mask becomes important. The shadow mask shown in figure 3.2 is assumed to be fabricated using an anisotropic wet etch, which produces tapered sidewalls. This allows for variation of the angle β as opposed to the shadow mask shown in figure 3.6.

Several other important effects are also shown in figure 3.5. The scalloping, caused by the DRIE, may shadow for incoming metal atoms. If the surface diffusivity of the deposited atoms is low, this may result in a noncontinues metal film and a resulting increased beam resistance. Excessive deposition at the top of the trench must also be avoided as this narrows the trench.

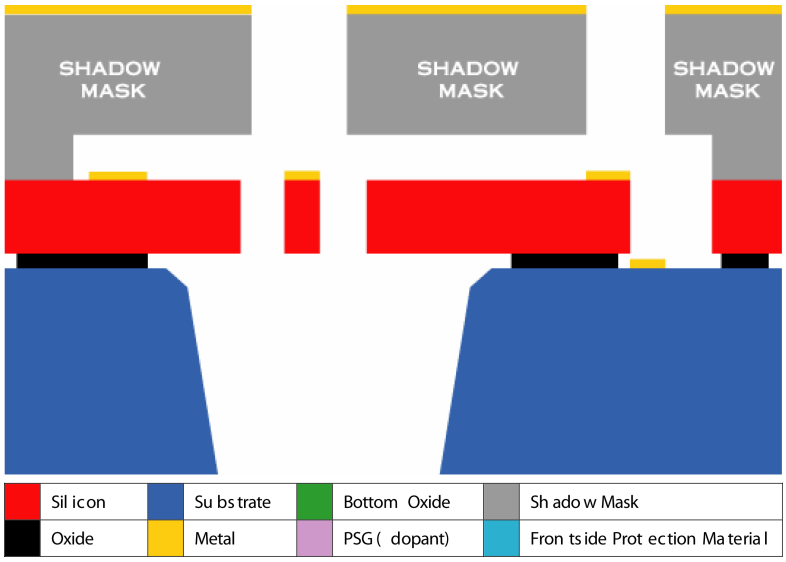

Figure 3.6: Shadow mask used in a commercial process. (From [31])

To obtain a stable electrical contact each time the switch is actuated, the contact areas should be geometrically defined. Figure 3.7 shows an example of such a defined contact. However, an accurate definition of such small tips can be difficult using DRIE. This is a result of the high energy ions of the DRIE plasma not being perfectly focused. Especially for wide trenches, this will typically cause a slight tapering of the sidewalls. For the small contact ridge shown in figure 3.7, this effect results in a skew contact.

For some applications it can be important that the fabrication process is compatible with CMOS processes (Section 2.3.1). The process shown in figure 3.3 requires anodic bonding of the glass substrate wafer, which is non-compatible with a post-CMOS process due to the elevated temperatures required. The other process steps are generally compatible with a post-CMOS approach.

3.4 Layered surface micromachining

The majority of the published RF MEMS switches are fabricated using deposited thin films for transmission lines, sacrificial layers and structural layers.

A somewhat simplified process flow for the fabrication of a switch, is given in figure 3.8.

a) A metal layer is deposited using i.e. sputtering. This layer is then

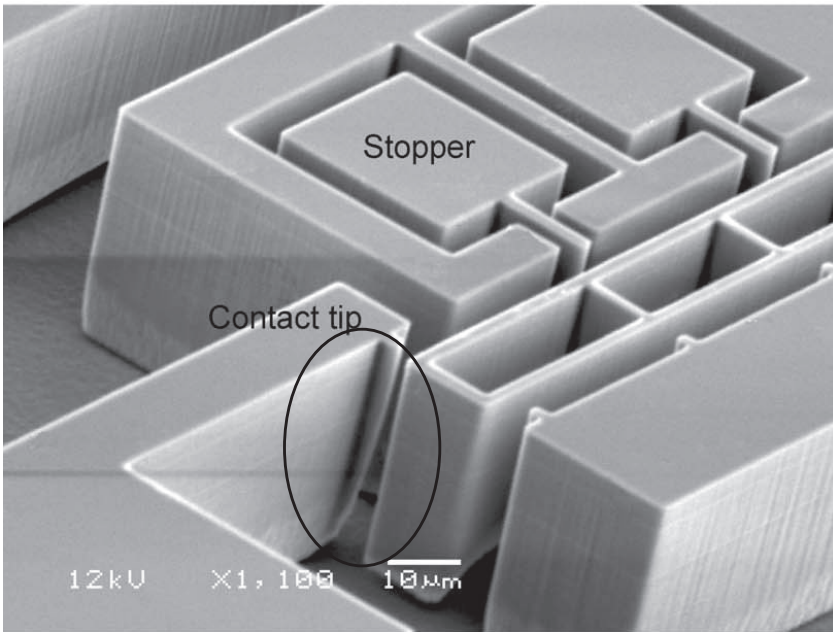

Figure 3.7: SEM micrograph of a defined contact. (From [16])

patterned, using lithography [5], to define the actuation electrode and transmission lines. A sacrificial layer (in this case Copper) is then deposited and patterned. In this example, a small notch is also defined that will become the upper contact.

b) The anchor of the beam is then defined by etching of the sacrificial layer.

c) A thin layer of the contact metal is then deposited and patterned before the structural layer forming the beam is deposited. The structural layer can be deposited using a physical deposition technique, electroplating (for thick layers) or a combination of the two.

d) The beam is then released using either a wet or dry etching technique [5].

The fabrication process for a capacitive shunt switch is very similar but includes the deposition and patterning of a dielectric layer, instead of a contact metal.

It is important that the structural layer has no or little residual stress to avoid warping of the released structure. The deposition of the structural layer must therefore be a well controlled process that may require post deposition annealing [5].

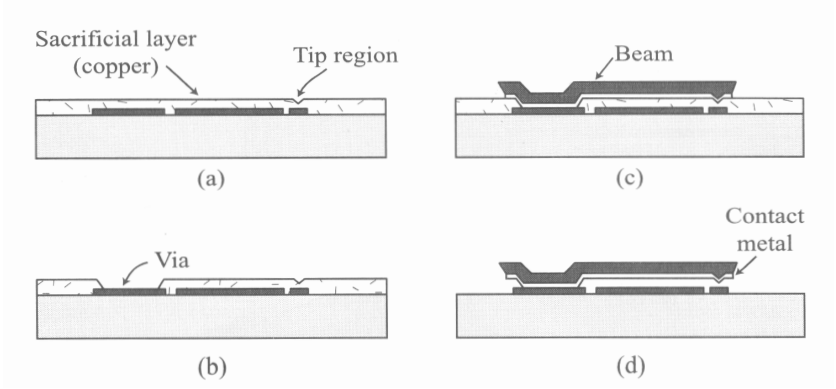

Figure 3.8: Surface micromachining of a serial metal contact switch. (From [37])

If a wet etching technique is used to etch the sacrificial layer, the surface tension of the liquid etchant can cause a problem called stiction [5, 41]. This is a result of the surface tension of the receding etchant pulling down the structure to be released, and the structure becoming stuck to the below layers. This can be avoided by using special release methods i.e. critical point drying [37, 41], or if the structure is very stiff.

Chapter 4

Contact modeling

4.1 Introduction

The main failure mechanisms for metal contact RF MEMS switches are related to the contact. The power level and switching condition, are important factors. Hot switching refers to the condition when the switch is loaded when switched, while cold switching refers to the condition where the signal is not present at the time of switching.

The drastic reduction of the reliability as a result of hot switching is not fully understood [37]. However, it is related to electric arcs that can form between the small contact spots when the upper and lower contacts separate. This results in large localized temperature increases, that can drastically change the contact topology and material properties.

Cold switching failure mechanisms are somewhat better understood. For low power levels ($1\ mW$) the predominant failure mechanisms are damage, hardening of the contacts or the formation of a dielectric on the contact [37]. As a result, the switch fails due to increased contact resistance or the creation of a series capacitor. For medium ($10-100\ mW$) to high ($>100\ mW$) power levels the failure mechanisms change. Due to the small contact spots created ($r \approx 100nm$), localized heating can cause material transfer, changes of the phase of the contact material [18] and microwelding [19, 37]. In this case the switch either fails due to increased contact resistance or due to the two contacts not releasing, remaining in the down position.

The contact resistance is also a very important parameter for the RF performance of the switch. It is therefore essential to understand the contact physics, to improve both reliability and RF characteristics of a switch.

MEMS contact physics is still a fairly immature field of research. In addition, much of the research is performed by companies with commercial

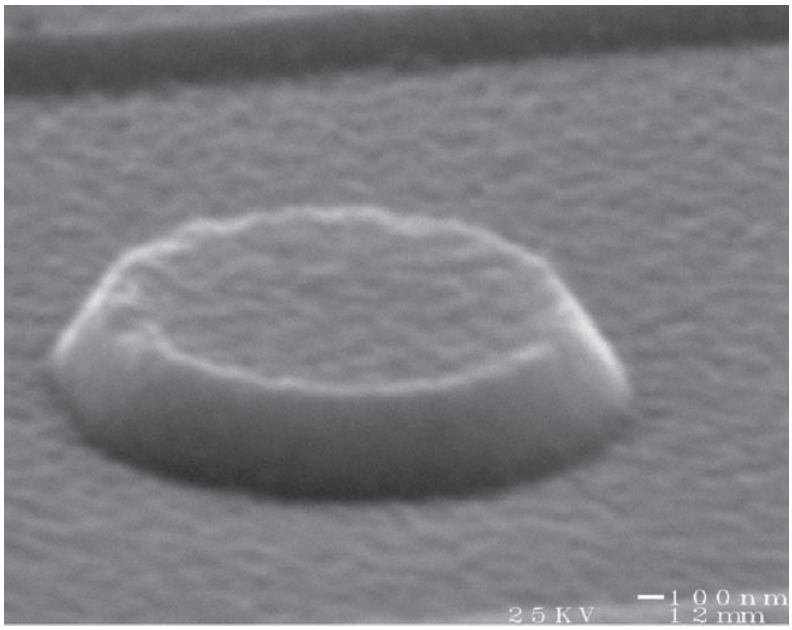

Figure 4.1: SEM micrograph of a MEMS switch contact. (From [19])

interests, resulting in limited publications.

In this chapter, the contact area and resistance modeling methods published in [18, 19] are presented and discussed.

4.2 Modeling approach

The methods presented in this chapter were implemented in MATLAB® functions and verified using the results presented in [18, 19].

Using these functions, the effect of variations of different parameters where investigated.

4.3 Material deformation

The surface of a deposited metal film is not completely smooth but consists of ridges and tops called asperities. Figure 4.1 shows a defined MEMS contact where these asperities can be seen. Due to the limited contact forces achieved for MEMS switches ($\sim 40-100\ \mu N$), this surface topology becomes important for the contact area and the resulting contact resistance.

The deformation of the contact surface is modeled using asperity-based models [15]. These models are based on the following assumptions:

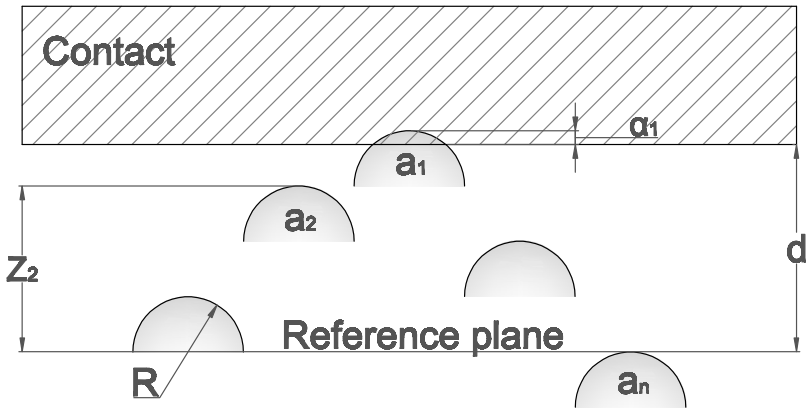

Figure 4.2: A rough surface contacting a smooth surface.

1. The rough contact surfaces are isotropic in the sense that all asperities have the same radius of curvature.
2. All surface asperity peaks are spherical near their summit.
3. Asperity heights are randomly distributed.
4. Asperities are far apart and independent, meaning that the deformation of one asperity does not affect the deformation of others.
5. No heating occurs, that could change the material properties.

Figure 4.2 shows a schematic of a rough surface contacting a smooth surface and the parameters used in the following models. The simplification, where only one surface is rough, has been shown to be equivalent to two rough surfaces in contact [6].

The metal films used as contact materials (i.e. Au alloys) are elastic-plastic materials. When a material loaded the material will deform. If the resulting strain is below a certain limit (elastic limit), the material will return to its original shape when unloaded. However, if the load is increased so that the strain increases above the elastic limit, the deformation becomes plastic and the material hardens. Plastic deformation results in permanent deformation of the material [24].

4.3.1 Elastic model

In the elastic region, the contact area and contact force for a single asperity is given as [6]

Parameter	Symbol	Value
Asperity radius of curvature	R	100 μm
Young's modulus, upper contact	E_1	85 GPa
Poisson ration, upper contact	ν_1	0.44
Young's modulus, lower contact	E_2	85 GPa
Poisson ration, lower contact	ν_2	0.44
Meyer hardness	H	1 GPa
Surface roughness	σ	30 nm
Number of asperities	n	5
Electron mean free path	l_e	500 Å
Resistivity	ρ	3.6 $\mu\Omega cm$

Table 4.1: The properties of the Au contact used in this chapter. Values from [12, 19]

$$A = \pi R\alpha \tag{4.1}$$

$$F_c = \frac{4}{3}E'\alpha\sqrt{R\alpha} \tag{4.2}$$

where R is the radius of curvature of the asperity and α is the vertical deformation of the individual asperity (Figure 4.2). The so-called Hertzian elastic modulus is given as

$$\frac{1}{E'} = \frac{1-\nu_1^2}{E_1} + \frac{1+\nu_2^2}{E_2} \tag{4.3}$$

where ν_n and E_n are respectively the Poisson ratio and Elastic modulus for the two contacting surfaces. For circular areas the contact area radius becomes

$$r = \sqrt{\frac{2F_cR}{4E'}} \tag{4.4}$$

4.3.2 Plastic model

A model used for fully plastic deformation is given in [6]

$$A = 2\pi R\alpha \tag{4.5}$$

$$F_c = HA \tag{4.6}$$

where H is the Meyer hardness of the material.

4.3.3 Elastic-Plastic

When combining the elastic and plastic model, a discontinuity occurs at the onset of plastic deformation (Figure 4.3). Methods have therefore been developed to cover both the elastic and plastic range [6, 23].

The asperity vertical deformation when the transition from elastic to plastic deformation occurs is given by

$$\alpha_c = \left(\frac{\pi KY}{2E'}\right)^2 R \tag{4.7}$$

where K is the yield coefficient and can be approximated as

$$K = 1.2828 + 1.158\nu \tag{4.8}$$

The parameter, Y, is the yield strength and is related to the hardness, H

$$Y = 0.354H \tag{4.9}$$

The contact area and contact force are calculated using the following formulas

$$A = \pi R\alpha \left(2 - \frac{\alpha_c}{\alpha}\right) \tag{4.10}$$

$$F_c = \left[3 + \left(\frac{2}{3}K - 3\right)\frac{\alpha_c}{\alpha}\right] YA \tag{4.11}$$

Assuming the contact is circular, the contact radius can be calculated using $r = \sqrt{A/\pi}$. Figure 4.3 shows the calculated contact radius as a function of contact force.

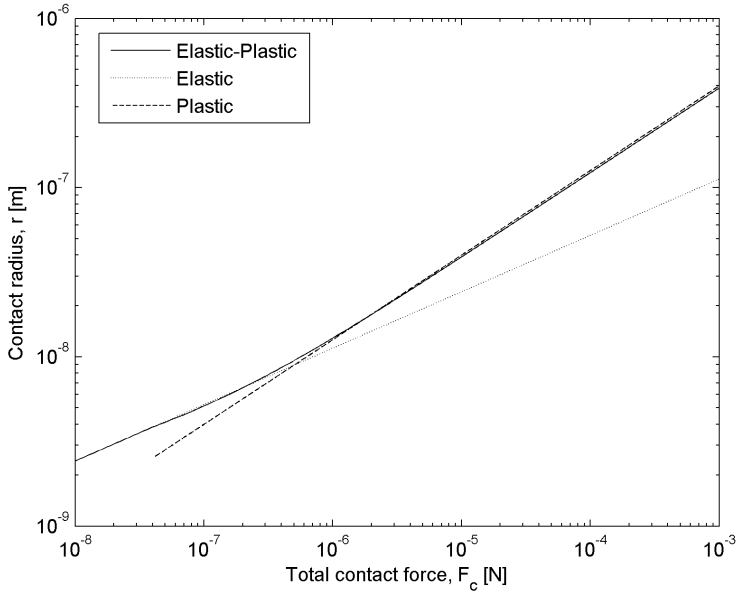

Figure 4.3: Contact radius of a single Au asperity.

4.3.4 Multiple asperities

The distribution of the asperities heights, Z_n (Figure 4.2), is given by the surface roughness and is specified as a standard deviation or root-mean-square value. The deflection of the individual asperities becomes

$$\alpha_n = d - Z_n \qquad \text{for } d \geq Z_n \tag{4.12}$$

where d is the distance between the smooth contact surface and the reference plane (Figure 4.2). By incrementing d, the contact radius of the individual asperities and the total accumulated contact force can be calculated. Figure 4.4 shows the contact radius of individual asperities as a function of the total accumulated contact force. For the given contact, the contact force must exceed ~ 300 μN for all five asperities to come into contact.

4.4 Contact resistance

When calculating the contact resistance, the effects of constriction and contaminant film must be taken into account [25]. The overall contact resistance becomes

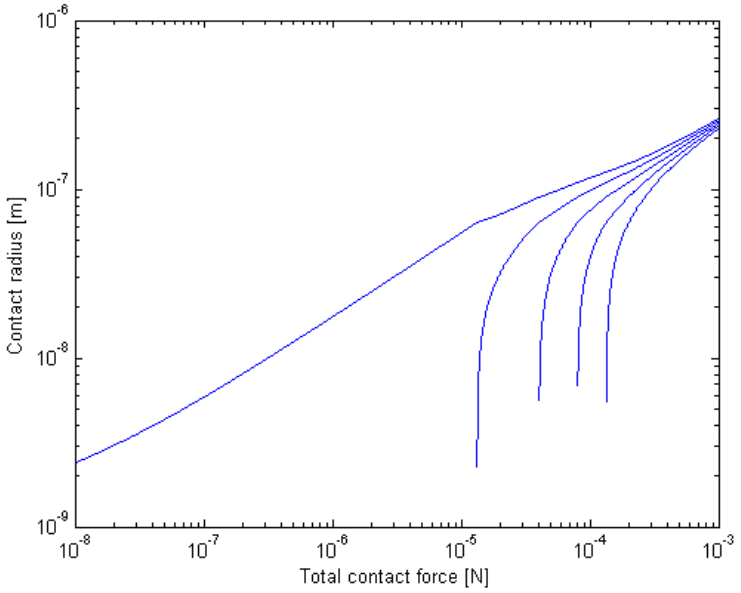

Figure 4.4: Modeled contact radius of the individual asperities for the contact specified in table 4.1.

$$R_{Contact} = R_c + R_{cf} \tag{4.13}$$

where R_c is the resistance due to constriction and R_{cf} is the added resistance due to the presence of a contaminant film.

The models presented here aim to estimate only the constriction resistance, R_c. The presence of a contaminant film is very process dependent and may change drastically during the first cycles. Results presented in [19], show that after $\sim$ 300 cycles in an inert ambient the measured contact resistance converges toward the calculated contact resistance.

For conventional macro-relays, the contact resistance is calculated solely based on Maxwell spreading resistance theory [25]

$$R_M = \frac{\rho}{2r} \tag{4.14}$$

where ρ is the Resistivity and r is the radius of the contact.

For MEMS switches the contact area can be comparable to the electrons mean free path, l_e. For such contacts there will be a large potential gradient near the contact causing electrons to be accelerated, passing through the contact ballistically [2]. This effect increases with an increasing Knudsen number

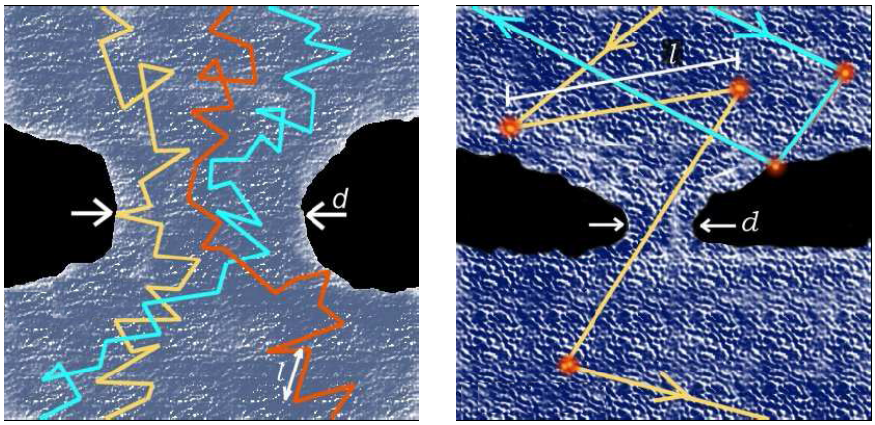

(a) **(b)**

Figure 4.5: Illustration of the Maxwell spreading resistance (a) and Sharvin resistance (b).

$$K_n = \frac{l_e}{r} \tag{4.15}$$

where l_e is the mean free path. For small contact areas (high Knudsen number) the contact resistance is calculated using the Sharvin resistance [44]

$$R_S = \frac{4\rho K_n}{3\pi r} \tag{4.16}$$

Figure 4.5 is an illustration of the electron motions for the two domains where the Maxwell spreading resistance and Sharvin resistance are valid.

A size dependent constriction resistance, which interpolates between the Maxwell spreading resistance [Eq. (4.14)] and the Sharvin resistance [Eq. (4.16)], is given by the Wexler resistance [44]

$$R_W = R_S + \Gamma(K_n) R_M \tag{4.17}$$

where $\Gamma(K_n)$ is a slowly varying gamma functions which determines the relative contribution of the R_M and R_S. The two gamma functions implemented in literature are somewhat different (Figure 4.6). The function derived in [44] varies between $\Gamma(0) = 1$ and $\Gamma(\infty) = 0.694$. This implies, that even for small contacts (large Knudsen number) there will be a contribution from the Maxwell spreading resistance on the overall contact resistance. In [10]

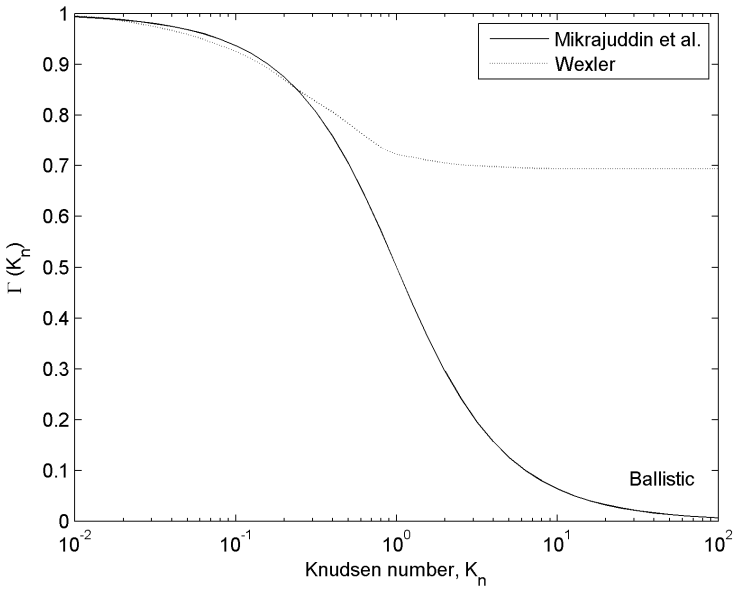

Figure 4.6: The two $\Gamma(K_n)$ functions used in litterature.

however, it was propose that the Maxwell spreading resistance and Sharvin resistance should be the asymptotic limits, for respectively large and small contacts relative to the electron's mean free path. The function proposed by [10] is given as

$$\Gamma(K_n) \approx \frac{2}{\pi} \int_0^\infty e^{K_n x} sinc(x) dx \tag{4.18}$$

Both gamma functions are shown in figure 4.6.

Figure 4.7 shows the calculated contact resistance for a single asperity as a function of the contact force. The figure also shows the variation of the two resistance components.

For MEMS switches, the limited contact force results in multiple deformed asperities that form contacts spots with varying area (Figure 4.4). Due to the low surface roughness and tightly packed grain structures of sputtered surface films, it is however uncertain if the individual asperity contacts can be regarded as independent contacts [18].

The so-called multiple asperity model, assumes that the individual asperity contact spots are independent and conduct in parallel (Figure 4.8). For this model, each individual contact is calculated according to the above method and the total contact resistance becomes

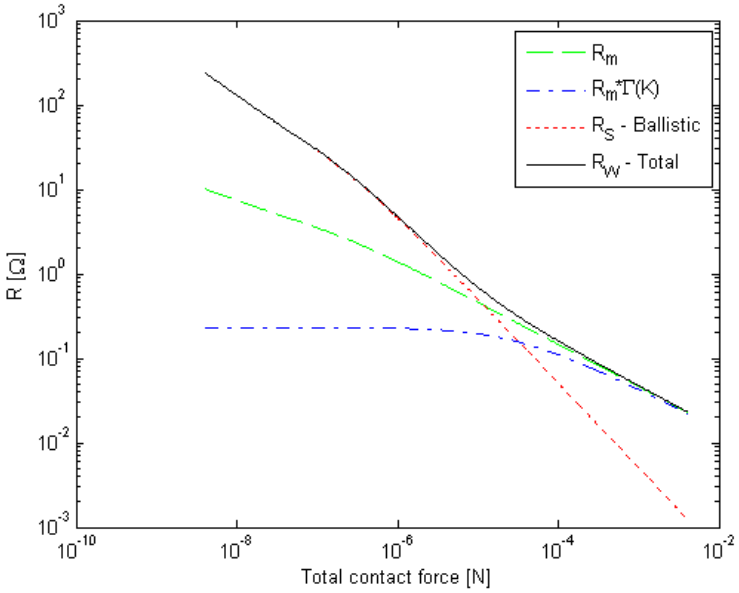

Figure 4.7: The calculated contact resistance for a single asperity.

$$\frac{1}{R_C} = \sum_i \frac{1}{R_{Wi}} \tag{4.19}$$

The single effective asperity model however, assumes that the individual asperity contact spots are not independent. It may i.e. be argued that the boundary conditions related to the Sharvin resistance are no longer valid for tightly spaced contacts. For this model, an effective contact area is defined as the sum of all the individual contact areas (Figure 4.8). Assuming this effective area is circular an effective radius is given as

$$r_{eff} = \sqrt{\frac{\sum_i A_i}{\pi}} \tag{4.20}$$

This effective radius is then used to calculate the contact resistance. Implementing this model the contribution from the Sharvin resistance (ballistic electron transport) will only be at initial contact and will therefore be negligible.

Instead of relying solely on one model, an upper and lower estimate for the contact resistance can be calculated using respectively the multiple and single effective asperity models [19].

Figure 4.9 and 4.10 show the modeled contact resistance for the contact

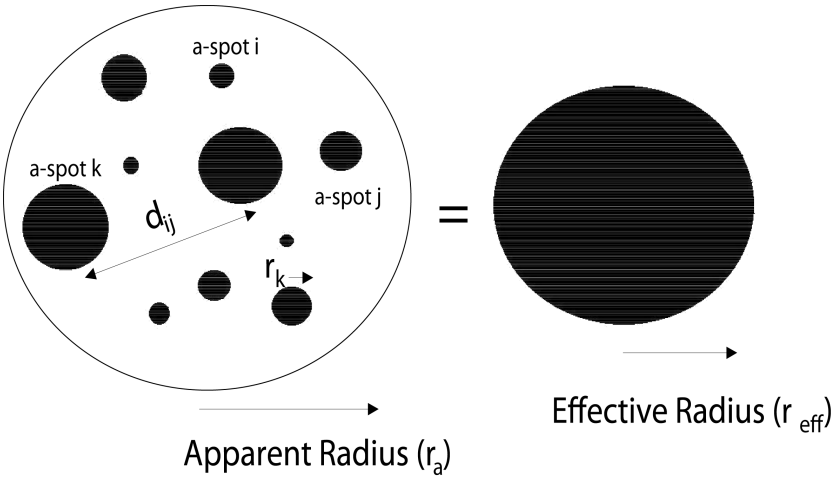

Figure 4.8: Illustration of the multi asperity (left) and the single effective asperity (right) contact area models. (From [18])

specified in table 4.1. As indicated by figure 4.9 and 4.4, only a single asperity is in contact until the contact force is $\sim$ 15 μN. At this point, the asperity model used comes into effect.

4.5 Parameter sensitivity

The contact resistance model presented here is dependent on a number of parameters. The implications of variations in these parameters are therefore important to understand.

The Young's modulus, E, of thin metal or metal alloy films may vary from the bulk property, are very process dependent and can be quite difficult to measure accurately [12]. There may therefore be a large degree of uncertainty linked to a given value. Typical values for E, for applicable metal and metal alloy films, vary between 85 to 170 GPa [12]. Such an increase, results in a somewhat smaller contact area during elastic deformation of the asperities [Eq. (4.4)]. However, in the μN contact force range, which is interesting for MEMS, the deformation is plastic and the variations are minimal [Eq. (4.5)].

In [19], the asperity radius of curvature, R, is estimated to be 50-200 nm. However, this value is assumed to vary depending on the deposition process, release process and the metal/ metal alloy film implemented. At first contact, an increased value for R results in reduced contact resistance. This is a result of the increased contact area for a given deflection, α [Eq. (4.1)]. However, this also results in an increased contact force. As a result, in the μN region

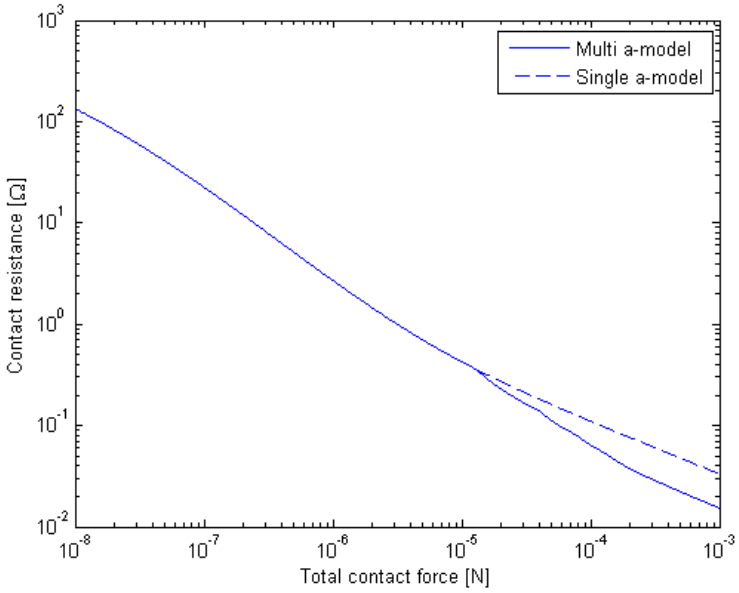

Figure 4.9: Modeled contact resistance for the Au specified in table 4.1.

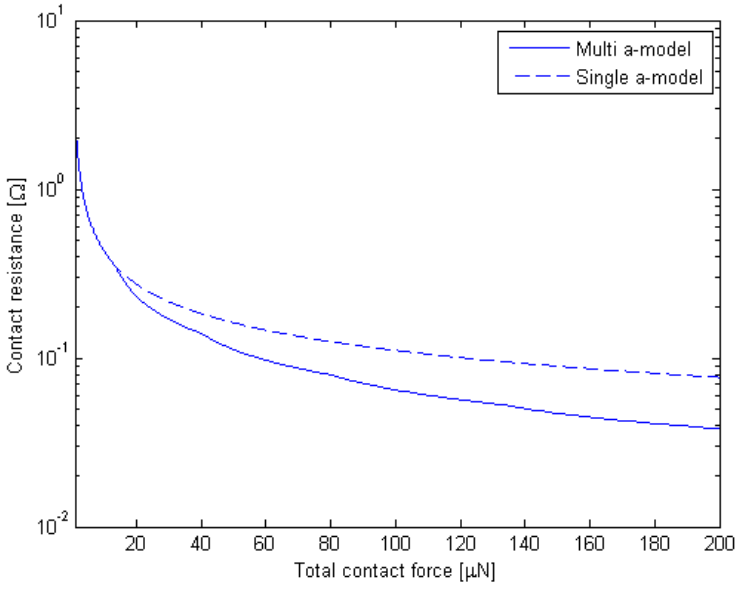

Figure 4.10: Modeled contact resistance for MEMS switch contact force range.

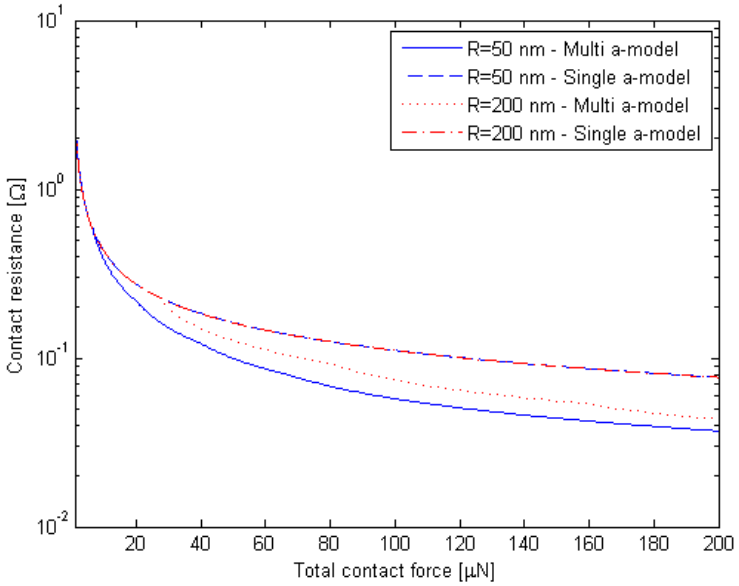

Figure 4.11: Calculated contact force for two values of R.

the number of asperities in contact is reduced for a given contact force. Using the multi asperity model, the contact resistance therefore increases with R (Figure 4.11). The influence on the single effective asperity model is however minimal.

Based on eq. (4.6) the asperity contact radius can be written as

$$r = \sqrt{\frac{F_c}{\pi H}} \tag{4.21}$$

The contact radius of the individual contact spots is therefore reduced for hard contact metals. This in turn, results in an increased contact resistance as $R_c \propto \frac{1}{r}$ [Eq. (4.14)].

$$R_c \propto H^{\frac{1}{2}} \tag{4.22}$$

The Meyer hardness, H, which varies between 1 and 15 GPa for applicable contact metals [12, 38], therefore becomes a very important parameter for the contact resistance. Based on figure 4.12, it can be seen that an increased hardness also requires an increased contact force in order to achieve a stable contact resistance.

The contact resistance is a linear function of the resistivity [Eq. (4.14),

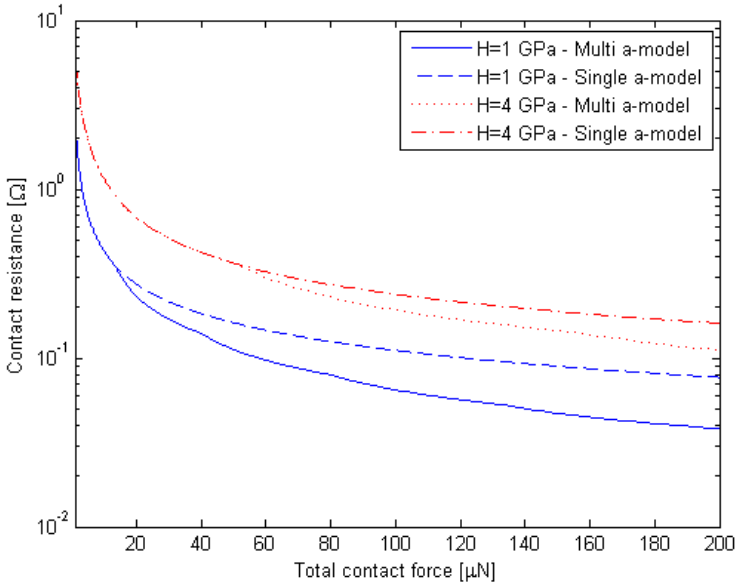

Figure 4.12: Calculated contact force for two values of H.

(4.16)], which varies between $\rho = 3 - 15\ \Omega cm$ for contact metals that are implemented in MEMS switches [12, 38]. Given the typical variations for the individual parameters, the Meyer hardness, H, and the resistivity, ρ, are the most important material properties for the contact resistance.

The surface roughness and the number of asperities coming into contact are other factors that need to be considered. In literature, it has been proposed that only $\sim 5 - 10$ asperities make contact for the achievable contact forces using a electrostatic actuated MEMS switch [19, 37]. Using the method presented in section 4.3, the number of asperities in contact for a contact force of $F_c = 100\ \mu N$ has been estimated. The results for several different surface profiles are presented in table 4.2 and agrees with the proposed number.

The calculated contact resistance for Profile 2 and 4 (Table 4.2)is given in figure 4.13. The increased number of asperities (Profile 4), results in a somewhat lower contact resistance based on the multiple asperity model. This limited difference in resistance confirms that Profile 2, which is used in this section, is a good approximation.

The contact resistance calculated using the single effective asperity model remains the same for all the profiles. This is a result of the contact area being a linear function of the contact force [Eq. (4.6)] and the single effective asperity [Eq (4.20)] model implemented to calculate the resistance.

Profile	Surface roughness, $\sigma[nm]$	Num. of asperities	Asperities in contact
1	-	1	1
2	30	5	3
3	30	20	7
4	10	20	11
5	30	50	8
6	10	50	12

Table 4.2: The number of asperities in contact at a contact force, $F_c = 100\ \mu N$.

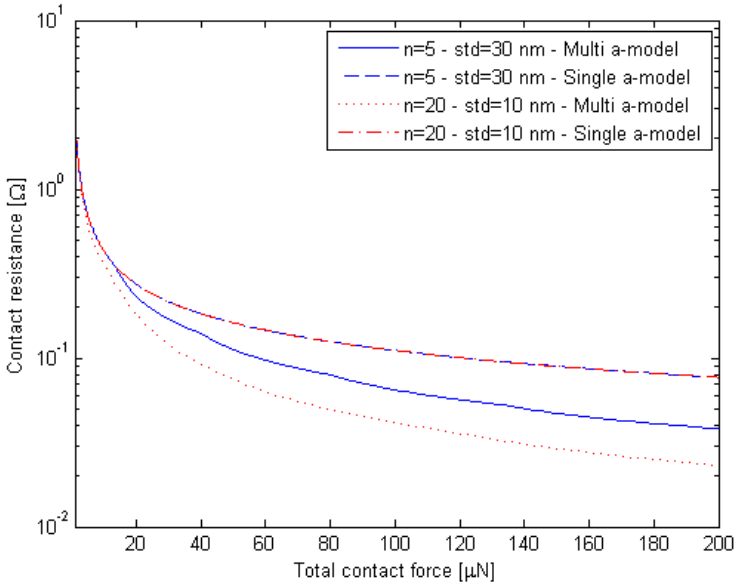

Figure 4.13: Calculated contact force for two different surface topologies.

Contact metal	First cycle Ω	After burn-in Ω	Reference
Au	10-0.07	0.07-0.03	[19]
Au	0.94	0.83	[18]
Au-(2%)Pd	0.63	0.49	[18]
Au on Au-(6%)Pt	0.73	0.67	[18]
Au-(5%)Pt-(0.5%)Cu	0.34	0.33	[18]
Au	0.1-0.05	-	[26]

Table 4.3: Summary of values for contact resistance for different contact metals. Contact force is $F_c \approx 100\mu N$.

4.6 Discussion

For a contact force $F_c \approx 100\ \mu N$ the contact resistance is estimated to be $R_c \approx 0.1\Omega$, using the contact properties given in table 4.1. This correlates well with some values presented in literature (Table 4.3). The differences in the presented values, is assumed to be partially due to different characterization methods used. In [19], for example, it is clearly stated that the characterization is performed in an inert ambient to prevent a contaminant film from forming on the contact. On the other hand, the relatively high contact resistance values given in [18] are partially credited to the forming of a contaminant film.

The methods presented here, do not say anything about the reliability of the switch. However, the methods explain some of the contact physics that in turn could be used to better understand the factors that determine the reliability.

Methods to estimate the adhesive force that occur between contacts have been presented but are not thoroughly documented [20]. The adhesive force generated is a complex function of the contact materials used, contact force and the temperature (function of current). As a rough estimate the adhesive force is 40% of the contact force [25].

Chapter 5

Modeling of beam mechanics

5.1 Introduction

A large number of the published RF MEMS switches are series metal contact switches, which implement a cantilever beam as the switching element [37]. For an electrostatic actuated switch, a variable cross-section can be used to e.g. reduce the actuation voltage, increase the contact force etc. An example of a commercially available switch that incorporates a variable cross-section is given in figure 5.1.

In this chapter analytical models are derived to analyze a layered cantilever beam with two cross-sections.

5.2 Modeling approach

The majority of the modeling was done using the analytical methods presented in this chapter. However, so-called system level simulation and FEM (Finite Element Modeling) are also used, both to verify the analytical methods and to perform more detailed analysis.

5.2.1 Analytical method

The analytical methods were implemented in MATLAB® functions, where a number of parameters could be varied at once. Using this approach, the effect of varying a given parameter could be better understood allowing for better optimization of a structure. Once the functions were developed the analysis time is in the order of seconds.

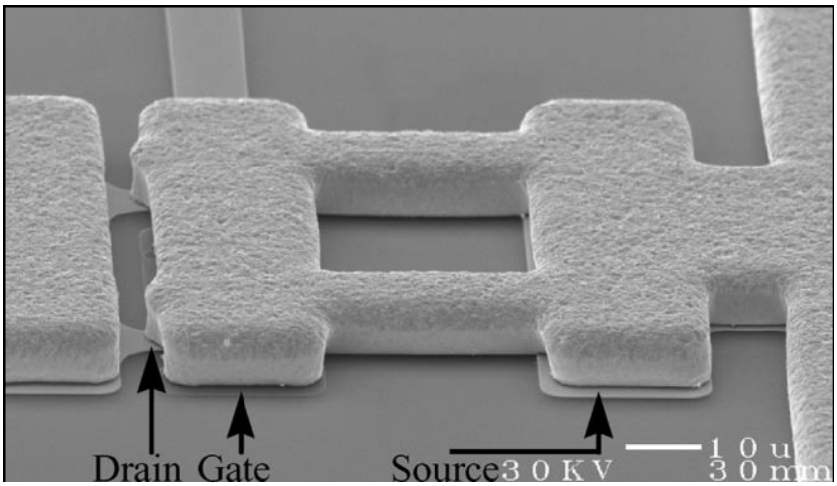

Figure 5.1: SEM micrograph of a microswitch showing the principle of variable cross section. The fixed end of the double cantilever beam is on the right.[19]

Parameter	Symbol	Value
Total length	l_{tot}	400 μm
Length section AB	l_1	200 μm
Length section BD	l_2	200 μm
Tip length	l_3	10 μm
Width	w	35 μm
Height section AB	h_1	2.5 μm
Height section BD	h_2	5 μm
Thickness of cladding layer	t_m	0.6 μm
Initial gap	g_0	4 μm
Contact gap	d	3 μm
Young's modulus beam core	E_{Si}	169 GPa
Density of beam core	ρ_{Si}	2500 kg/m^3
Young's modulus cladding layer	E_{Au}	58 GPa
Density of cladding layer	ρ_{Au}	19300 kg/m^3

Table 5.1: The characteristics of the cantilever beam used in this chapter. Any variations from this is commented in the respective calculations.

5.2.2 System level simulations

The CoventorWare® Architect module was used for system level simulations. In Architect, predefined objects are combined to form complex systems. In this case a cantilever beam with an actuation electrode and contacts (Figure 5.3). The predefined objects are based on analytical methods, similar to the once presented in this chapter. Compared to FEM, the simulation time can be in the order of seconds compared to minutes/hours for the FEM simulations. The interaction between different domains e.g. mechanical, electrical etc., can also be effectively simulated, using a wide range of analysis e.g. variation of a parameter, transient etc.

Figure 5.2 shows how the different modules of CoventorWare® are related. All modules are based on a process file where the different deposition and etch steps to fabricate the structure are defined. The predefined objects, used in Architect, are based on this layered process file. For example, the object for an electrostaticly actuated beam is assigned a layer for the beam and a layer for the lower electrode. This concept however does not work for laterally actuated structures where both the beam and electrode are fabricated in the same layer. In order to use Architect in this thesis, an equivalent process file was specified, effectively modifying the laterally actuated beam into a vertically actuated beam. This is acceptable for simple structures but for more complex structures this is not possible. Architect is therefore severely limited for analysis of laterally moving structures.

Figure 5.3 shows the system model schematic. Each object is assigned a number of parameters defining position, length, width, thickness, damping etc. As mentioned above, the parameter specifying the layer thicknesses are given by the process file. However, this specific parameter may be overridden to allow for simulations with e.g. different metal layer thicknesses. Some of the object also return values that can be used as input for other objects or as output e.g. contact force, capacitance.

The accuracy of system level simulations is often good but some mechanisms/ effects might not be captured by the analytical methods used. This is important to be aware of.

5.2.3 Finite Element Modeling

Analysis performed using finite element modeling (FEM) methods are much less constrained compared to system level simulations. However, performing a transient analysis of a MEMS switch, which may include both damping and contact, becomes very complex requiring large amounts of computer resources and are time consuming.

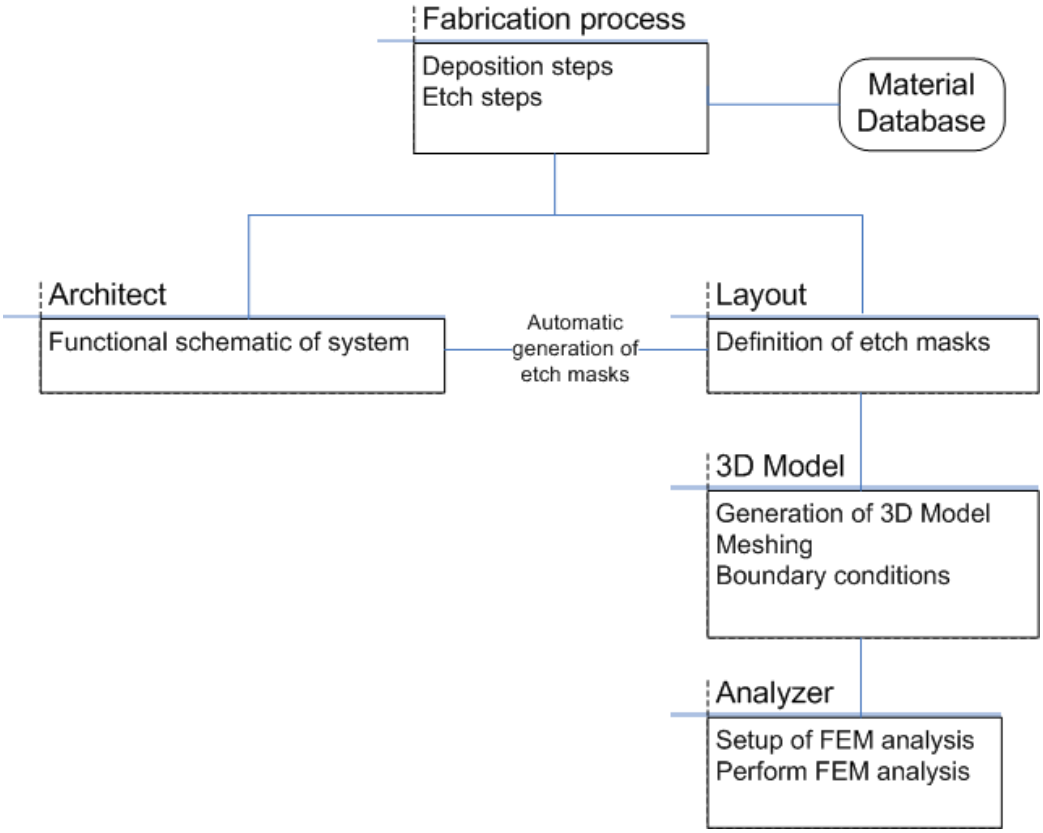

Figure 5.2: Illustration of the different modulus of CoventorWare

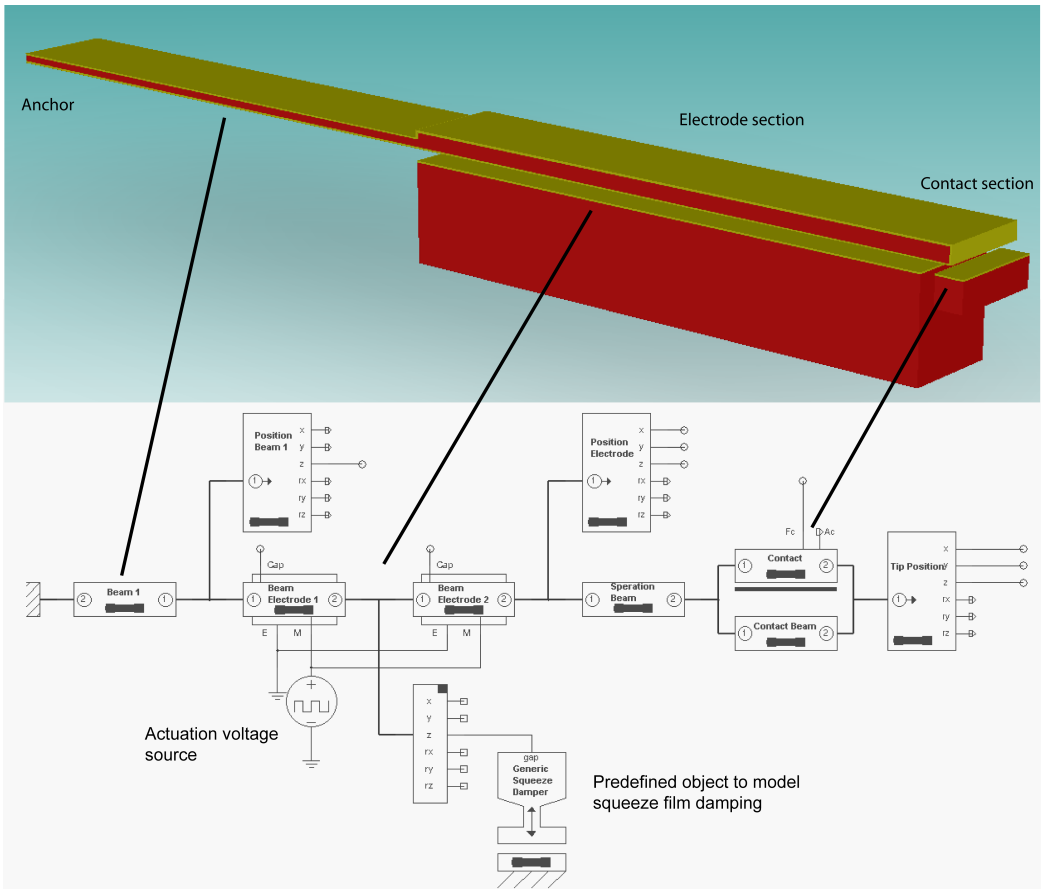

Figure 5.3: System model schematic.

Number	Step Name	Action	Layer Name	Material Name	Thickness	Mask Name	Photoresist	Etch Depth
0	Substrate	Substrate	Substrate	SILICON	50	SubstrateMask		
1	Grow oxide	Stack Material	BOx	OXIDE	3			
2	Bonding of device layer	Stack Material	Device layer	SILICON	35			
3	DRIE etch	Straight Cut				DRIE_etch	+	
4	Sputtering	Conformal Shell	Metal_deposition	GOLD	0.6			
5	Shadow mask	Straight Cut				Shadow_mask	+	
6	Alternative	Straight Cut				Shadow_mask	-	0.6

Figure 5.4: Process file used for FEM analysis.

Due to how a FEM model is defined, the simple adjustment of i.e. a geometric parameter, such as the thickness of a beam section, is much less flexible compared to system level simulations. The CoventorWare® ANALYZER module (Figure 5.2) offers some tools to adjust parameters, but often a new FEM model must be generated. This may involve the definition of a new process file, modification of etch masks and re-meshing of the model.

The CoSolve solver is used to analyze the response of the electrostatic actuated cantilever. This solver uses the MemMech solver to analyze the mechanics and MemElectro to determine the electrostatic loading.

To define the laterally actuated switch, the fabrication process defined in the process file is modified somewhat compared to the process given in section 3.3. The process steps used are given in figure 5.4. Instead of a shadow mask, an additional etch step (step #5) is used to remove metal deposited in the bottom of the trenches.

When meshing, the thin conformal metal layer results in a threefold increase in the number of elements. The effect is shown in figure 5.5. In addition, as a rule of thumb the elements should be square in the plane perpendicular to the plane of bending. This means that the elements size should be approximately the thickness of the thin metal layer. To reduce the number of elements (and computation time) a cross-section consisting of only one material and an effective Young's modules can be implemented. This is described in section 5.3.3.

To determine the required element size and type, a mesh convergence analysis can be performed. A number of analyses are then performed where the mesh is refined until the result converges. In the case of the MEMS switch, three such analysis can be performed. The mesh required to accurately model mechanical behavior of the switch may be different than what is needed to accurately model the electrostatic actuation (Figure 5.5). Refining the mesh at the contact tip may also be required.

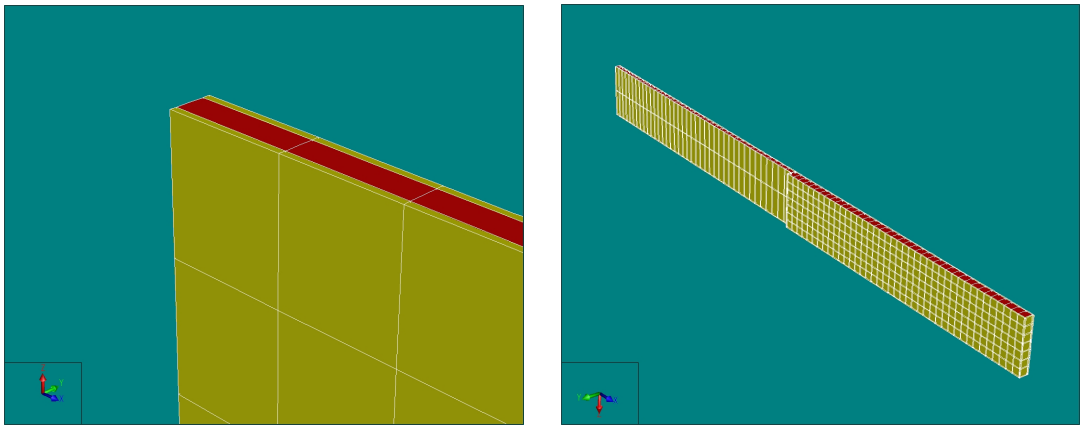

(a) (b)

Figure 5.5: The additional elements introduced by the thin metal film (a). Different mesh densities for beam and electrode (b)

5.3 Modeling methods

5.3.1 Electrostatic Actuation

Figure 5.6 shows a schematic of a cantilever beam with two cross-sections. For several reasons, which will explained later, section BD is made stiffer than AB and is therefore assumed not to curve during bending. The electrostatic force F_e becomes [11]

$$F_e = \int_{l_1}^{l_1+l_2} \frac{\varepsilon_0 w_a V_a^2}{2(g_0 - \delta_x)^2} dx \tag{5.1}$$

where ε_0 is the permittivity of free space, w_a is the width of the electrode area, V_a the actuation voltage and g_0 the initial gap. The parameter δ_x is given as

$$\delta_x = \delta_B + \theta_B(x - l_1) \tag{5.2}$$

where δ_B is the deflection at point B, θ_B is the beam angel at point B and x the location along the beam.

In order to simplify eq. (5.1), δ_x is typically substituted with δ_C located at $b = l_2/2$ [11, 37]. Eq. (5.1) becomes

$$F_e = \frac{\varepsilon_0 w_a l_2 V_a^2}{2(g_0 - \delta_C)^2} \tag{5.3}$$

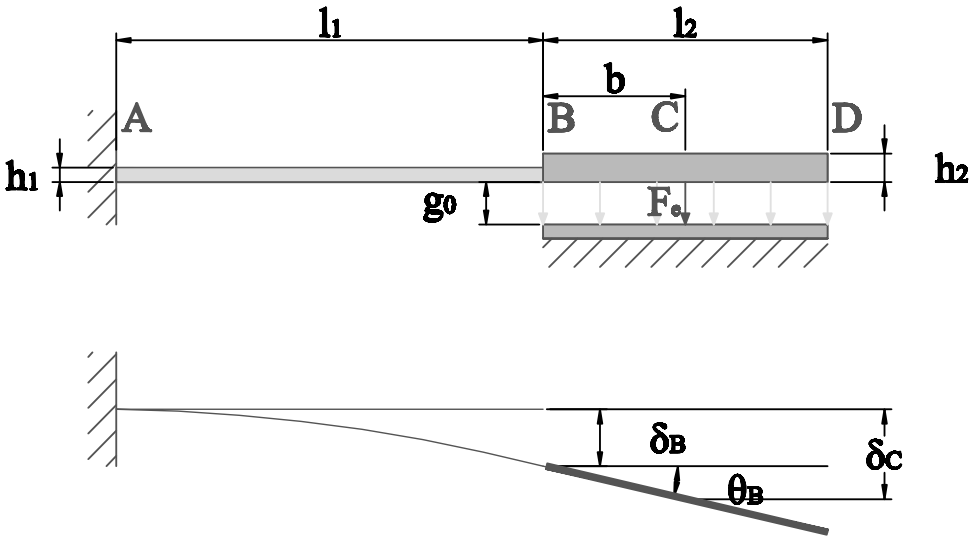

Figure 5.6: Electrostatic actuated cantilever beam with two cross-sections.

which is the equation for electrostatic force between two parallel plates. If however θ_B becomes significant, the electrostatic force, F_e, will shift closer to the tip.

Figure 5.7 shows a schematic of an electrostatic actuator. The force supporting the upper electrode can be expressed using Hooke's law [24]

$$F_k = kx \tag{5.4}$$

where k is the equivalent spring constant and x is the elongation of the spring. Based on this, the net force on the upper plate becomes

$$F_{net} = -F_e + F_k = -\frac{\varepsilon A_a V_a^2}{2g^2} + k(g_0 - g) \tag{5.5}$$

where g_0 is the initial gap between the two plates and g is the gap at a given deflection, x. When the system is stable, F_{net} is zero. However, at a certain point the system becomes unstable and the upper plate snaps down. The behavior is called pull-in and it can be explained by studying how the partial derivative of F_{net} with respect to g varies given a small perturbation and constant actuation voltage, V_a [41].

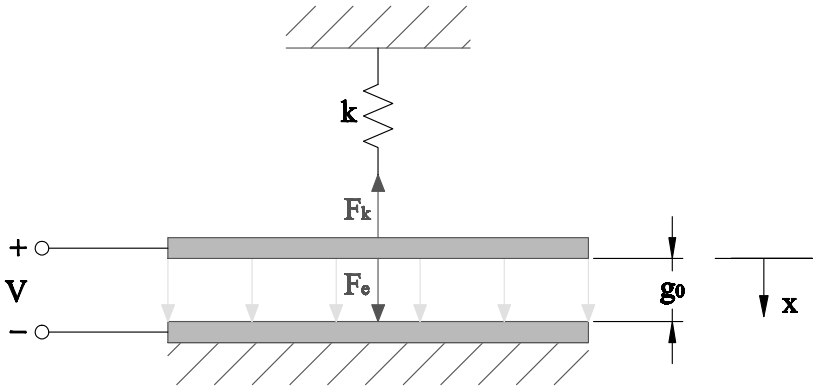

Figure 5.7: Schematic of an electrostatic actuator with a supporting spring force.

$$\delta F_{net} = \left.\frac{\partial F_{Net}}{\partial g}\right|_V \delta g = \left(\frac{\varepsilon A_a V_a^2}{g^3} - k\right)\delta g \tag{5.6}$$

In order for the system to be stable, $\frac{\partial F_{Net}}{\partial g}$ must be negative to insure that a positive perturbation, δg , does not result in further increase of the difference between the electrostatic force, F_e, and the spring force, F_k. In order to achieve this

$$k > \frac{\varepsilon A_a V_a^2}{g^3} \tag{5.7}$$

The specific gap where pull-in occurs is determined by inserting eq. (5.7) into eq. (5.5) and applying the equilibrium requirement, $F_{net} = 0$.

$$g_{pi} = \frac{2}{3} g_0 \tag{5.8}$$

By inserting eq. (5.8) into eq. (5.7), the pull-in voltage V_{pi} becomes

$$V_{pi} = \sqrt{\frac{8kg_0^3}{27\varepsilon A_a}} = \sqrt{\frac{8kg_0^3}{27\varepsilon w_a l_a}} \tag{5.9}$$

5.3.2 Beam deflection and equivalent spring constant

The tip deflection of a cantilever with a point load, is given as [24]

$$\delta_b = \frac{FL^3}{3EI} \tag{5.10}$$

where F is the force acting on the tip of the beam, L is the length of the beam, E is the Young's modulus of the beam material and I is the moment of inertia of the beam. The moment of inertia of a rectangular beam is

$$I = \frac{1}{12} w_b h_b^2 \tag{5.11}$$

where w_b is the width of the beam and h_b is the thickness of the beam.

The equivalent spring constant, k, for a cantilever beam with a rectangular cross section, can then be derived by combining eq. (5.4), (5.10) and (5.11).

$$k = \frac{E w_b h_b^3}{4L^3} \tag{5.12}$$

This spring constant is an important design parameter and is used throughout the mechanical modeling of a switch.

The pull-in voltage, V_{pi} [Eq. (5.9)], is a function of k. V_{pi} can be lowered by reducing the equivalent spring constant, k or increasing the electrode area, A_a. The initial gap, g_0, will also strongly influence V_{pi}. The initial gap is however often set by the isolation requirement of the RF application.

In order to reduce k, but at the same time not reduce actuation area, A_a, a beam with two widths may be implemented (Figure 5.1). This also reduces the curvature of the upper electrode during bending, which also results in a lower pull-in voltage. For a laterally activated cantilever, the same is achieved be controlling the height, h_b, of the beam.

The deflection equations for a given beam can be found by solving a set of differential equations [41]. To derive a deflection equation for a more complex beam, i.e. cantilever beam with two cross sections, the principle of superposition [24] can be implemented. The superposition principle says that the deflection, as a result of different loads acting simultaneously, can be calculated by summing the deflections caused by the individual loads.

Figure 5.8 shows the parameters and principle used to derive the deflection equation. The point where the load is located and the deflection is

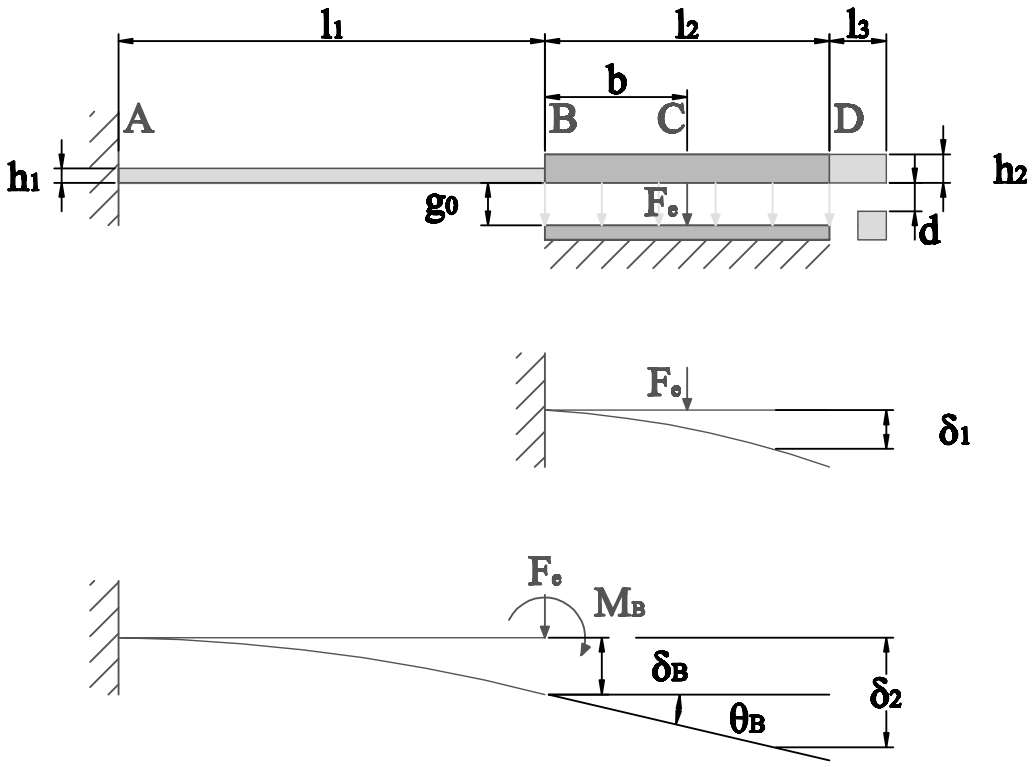

Figure 5.8: Schematic view of the beam.

calculated is given by the parameter b. Using this approach, the expression for the effective spring constant becomes more flexible.

The deflection at point C, assuming section BD is clamped at B [24]

$$\delta_1 = \frac{F_e b^3}{3E_2 I_2} \tag{5.13}$$

The deflection of section AB as a result of F_e and M_B [24]

$$\delta_B = \frac{F_e l_1^3}{3E_1 I_1} + \frac{F_e b l_1^2}{2E_1 I_1} \tag{5.14}$$

$$\theta_B = \frac{F_e l_1^2}{2E_1 I_1} + \frac{F_e b l_1}{E_1 I_1} \tag{5.15}$$

The contribution of the deflection of AB on BC

$$\delta_2 = \delta_B + \theta_B b \tag{5.16}$$

Total deflection at point C

$$\delta_C = \delta_1 + \delta_2 = \frac{F_e}{3E_1 I_1 E_2 I_2} \left(E_1 I_1 b^3 + E_2 I_2 (l_1^3 + 3bl_1^2 + 3b^2 l_1) \right) \tag{5.17}$$

The spring constant, k, of a structure supporting the upper plate of an electrostatic actuator, becomes

$$k = \frac{F_e}{\delta_C} = \frac{3E_1 I_1 E_2 I_2}{(E_1 I_1 b^3 + E_2 I_2 (l_1^3 + 3bl_1^2 + 3b^2 l_1))} \tag{5.18}$$

5.3.3 Effective Young's modulus for a layered cross-section

For a beam with two cross-sections consisting of one material, the Young's modulus is constant [$E_1 = E_2$ in eq. (5.18)]. The laterally actuated beam is however made up of a single crystal silicon beam and a cladding layer of metal (Figure 5.9). Calculating the deflection of such a beam can be quite complex as the Young's modulus varies through the thickness of the beam. There are however several methods to simplify such a calculation. One method,

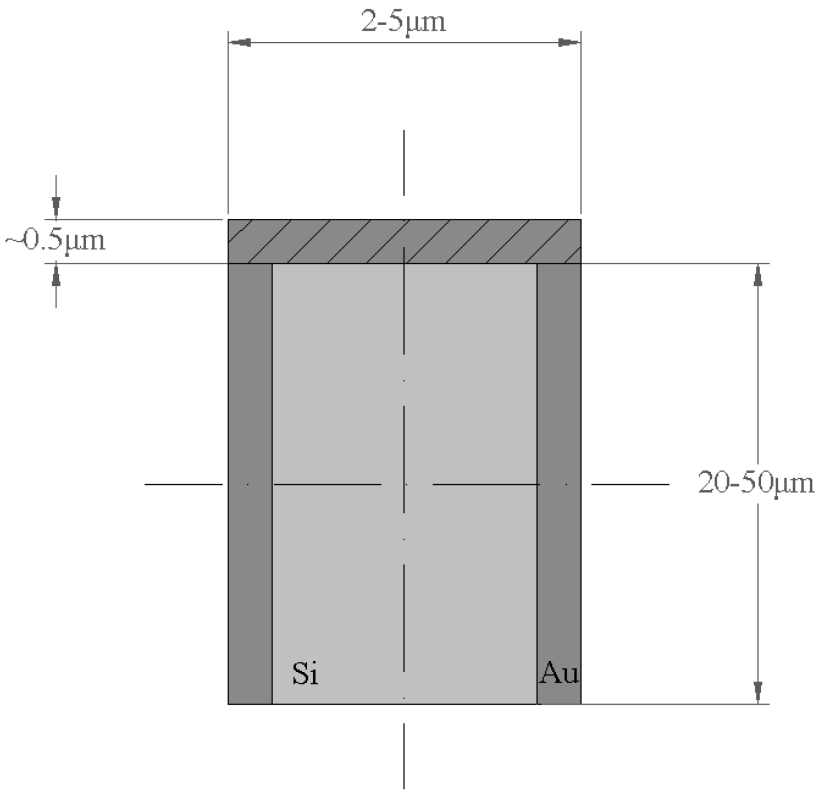

Figure 5.9: Cross section of a single crystal beam with a Au cladding layer.

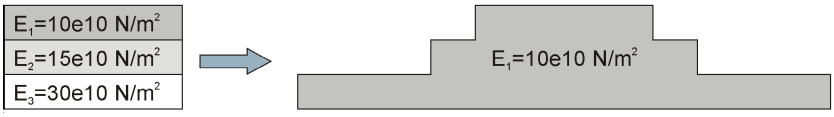

Figure 5.10: Implementation of an equivalent moment of inertia [9].

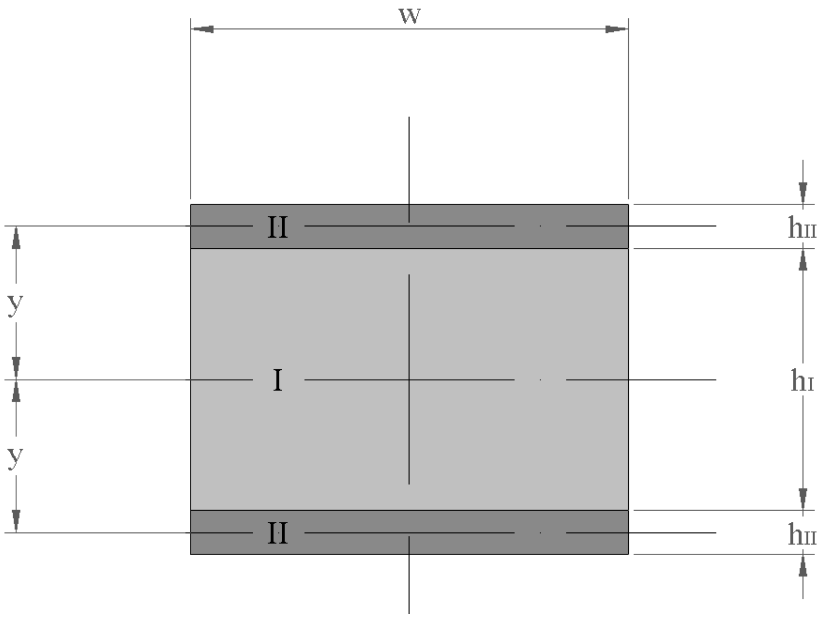

Figure 5.11: Cross-section of a symmetrical three layered beam. The cross-section has been rotated 90° compared to figure 5.9.

is to calculate an equivalent moment of inertia consisting of only one of the materials (Figure 5.10) [45].

Another method is to keep the original moment of inertia but calculate an effective Young's modulus, E_{eff}, [45] based on the Young's modulus and moment of inertia of the different layers.

For laterally actuated beam, implementing the effective Young's modulus is regarded as more practical. E_{eff} can also be implemented in FEM simulations avoiding the fine mesh for thin metal layers. Using this method, the overall stiffness of the beam will be correct. The stress through the cross section will however not be correct. This should be kept in mind.

The cladding layer is assumed to be thin compared to the height of the beam. For the dimensions given in figure 5.9, the contribution of highlighted section is therefore limited (2.5-1%) and is omitted from the analytical model given below. In addition, the Young's modulus for silicon ($E_{Si} \approx 169\ GPa$ [27]) is much larger then the Young's modulus for, i.e. Au ($E_{Au} \approx 60\ GPa$ [27]), further reducing the contribution of the highlighted section. If however the thickness of the cladding layer becomes comparable with the width of the beam, it must be taken into account.

The moment of inertia of the section I of the cross-section shown in figure 5.11, is given as

$$I_I = \frac{1}{12} w h_I^3 \tag{5.19}$$

In order to calculate the moment of inertia of the cladding layer, the parallel-axis theorem [24] is used.

$$I_{XY} = I_{XcYc} + Ay^2 \tag{5.20}$$

I_{XcYc} is the moment of inertia of an area with respect to its own centroid, A is the area, while y is the distance between the areas centroid and the overall cross-section centroid. The moment of inertia of the cladding layer becomes

$$I_{II} = \frac{1}{6} w h_{II}^3 + \frac{1}{2} w h_{II} (h_I + h_{II})^2 \tag{5.21}$$

The resulting moment of inertia of the of the entire cross-section becomes

$$I_{tot} = \frac{1}{12} w (h_I + 2h_{II})^3 \tag{5.22}$$

Further, the bending moment at any point along a beam is given as [41]

$$M = -\frac{d^2 v}{dx^2} EI = -\frac{1}{\rho} EI \tag{5.23}$$

where ρ is the radius of curvature of the beam. The radius of curvature will be the same for section I and II. As result, the total bending moment becomes the sum of bending moments of the individual beam layers.

$$M = -\frac{1}{\rho} E_I I_I - \frac{1}{\rho} E_{II} I_{II} \tag{5.24}$$

Implementing the concept of effective Young's modulus.

$$M = -\frac{1}{\rho} E_{eff} I_{tot} = -\frac{1}{\rho} (E_I I_I + E_{II} I_{II}) \tag{5.25}$$

The effective Young's modulus becomes

$$E_{eff} = \frac{E_I I_I + E_{II} I_{II}}{I_{tot}} \tag{5.26}$$

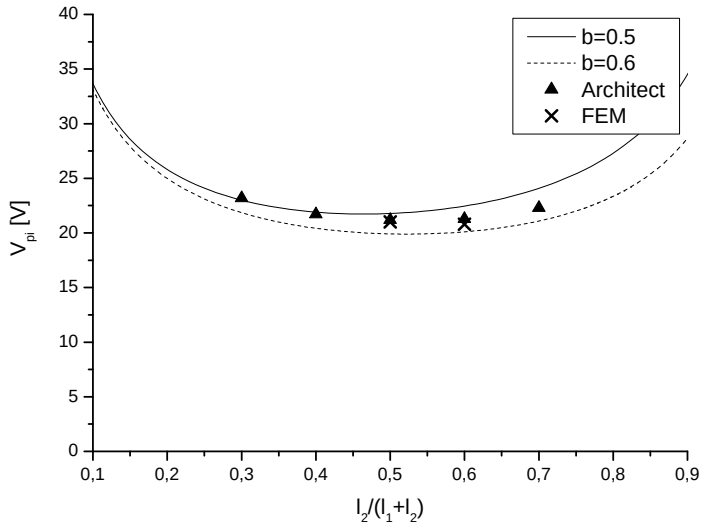

Figure 5.12: Calculated pull-in voltage V_{pi}.

Architect, which uses the equivalent moment of inertia method shown in figure 5.10, was used to verify the method. The results matched exactly for a number cladding layer thicknesses.

5.3.4 Pull-In voltage

In this section, the expressions derived above will be used to estimate the pull-in voltage for the beam given in table 5.1. The pull-in voltage is derived in section 5.3.1 and is given as

$$V_{pi} = \sqrt{\frac{8kg_0^3}{27\varepsilon A_a}} \tag{5.27}$$

As mentioned in section 5.3.1, the resulting electrostatic force, F_e, will move closer to the tip when the beam deflects. Figure 5.12 shows the calculated pull-in voltage for two different values for b together with results from Architect and FEM analyses.

For the given geometry the effect is small. However, if i.e. the initial gap, g_0, is large the effect can become important.

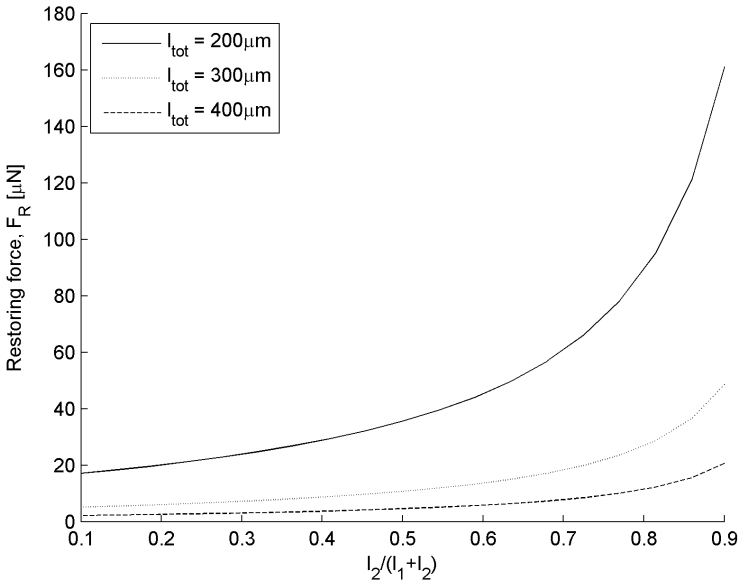

Figure 5.13: Calculated restoring force F_R.

5.3.5 Restoring force

When the actuation voltage is removed, the deformation of the cantilever beam results in a restoring force at the contact. In order to achieve high-reliability, the restoring force must be larger than any adhesive forces that can occur between the two contacts. According to [37] most switch designs have a restoring force between is 30-120 μN.

The restoring force at deflection, d, is equal to the point load on the tip needed to deflect the beam d. The restoring force can be written as

$$F = k_{tip} d \tag{5.28}$$

where k_{tip} is the equivalent spring constant at the tip and d is the initial distance between the upper and lower contacts (Fig. 5.8). To calculate k_{tip} eq. (5.18) is used with $b = l_2 + l_3$.

Figure 5.13 shows the calculated restoring force for several beam lengths.

5.3.6 Contact force

The contact force, F_{con}, is an important design parameter for a RF MEMS switch. Together with the material properties of the contact metal, the con-

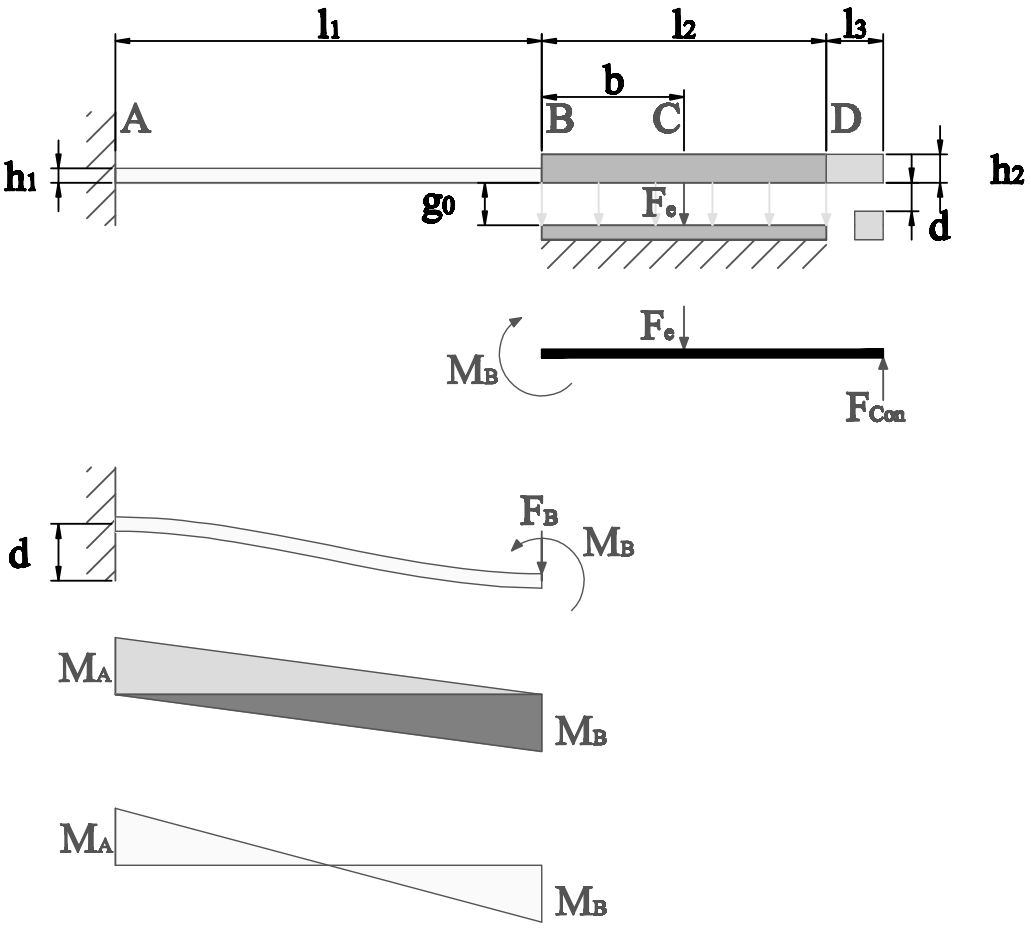

Figure 5.14: Cantilever beam in contact with the lower contact.

tact force determines the contact resistance and to some extent the reliability of the switch (Chapter 4).

Calculating F_{con} is complicated due to the electrostatic force and boundary conditions of the contacting beam. Pull-in of the electrode section will also occur at a given voltage, when section AB can not support the electrostatic force. A simplified method to estimate the maximum achievable contact force, F_{cmax}, will be derived here.

The method assumes that the beam has deflected to the point where section BD is parallel to the bottom electrode. For most geometries this point will never be reached, due to pull-in, but the method gives insight into how the F_{con} can be improved.

When the beam tip comes into contact, it is assumed that only section

AB deforms, $E_1I_1 << E_2I_2$. The deflection of the beam creates a negative bending moment, M_A, at point A.

$$M_A = -F_B l_1 \tag{5.29}$$

Equally a positive bending moment, M_B, will be generated at the interface between section AB and BD (Figure 5.14). At the point, when the upper electrode is parallel with the bottom electrode, section AB will be deflected symmetrically ($M_A = -M_B$). The bending moment at $l_1/2$ is therefore zero. As a result, the bending moment can also be calculated assuming a equivalent force located at $l_1/2$.

$$M_A = -M_B = -F_{Eq}\frac{l_1}{2} = -F_B l_1 \tag{5.30}$$

As a result

$$F_{Eq} = 2F_B \tag{5.31}$$

The deflection at $l_1/2$ can then be calculated using the following equation [24].

$$\delta = \frac{FL^3}{3E_1I_1} = \frac{F_B l_1^3}{12E_1I_1} \tag{5.32}$$

Assuming the two electrodes are parallel the deflection δ at $l_1/2$ becomes $d/2$. Solving eq. (5.32) with regard to the F_B

$$F_B = \frac{6E_1I_1d}{l_1^3} \tag{5.33}$$

The sum of moments around point B is

$$M_B = F_B l_1 = F_e\frac{l_2}{2} - F_{cmax}(l_2 + l_3) \tag{5.34}$$

Substituting eq. (5.33) into eq. (5.34) and solving for F_{cmax}

$$F_{cmax} = \frac{(2l_1 + l_2)}{(l_2 + 2l_3)}\frac{6E_1I_1d}{l_1^3} \tag{5.35}$$

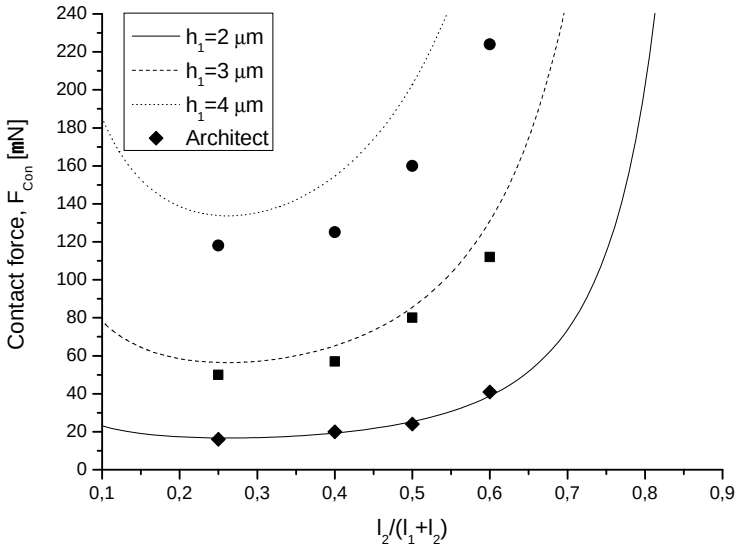

Figure 5.15: Calculated contact force F_{cmax}. ($t_m = 0$)

To determine the voltage when this condition occurs, eq. (5.3) is solved with respect to the voltage V

$$V_{cmax} = \sqrt{\frac{2F_e g^2}{e_0 A_a}} = \sqrt{\frac{2(F_B + F_{cmax})(g_0 - d)^2}{e_0 w l_2}} \tag{5.36}$$

where w is the width of the beam. Both F_B and F_{cmax} are linear functions of w. As a result, the voltage, V_{cmax}, is independent of the w (disregarding any fringing effect of the electric field). Hence, F_{cmax} can be increased without increasing the actuation voltage by increasing the width of the beam. Reducing the gap $(g_0 - d)$, is also an very efficient way to increase the contact force.

Figure 5.15 shows the calculated contact force together with results calculated using Architect. The two methods correlate, especially for a low stiffness, but it is clear that the derived method overestimates the contact force.

The corresponding actuation voltage, V_{cmax}, is given in figure 5.16. The two calculation methods used, show the same trend but it is clear that the derived method underestimates V_{cmax} by a factor $f_u = 1.1 - 1.4$. Based on Architect analysis, the factor is seen to be approximately independent of the beam height, h_1, for a given beam length $(l_1 + l_2)$ and electrode length

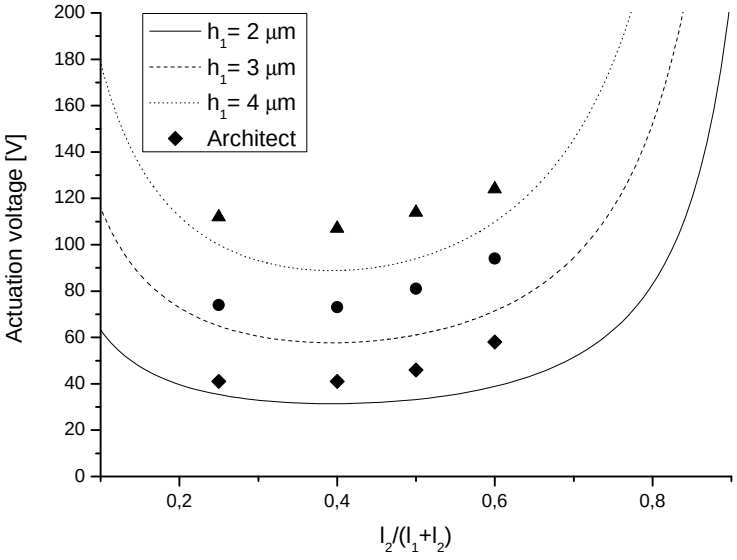

Figure 5.16: Calculated actuation voltage V_{cmax}. ($t_m = 0$)

(l_2). This is due to the angle of the upper electrode being approximately independent of h_1 for a given beam length.

The derived method shows that the contact force F_{con} can be increased drastically by carefully selecting the stiffness of section AB, the ratio $l_2/(l_1 + l_2)$ and the total beam length $l_1 + l_2$.

To reduce the pull-in voltage, it can be tempting to reduce the stiffness of section AB. If however V_{cmax} for is lower than the original pull-in voltage V_{pi}, the beam will not become stable after contact and collapse directly down on the bottom electrode.

Calculating the contact force as a function of actuation voltage can be performed using Architect. Figure 5.17 shows the calculated contact force for two geometries. As an alternative, the factor f_u can be adjusted based on results from Architect or FEM analysis, and a second order polynomial can be fitted using F_{cmax}, V_{cmax} and V_{PI} as boundary conditions.

5.3.7 Resonance frequency

The resonance frequency is given as

$$\omega_0 = 2\pi f_0 = \sqrt{\frac{k}{m_{eff}}} \tag{5.37}$$

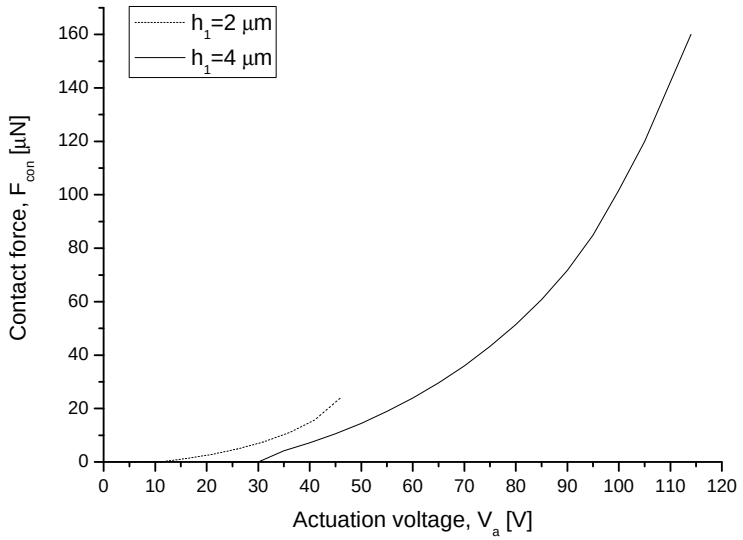

Figure 5.17: The contact force F_{Con} as a function of the actuation voltage. ($t_m = 0$)

where k is the equivalent spring constant and m_{eff} the effective mass.

The effective mass of the cantilever beam can be estimated by applying several assumptions. Figure 5.18 shows the simplified structure used. Section AC is a beam with the same dimensions as section AB, supporting a mass equivalent to section BD. The effective mass of the a cantilever beam AC is [35].

$$m_{eff} = 0.23 m_{AC} \tag{5.38}$$

As section BD oscillates about its own mass center, the effective mass for

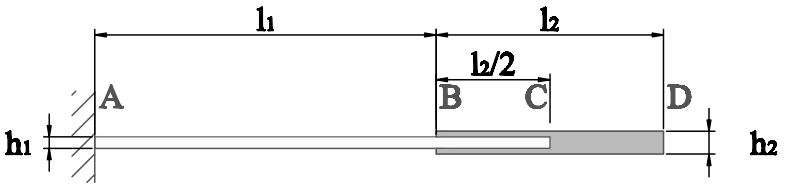

Figure 5.18: Schematic view of the structure used to estimate the effective mass m_{eff}

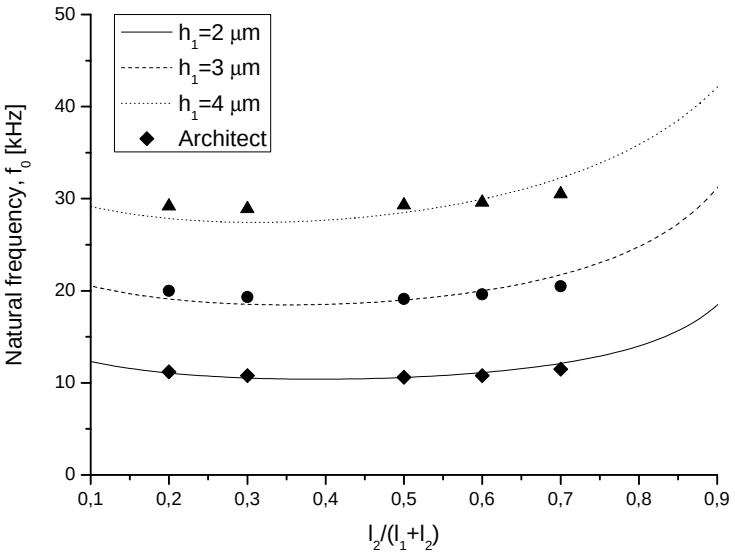

Figure 5.19: The calculated resonance frequency using analytical method and Architect

.

the simplified structure becomes

$$m_{eff} = m_{BD} + m_{effAC} = m_{BD} + 0.23 m_{AC} \tag{5.39}$$

The beam in this case consist of a silicon core and a metal cladding layer (Figure 5.11). Instead of calculating the mass of the different layers individually, an effective density for the cross-section can be used.

$$\rho_{eff} = \frac{\rho_I h_I + 2\rho_{II} h_{II}}{h_I + 2h_{II}} \tag{5.40}$$

The estimated the resonance frequencies, f_0, for three geometries are given in figure 5.19. The results agree well with the values calculated using Architect. The analytical method however, shows a somewhat increase in ω_0 for increasing $l_2/(l_1 + l_2)$. This assumed to be due to the assumption that section BD is only a mass supported by section AC.

5.3.8 Damping and quality factor

RF MEMS switches are usually designed to operate in an inert gas ambient at atmospheric pressure. This is to reduce unwanted transient mechanical

oscillations and oxidation/ contamination of contact surfaces. As result, when the cantilever beam is actuated toward the bottom electrode the gas must flow out of the way, causing energy dissipation or damping. If the actuation is done sufficiently fast, the gas will not have time to flow away resulting in an opposing spring force in addition to the dissipating effect [21]. This effect is called squeeze-film damping.

The Knudsen number is a measure of the number collisions between the gas molecules and its surroundings in the gap

$$K_n = \frac{\lambda}{g} \tag{5.41}$$

The parameter, λ, is the mean free path of the gas and g is the gap height. The mean free path for common gases used in MEMS packaging is 0.07-0.09 μm at standard pressure and temperature (STP) [37, 41].

The viscosity of a gas, μ, is a measure of its internal resistance to flow and is $1.845 \cdot 10^{-5} Pa\ s$ at STP for ideal gases [37].

A small Knudsen number $K_n \ll 0.1$, indicates that there are many collisions. In this case, the flow can be said to be viscous and a no-slip boundary condition can be used to describe the flow. The no-slip boundary conditions implies that the flow velocity is zero at the walls, which results in a parabolic flow profile in the gap (Poiseuille flow) [41].

When λ becomes comparable with g ($K_n \approx 0.1$), the collisions at the wall are reduced. The flow is no longer viscous and the no-slip condition is no longer valid. As a result, the gas molecules can travel a significant fraction of the the gap, g, without experience a collision. At this point the gas flow can be modeled using a effective viscosity μ_{eff} [21].

$$\mu_{eff} = \frac{\mu}{1 + 9.638 K_n^{1.159}} \tag{5.42}$$

Figure 5.20 shows how μ_{eff} is reduced as the K_n increases.

A parameter that is important when calculating the dynamic response of a system, is the quality factor. It is defined as the ratio between energy stored in a system to energy dissipated per cycle. For this application it can be expressed as [37]

$$Q = \frac{k}{\omega_0 b} \tag{5.43}$$

where ω_0 is the resonance frequency and b the damping coefficient.

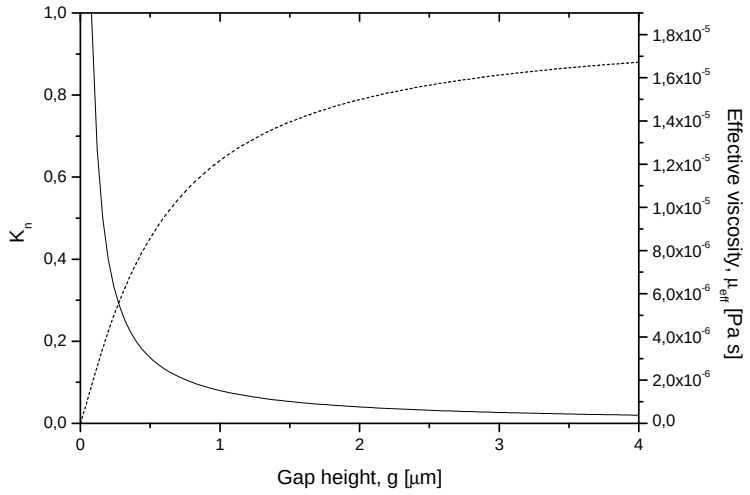

Figure 5.20: The effective viscosity, μ_{eff}, and the Knudsen number, K_n, as a function of gap height, g.

The small displacement damping coefficient, b, for a rectangular parallel plate geometry, is given as [37]

$$b = \frac{3}{2\pi}\frac{\mu(wl)^2}{g_0^3} \tag{5.44}$$

This equation is however not directly applicable due to how a cantilever beam deflects. However, a rough estimate can be calculated by assuming that only the electrode section, BD, of the beam is damped. Figure 5.21 shows the calculated quality factor using the estimated damping coefficient (Method # 1). When $l_2/(l_1 + l_2) \to 0$ the method is invalid as $b \to 0$.

A better approximation of the quality factor of a cantilever beam is given as [32]

$$Q = \frac{\sqrt{E\rho}h^2}{\mu(wl)^2}g_0^3 \tag{5.45}$$

This method however, implements a cantilever beam with a constant cross-section. The cantilever beam proposed in this thesis has a constant width, w, but two different heights h_1 and h_2, where $h_1 < h_2$. This implies that that the quality factor Q will be higher compared to a beam with a constant height h_1. Eq. (5.45) is therefore assumed to be conservative and will be used

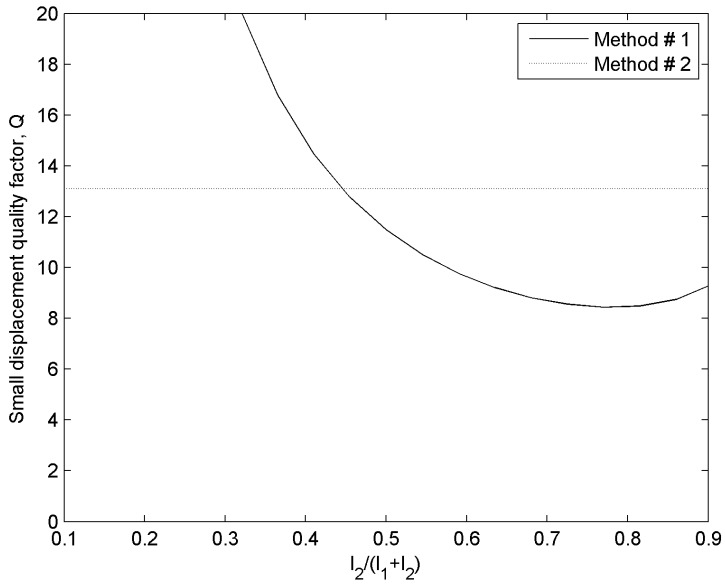

Figure 5.21: Calculated quality factor Q using eq. (5.43) (Method # 1) and eq. (5.43) (Method # 2). ($h_1 = 3\mu m$, $t_m = 0\mu m$)

to estimate the quality factor.

The damping coefficient, b [Eq. (5.44)], is a strong function of the initial gap, g_0. When the switch is actuated this gap will be drastically reduced. To correct the damping coefficient for this large displacement, it has been proposed to multiply the damping coefficient with the following function (Figure 5.22) [40].

$$f_d = \left(1.0 - \left(\frac{x}{g_0}\right)^2\right)^{-(3/2)} \tag{5.46}$$

where x is the deflection from the initial gap g_0.

Implementing the effective viscosity [Eq. (5.42)] and the large displacement correction factor, the quality factor, Q, becomes

$$Q = \frac{\sqrt{E\rho}h^2 g_0^3}{\mu_{eff}(wl)^2} f_d^{-1} \tag{5.47}$$

Figure 5.23 shows how the corrected quality factor is reduced with the closing gap. This increased damping effect is the so called squeezed film damping.

For a lateral switch fabricated using either of the processes described in

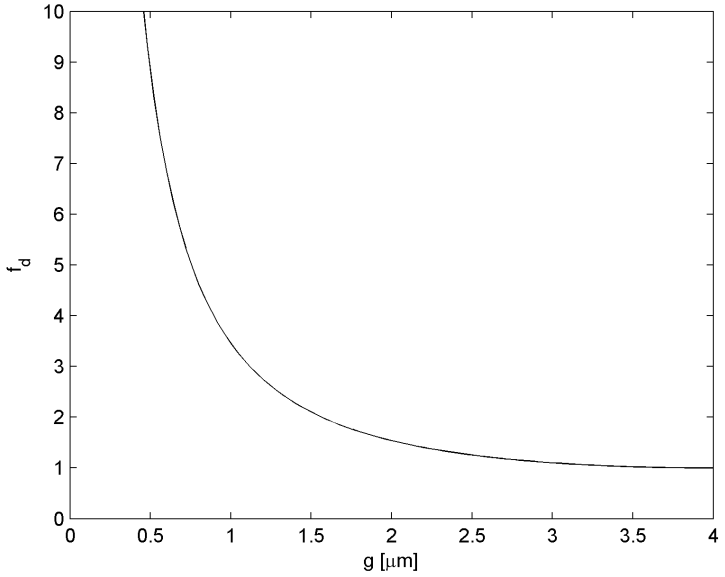

Figure 5.22: Correction function for the damping coefficient given a large displacement

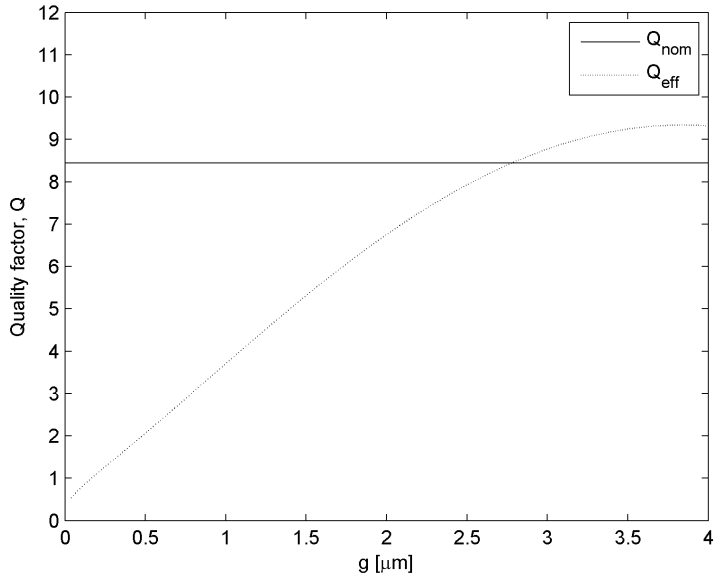

Figure 5.23: The small displacement quality factor Q_{nom} (eq. 5.45) and the corrected quality factor Q_{eff}.

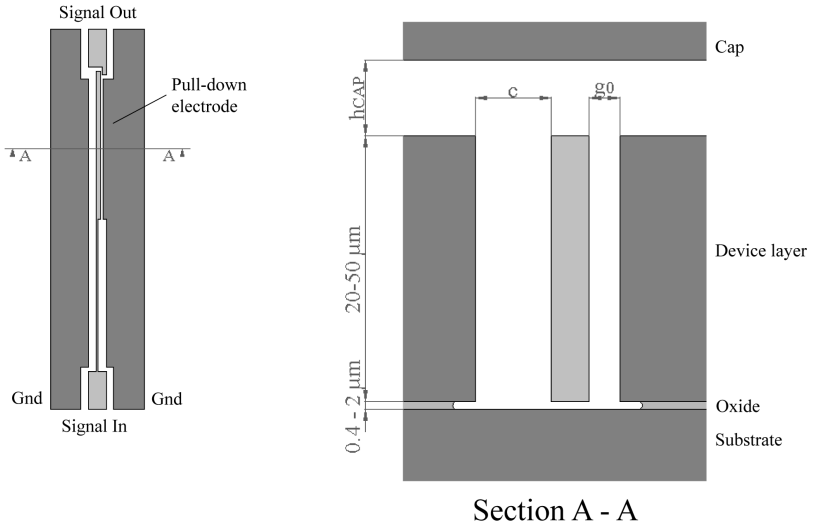

Figure 5.24: A laterally actuated RF MEMS switch fabricated in a SOI process

section 3.3, the damping effect will be further increased due to the restricted gas flow to one side of the beam. The effect is shown in figure 5.24. As the length of the electrode, l_2, is generally larger then the width, w, this effect becomes is important. In the case of a vertically actuated cantilever beam, the gas underneath the beam can typically flow outward in all directions.

Assuming the gas flow through the bottom gap is negligible, the gas flow pattern will be similar to that of a beam with double width. As a rough approximation an effective width $w_{eff} = f_{eff}w$ where $f_{eff} = 1 - 2$ can be implemented for section BD. Given eq. (5.43) and (5.44) this will reduce the quality factor Q by a factor $1/f_{eff}^2$.

During design it is also important to take into account the gap c and the cap clearance h_{Cap}. If the gap c is small, additional damping can occur due to restricted gas flow into the gap when the beam is actuated. In addition, h_{Cap} should be sufficient to allow the displaced gas to flow in and out of the gaps without becoming constricted etc.

The additional damping effect can be reduced by defining lateral channels in the surrounding structure. However, making such channels in the electrode reduces the actuation area.

5.3.9 Switching time

The definition of switching time in literature is somewhat confusing. Traditionally, switching time is used to represent the time for switching from

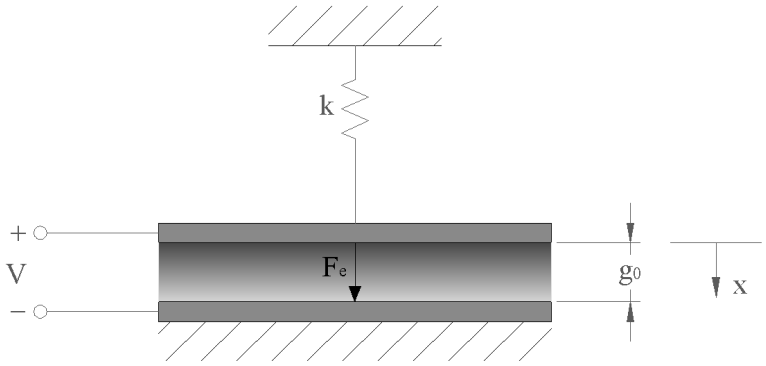

Figure 5.25: A schematic view of a simplified model of a electrostatic actuated switch

up to down-state as result of actuation. Release time is defined as the time the switch uses to return from down to up-state, and is usually much longer. However, switching time is also sometimes used for both. In this thesis the actuation time will be used to represent switching from up to down-state, while switching time will be used as a general term.

The switching time is strongly dependent on a number of parameters e.g. beam stiffness, viscous damping and actuation voltage. Optimizing a switch with regard to the switching time may however have detrimental effect on other design parameters e.g. actuation voltage, isolation etc. In this section a model to estimate the actuation and release time will be presented.

A simplified 1-D model of an electrostatic actuated cantilever switch is given in figure 5.25. The differential equation for the model is

$$m\frac{d^2x}{dt} + b\frac{dx}{dt} + kx = F_e(x) \tag{5.48}$$

where m is the effective mass of the upper electrode and its supporting structure [Eq. (5.39)], b the viscous damping, k the equivalent spring constant of the supporting structure [Eq. (5.18)] and F_e the electrostatic force [Eq. (5.3)]. The viscous damping can be calculated based on the corrected quality factor

$$b = \frac{k}{\omega_0 Q_{eff}} \tag{5.49}$$

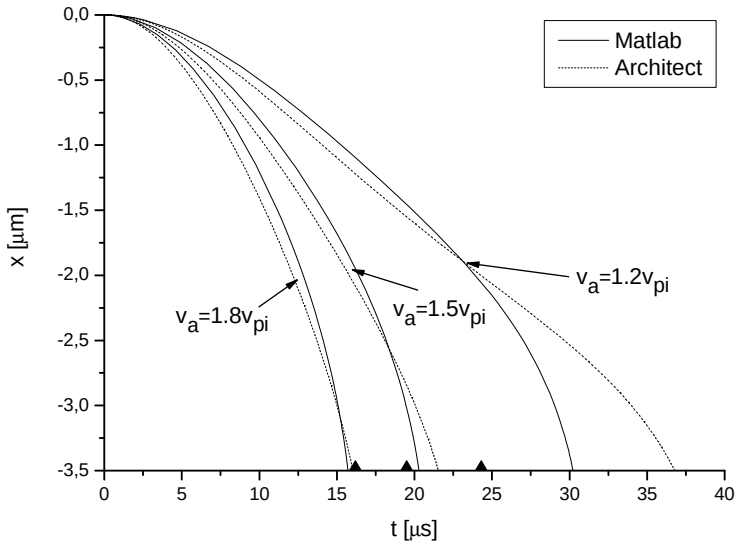

Figure 5.26: Actuation time simulated using eq.(5.48) and Architect.

In order to calculate the actuation time, the differential equation can be solved implementing the initial conditions $x(0) = 0$ and $\frac{dx}{dt}(0) = 0$. Similarly, the release time can be calculated by setting the right hand side equal to zero and solving using $x(0) = d$ and $\frac{dx}{dt}(0) = 0$.

Figure 5.26 shows the response of the cantilever beam versus actuation voltage V_a. For the given beam geometry $V_{pi} = 20V$. For a sufficiently high V_a, the response simulated using eq. (5.48) and Architect agree. However, when V_a approaches V_{pi} the simulated responses using Architect is slower. This is likely a result of the different methods used to model the damping and the simplified parallel plate actuator model implemented in eq. (5.48).

A simple method to estimate the actuation time if $Q > 2$ (small damping coefficient) is proposed in [37]. This method assumes that the actuation time is inertia limited and the damping, $b \sim 0$. Further, the electrostatic force is assumed to be constant.

$$t_a \simeq 3.67 \frac{V_{pi}}{V_a \omega_0} \tag{5.50}$$

The estimated actuation time is indicated on the x-axis in figure 5.26. For sufficiently high actuation voltage, $V_a > 1.8V_{pi}$, the estimated actuation time correlates well with the other two methods. Eq. (5.50) may therefore be used,

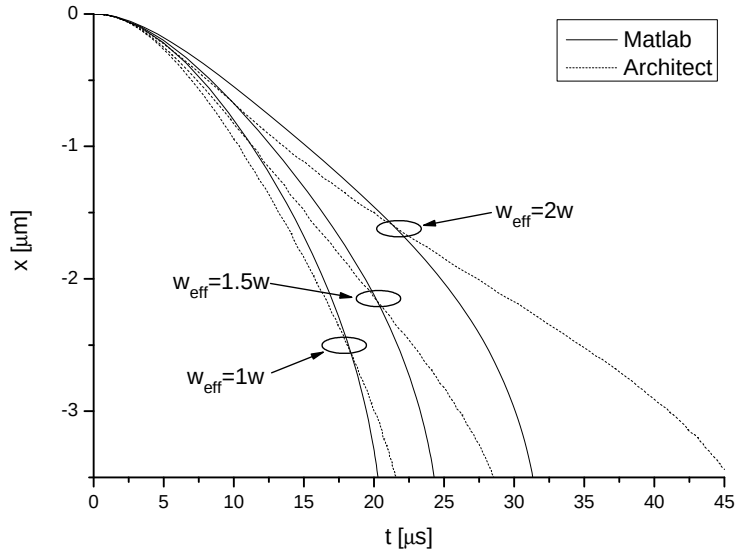

Figure 5.27: Simulated actuation time for three effective beam widths, w_{eff}. ($V_a = 1.5V_{pi}$)

for example, in the early design phase.

As discussed in section 5.3.8, the damping effect will be increase due to the restricted gas flow on the substrate side of the beam (Figure 5.24). The simulated response for three effective beam widths, w_{eff}, is given in figure 5.27. The increased damping results in a larger difference between the response simulated using Architect and simplified model, eq. (5.48). The results calculated using Architect show a quicker response in the first part of the cycle, compared to the simplified model, but a slower response as the gap is reduced.

When the cantilever beam makes contact it posses kinetic energy. As a result, the switch bounces several times increasing the actuation time. The amount of bouncing is a function of the kinetic energy, damping and actuation voltage and can increase the actuation time by $20 - 100\%$ [38]. Modeling of the bouncing effect is not performed in this thesis.

The release response is shown in figure 5.28 and can roughly estimated as [38]

$$t_r \simeq \frac{1}{2\pi\omega_0} \tag{5.51}$$

For the given geometry and gas parameters, the cantilever beam is clearly

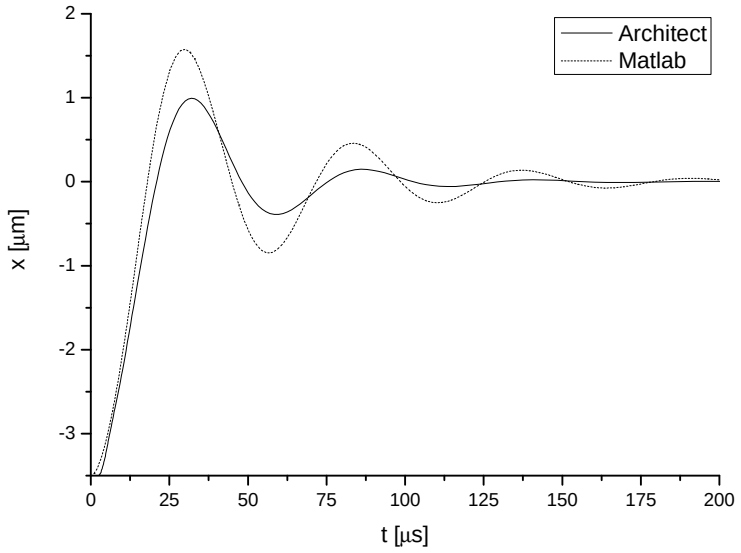

Figure 5.28: Simulated release time.

under damped as it continues to oscillate about its equilibrium position. This is undesired as the release time is greatly increased.

Figure 5.29 shows the release response implementing an effective width, w_{eff}. The increased damping results in an approximately critically damped system for $w_{eff} = 1.5w$ and a over damped system for $w_{eff} = 2w$. The Architect results show also here a larger damping effect compared to the simplified model.

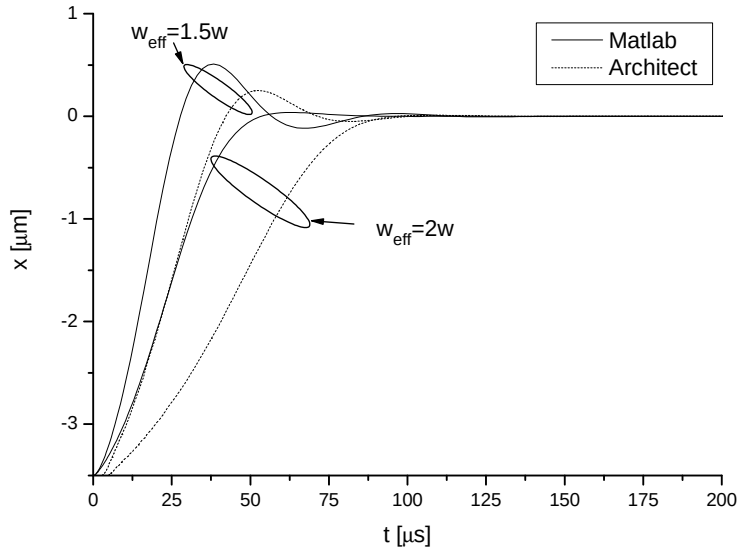

Figure 5.29: Simulated release time for two different effective beam widths, w_{eff}.

Chapter 6

RF modeling

6.1 Introduction

The DRIE based fabrication technique described in section 3.3 allows the switch to be fabricated as an integral part of a transmission line with few process steps. The switch concept proposed in [11] incorporates the switch into a coplanar waveguide (CPW) (Figure 6.1) transmission line (t-line). Figure 6.2 shows a sketch of the concept, where the cantilever beam is part of the signal line and one of the ground planes is extended towards the beam, acting as the actuation electrode. The actuation is achieved by superimposing a bias voltage on the signal.

CPW t-lines are finding extensive applications in microwave integrated circuits (MIC), due to increased flexibility in circuit design and improved performance for some circuit functions [3, 22]. The coplanar strip (CPS) is another promising configuration (Figure 6.1). The coplanar t-lines are often preferred at higher frequencies as the ground plane is brought to close proximity of the signal line. This reduces attenuation of the signal by reducing dielectric and radiation losses. Another positive property of the coplanar t-lines is that the characteristic impedance, Z_0, of t-line can be well controlled, by adjusting the parameters S and W in figure 6.1.

For the CPW, applying the bias voltage on the signal line can however be difficult as the signal line is enclosed by the two ground planes. The biasing can be achieved by e.g. bridging the ground planes or utilizing vias [43]. Alternatively, the switch can be fabricated as a CPS t-line transmission line. This will however have an adverse affect on the RF characteristics, increasing the resistance and reducing the confinement of the electric field.

Figure 6.3 shows three applicable t-line configurations and their respective current distribution caused by the concentrated electric field between the

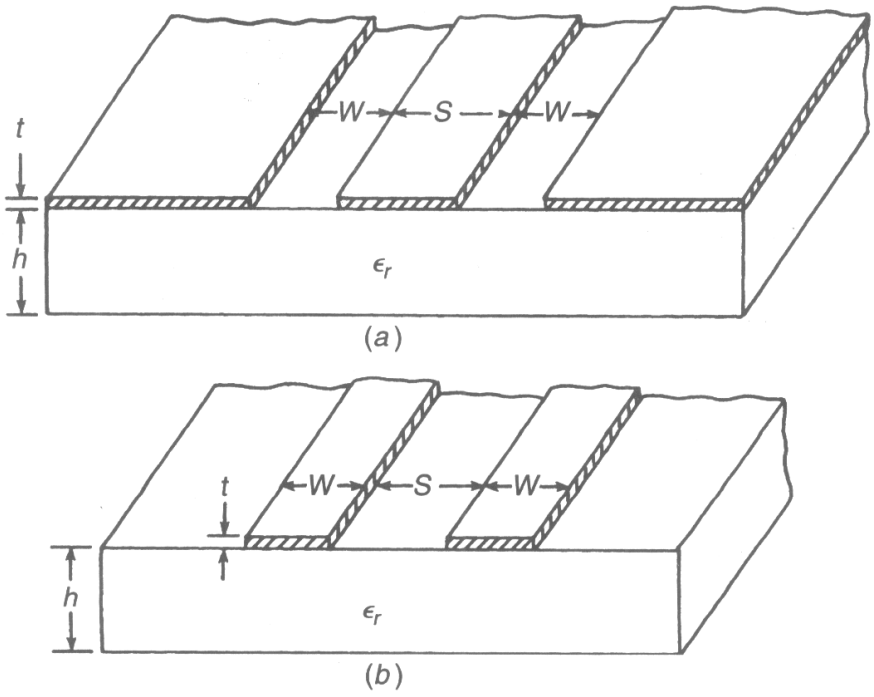

Figure 6.1: Coplanar waveguide (a) and a coplanar strip transmission line (b). (From [3])

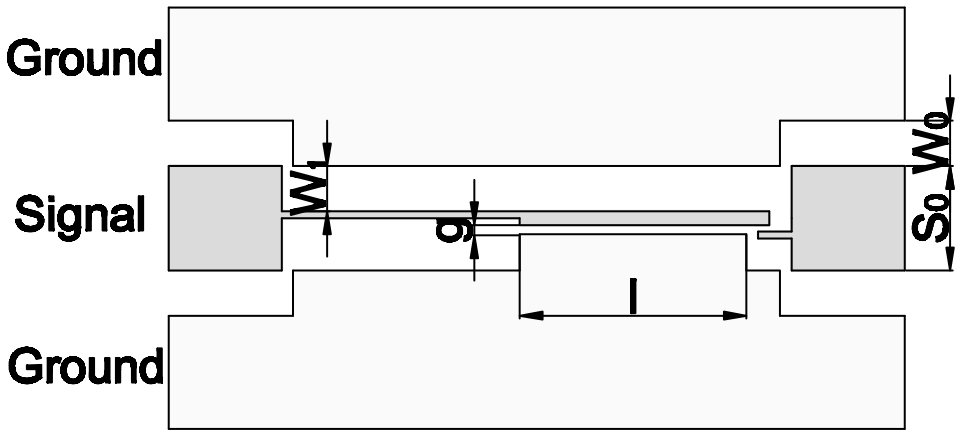

Figure 6.2: The concept of the series switch incorperated in a CPW transmission line.

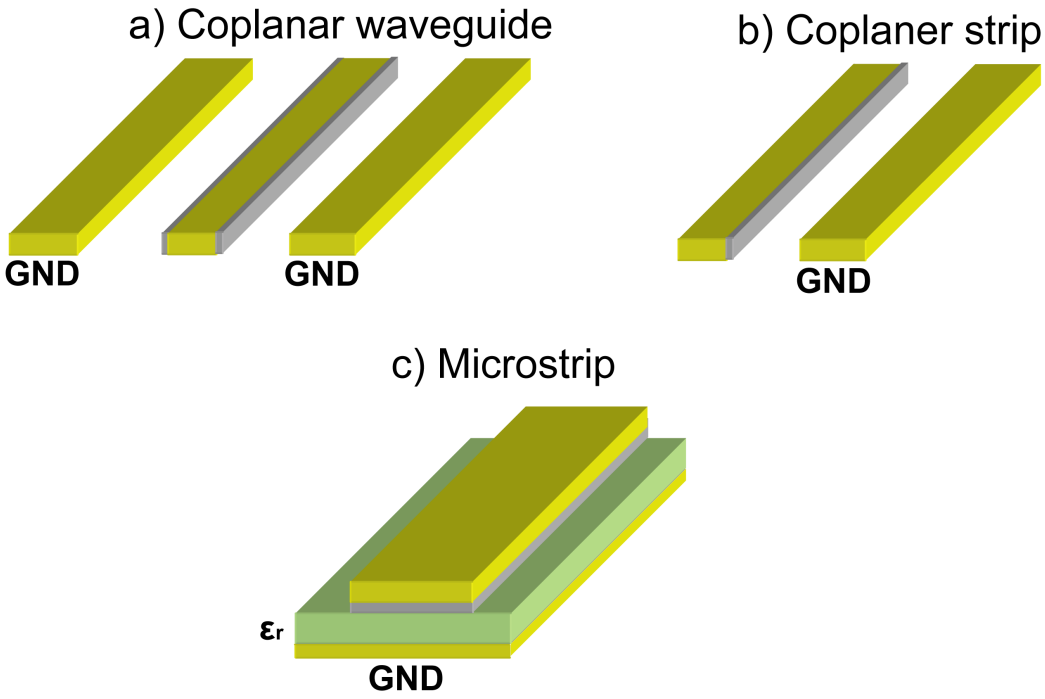

Figure 6.3: Current distribution for CPW, CPS and microstrip transmission lines.

ground plane and signal line. For the CPW and CPS t-line the current will be concentrated on the edges/ edge of the signal line. The conduction loss is therefore a function of the thickness of the signal line and the skin depth [Eq. (6.2)]. For the microstrip t-line the conduction loss is a function of the width of the signal line and skin depth. A lateral switch fabricated using DRIE is therefore most suited to be implemented as either a CPW or CPS configuration, as the thickness of the device layer becomes the signal line thickness.

Methods to model and analyze the RF performance of the CPW switch concept shown in figure 6.2 will be presented in this chapter, but can be easily adapted to be valid for a CPS t-line.

6.2 Modeling approach

The RF performance of the switch was analyzed using an equivalent circuit. The parameters of the equivalent circuit were determined using both analytical methods and numerical techniques.

For devices presented in literature, more accurate analysis using full wave

electromagnetic simulation software (i.e. HFSS [7]) are generally performed in addition. This will not be performed in this thesis.

6.2.1 Analytical methods

The analytical methods presented in this chapter were incorporated into MATLAB® functions. This way the analytical expressions could be better understood and a number of parameters could be varied effectively.

The use of only analytical methods is however somewhat limited due to the complex nature the coupled electric and magnetic fields.

6.2.2 Numerical methods

The ANALYZER module of CoventorWare® was both used to adjust the analytical methods and calculate several of the equivalent circuit parameters. More details on the analysis approach using CoventorWare is given in section 5.2.

The ANALYZER MemElectro solver was used to calculate the capacitance between the different structures. MemElectro analyzes electrostatics using a boundary element method (BEM). This is a simplification of the finite element method (FEM) where only the surface of the structure is used in the calculations, as opposed to the volume for FEM.

The frequency dependent resistance and inductance of the switch was estimated using the MemHenry solver. The accuracy of the solver for this application is however assumed to be reduced as a ground plane can not be defined. The MemHenry solver also implements BEM but divides the volume of the conductor into filaments, in order to capture the skin effect [30] (Figure 6.4). The meshing therefore becomes less important.

6.3 Equivalent circuit

A series switch can be modeled using a transmission line equivalent circuit to represent the beam, and a series capacitor or series resistance to represent the contact in respectively up-state and down state [11, 37]. Figure 6.5 shows the equivalent circuit used. The shunt conductance usually included in a transmission line equivalent circuit, is not included as the loss through the buried oxide/ handle wafer is assumed to be limited [11].

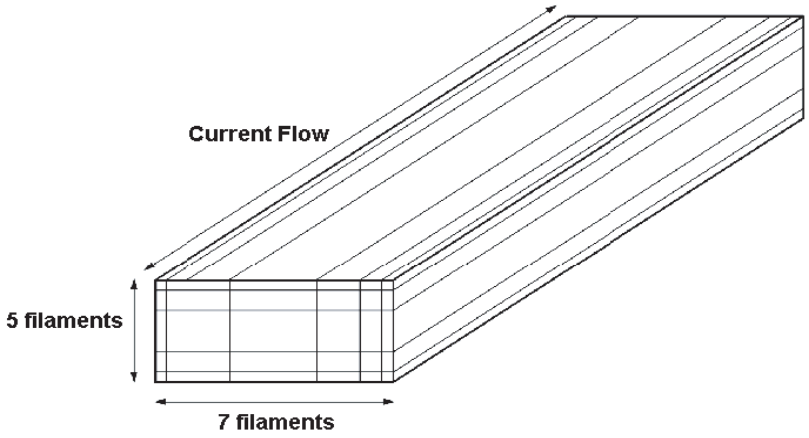

Figure 6.4: Refinement of the volume of the conductor. (From [8])

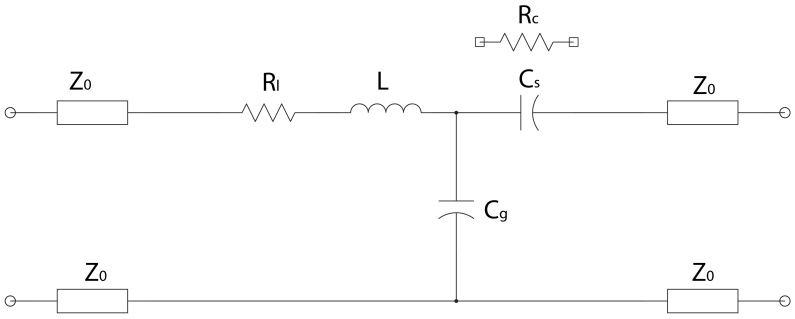

Figure 6.5: Equivalet circuit of the switch.

6.3.1 Beam series resistance

The beam series resistance, R_l, is the resistance of the beam, which consist of a silicon core and a metal cladding layer (Figure 5.9). As the conductivity of the metal cladding layer ($\sigma = 4.4 \cdot 10^{13}\ pS/\mu m$) is much higher than the conductivity of the silicon core ($\sigma = 1 \cdot 10^{9}\ pS/\mu m$), only the metal layer is used to calculate the resistance. Below a certain frequency the series resistance can be calculated as

$$R_l = \frac{l}{\sigma_{metal} A} = \frac{l}{2\sigma_{metal} w t_m} \tag{6.1}$$

where σ_{metal} is the conductivity, w the width of the beam and t_m the thickness of the metal cladding layer.

At higher frequencies, the alternating magnetic and electric field cause the current flow to reside at the outer perimeter of a conductor. This is called the skin effect and the skin depth can be calculated as [30]

$$\delta = (\pi f \mu \sigma_{cond})^{-1/2} \tag{6.2}$$

where μ is the permeability ($4\pi \cdot 10^{-7}\ H/m$). The skin depth for Au as a function of frequency is shown in figure 6.6. When the skin depth, δ, becomes smaller than t_m, the effective conduction thickness will be reduced.

In addition, the current density will be higher at the top and bottom of the beam, effectively reducing the conductor width, w. This effect is shown in figure 6.7. The corrected resistance can be calculated as

$$R_l = \frac{l c_w}{2\sigma_{metal} w \delta} \qquad \text{for } \delta(f) < t_m \tag{6.3}$$

where c_w factor is an experimental factor used to reduce the conductor width. For a beam width 35 μm, $c_w \approx 2$, using MemHenry. Figure 6.8 shows the calculated resistance using eq. (6.1) and (6.3) together with the resistance calculated using MemHenry. The methods show good correlation.

The resistance of the t-line sections at the input and output of the switch should also be included in the total series resistance of the switch.

6.3.2 Series capacitance

As mentioned in section 2.2, the upper operating frequency of a series RF MEMS switch is typically limited by the up-state capacitance. When the switch is in the up-state a series capacitance is generated between the beam

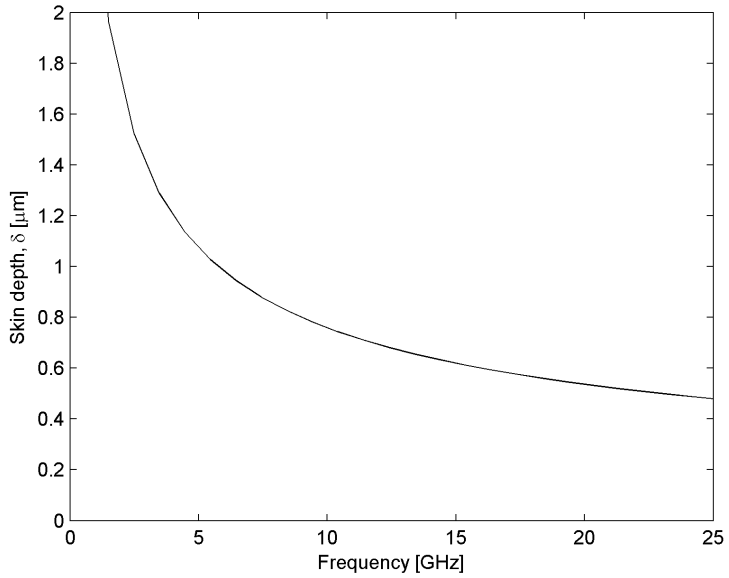

Figure 6.6: Skin depth of Au.

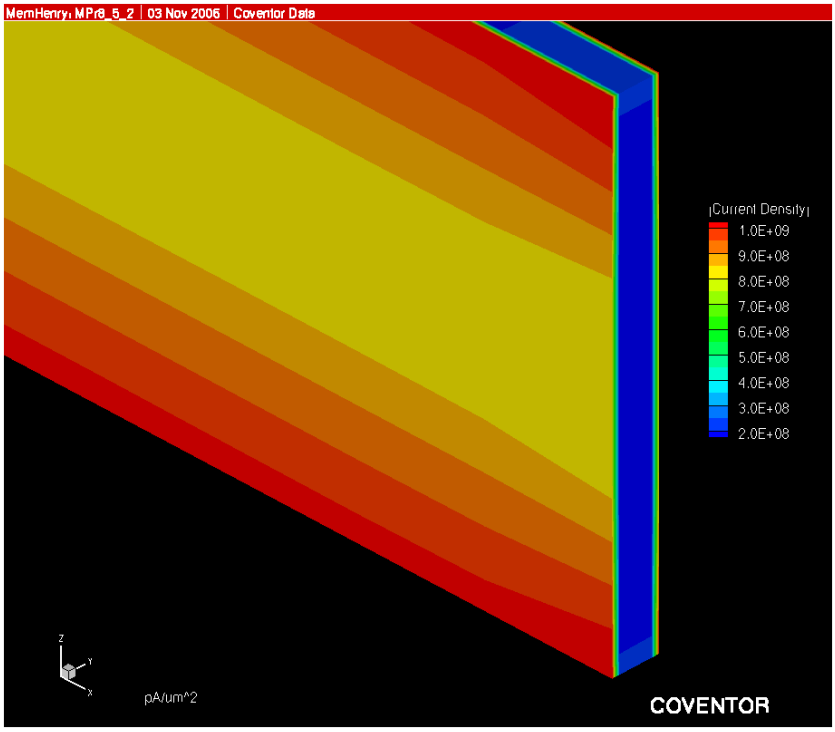

Figure 6.7: Cross-section of the beam showing current density.

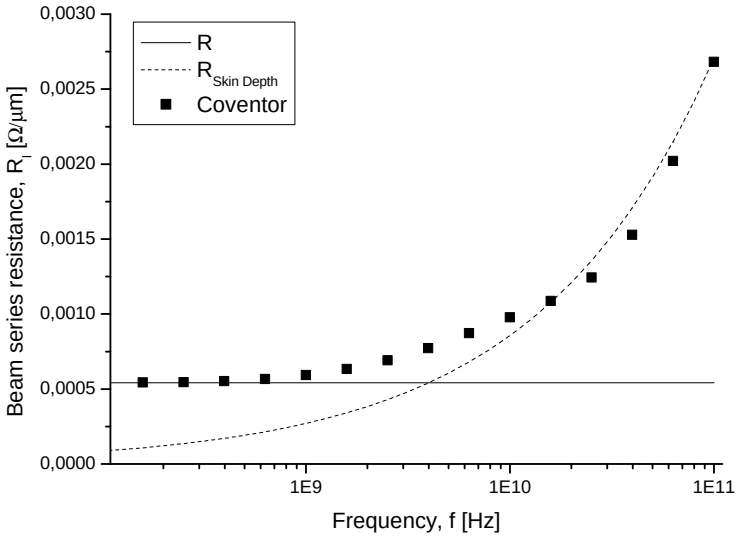

Figure 6.8: The distributed contact resistance as a function of frequency.($w = 35\ \mu m$, $t_m = 0.6\ \mu m$)

tip and the signal line (Figure 6.9). Given a sufficiently high frequency, this series capacitance will cause the signal to leak through the switch.

The capacitance between the beam and lower contact will be dominated by fringing capacitance as the overlap, l_0, is fairly small. Figure 6.10 shows the capacitance simulated using MemElectro for two different gaps, d. As expected, the capacitance becomes more sensitive to the overlap for a smaller gap, d. The effect of the beam width on the capacitance was also simulated and showed an approximate linear relation for the width range $20 - 65\ \mu m$.

Another component of the series capacitance will occur between the beam tip and the main part of the signal line. This capacitance was simulated for a varying distance, X_{end}, and is presented in figure 6.11.

The total series capacitance will be the sum of these two parallel capacitances. Depending on the design, additional coupling capacitances through the substrate or between the two main signal lines may also need to be included [37]. The addition of a contact dimple on the upper or/ and lower contact will also increase the series capacitance.

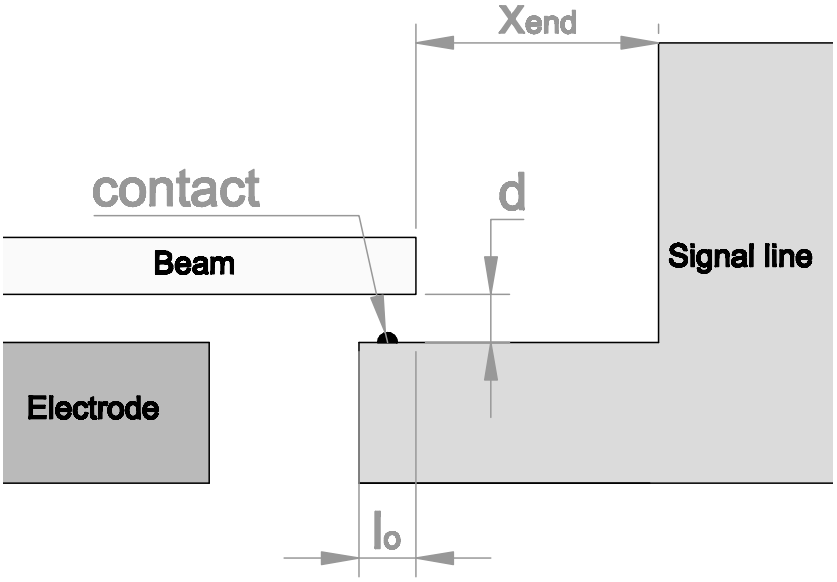

Figure 6.9: Cantilever beam tip and surrounding structure.

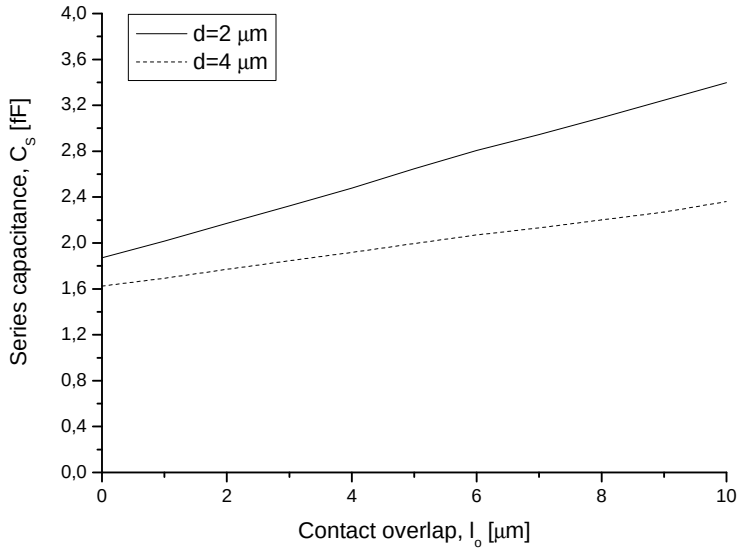

Figure 6.10: Series capacitance as function of the overlap l_0.

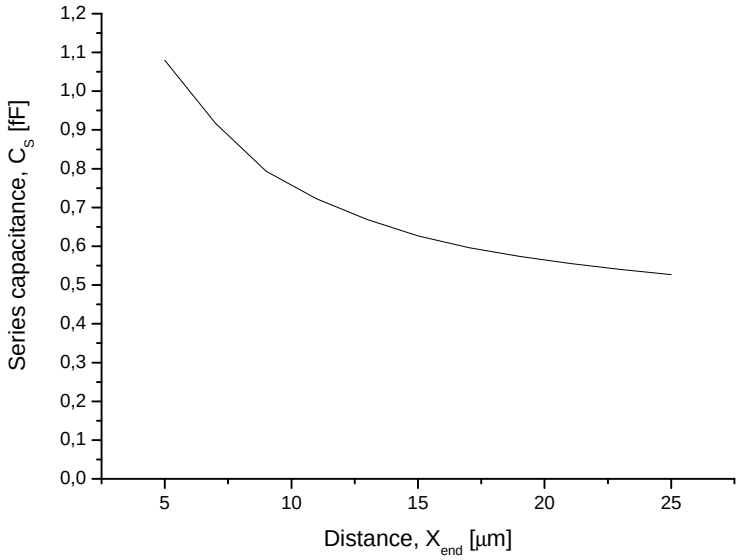

Figure 6.11: Series capacitance as function of the distance, X_{end} between the beam tip and main signal line.

6.3.3 Shunt coupling capacitance

A shunt coupling capacitance is created between the cantilever beam (signal line) and the two ground planes (Figure 6.2). As one of the ground planes is extended towards the cantilever beam, to function as the actuation electrode, the shunt coupling capacitance will be dominated by the capacitance in this region.

The coupling capacitance can be estimated using

$$C_g = C_{pp} + C_f = \frac{\varepsilon_0 wl}{g} + C_f \tag{6.4}$$

where C_{pp} is the parallel plate capacitance and C_f is the fringing capacitance. The fringing capacitance can be substantial compared to the parallel plate capacitance.

Using MemElectro, a number of electrode dimensions and gaps have been analyzed to map the fringing effect and is presented in table 6.1. The analysis shows that the fringing effect is reduced with a reduced gap and sufficiently wide/ long electrode, which is expected.

The shunt coupling capacitance will be higher in the down-state then up-

$l_2[\mu m]$	$w[\mu m]$	$g[\mu m]$	$C_U[fF]$	$C_{pp}[fF]$	$C_f[fF]$	$C_f/C_{pp}[\%]$
50	35	4	6.0	3.9	2.1	54
150	35	4	15.9	11.6	4.3	37
50	35	2	10.2	7.7	2.5	32
150	35	2	28.4	23.2	5.1	22
50	20	4	3.9	2.2	1.6	74
50	50	4	8.0	5.5	2.5	45
50	20	2	6.4	4.4	1.9	43
50	50	2	14.0	11.1	3.0	27

Table 6.1: Capacitance between two electrodes.

state, due to the reduced gap between the electrodes. In the down-state the electrode section of the cantilever will be at an angle, which complicates the calculation of the capacitance. However, the capacitance can be estimated using eq. (6.4) and an average gap, g.

As indicated in figure 6.9, the lower electrode and the lower contact will be in close proximity. When the switch is in the down state this can contribute to additional shunt coupling capacitance.

6.3.4 Inductance

Given the characteristic impedance of the cantilever, Z_l, the series inductance of the cantilever can be calculated using [11]

$$L = \frac{Z_h l \sqrt{\varepsilon_{eff}}}{c} \tag{6.5}$$

where ε_{eff} is the dielectric constant of a single effective material surrounding the conductor and c is the speed of light in vacuum ($c = 3.0 \cdot 10^8 m/s$). In literature Z_l and ε_{eff} are calculated using numerical electromagnetic techniques (i.e. HFSS [7]) [11, 37].

As such software was not available, an attempt was made to estimate the parameters Z_l and ε_{eff} using analytical methods for a conventional CPW [3]

$$Z_0 = \frac{30\pi}{\sqrt{\varepsilon_{eff}}} K \tag{6.6}$$

where K is dependent on the lateral geometry of the CPW t-line (Figure 6.1). For the CPW structure implemented here, the results were not comparable

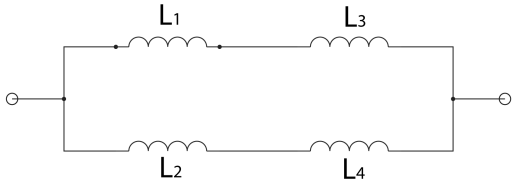

Figure 6.12: Total beam inductance.

with the values calculated using numerical electromagnetic techniques [11]. This is assumed to be due limitations in eq. (6.6). For a conventional CPW the thickness of the t-line is small compared with the lateral dimensions, w and s (Figure 6.1). For CPW used in this design however, the t-line thickness is the depth of the DRIE etch (thickness of the device layer), w, and is comparable to or larger than the lateral dimensions.

As an alternative method, using the inductance expression for parallel plate t-line was investigated. The inductance of a parallel plate t-line is given as [30]

$$L = \frac{\mu l W}{w} \qquad \text{for } g < w \tag{6.7}$$

where l is the length of the beam section and W is the distance between the two parallel plates. For the switch concept shown in figure 6.2 the total beam inductance can be represented as the network given in figure 6.12. The total beam inductance becomes

$$L = \left(\frac{1}{L_1 + L_3} + \frac{1}{L_2 + L_4} \right)^{-1} \tag{6.8}$$

where L_4 is the inductance of the electrode section of the beam. For the switch shown in figure 6.2 the remaining inductances are equal.

Using this method a beam inductance of $\sim 100\ pH$ was calculated for the geometry given in [11]. This is somewhat lower than the values presented in the article. However, the geometry has variations in cross-section which will result in parasitic inductance [3, 37]. Such parasitic effects will not be captured by this simplified method. The method has however sufficient accuracy to be used as a good estimate.

Figure 6.13 shows two beam sections with varying cross-sections. The tapered step is preferred as it will introduce less parasitic inductance. Similar changes in the dimension of the input or output t-line will also introduce

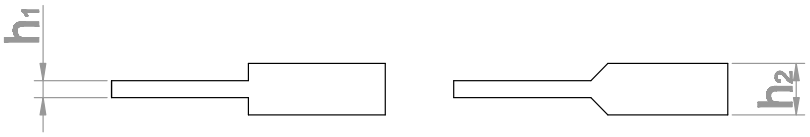

Figure 6.13: Cross-section variation of the cantilever beam.

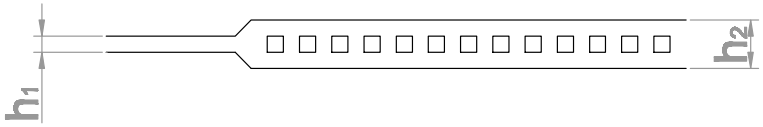

Figure 6.14: Cantilever beam with reduced mass.

parasitic inductance and should be included in the total switch inductance.

Holes can also be introduced in the section with the larger height, to allow for the cantilever beam section to be released (Section 3.3) and/or to reduce the mass of the section. Since the current is carried on the edges of the MEMS beam (Figure 6.7), the effect on the inductance is minimal [37].

MemHenry was also used to calculate the inductance. The results for a beam segment with varying width, are presented in table 6.2. The values were seen to remain roughly constant over the entire simulated frequency range (100 Mhz-30GHz) and were also largely independent of the thickness of the cladding layer.

Due to several limitations in MemHenry the accuracy is assumed to be somewhat reduced (Section 6.2.2). For the geometry given in [11], the calculated value using MemHenry was ~ 30 % higher than the value given in the article.

Beam width, w [μm]	Inductance, L [$pH/\mu m$]
20	0.53
35	0.44
50	0.39
65	0.34

Table 6.2: Calculated distributed inductance. ($t_m = 0.6$ μm)

Figure 6.15: Two-port S-parameter network. (From [30])

6.3.5 Contact resistance

A method to estimate the contact resistance, R_c, is given in chapter 4. Practical contact resistance values are around $0.5 - 2\ \Omega$ [37], but lower values have been presented.

6.4 S-Parameters

Network parameters such as impedance, admittance and ABCD-parameters are used to simplify and restructure complicated systems and are therefore valuable tools for characterization of circuits and devices. At high frequencies (f>500 MHz) however, scattering parameters (S-Parameters) must be used as the termination conditions used for characterization at lower frequencies become invalid. In addition, if proper terminations are not applied, voltage and current wave reflections will occur due to the wave propagation of the signal.

S-parameters define the input and output relations of a network using incident and reflected normalized power waves. These power waves are given as [30]

$$a_n = \frac{1}{2\sqrt{Z_0}}(V_n + Z_0 I_n) \tag{6.9}$$

$$b_n = \frac{1}{2\sqrt{Z_0}}(V_n - Z_0 I_n) \tag{6.10}$$

where Z_0 is the characteristic impedance of the terminations, and V_n and I_n are respectively the voltage and current wave at port n. A two port S-parameter network is shown in figure 6.15.

The S-parameters define the relation between the reflected power waves, b_n, and the incident power waves, a_n [30].

$$\begin{Bmatrix} b_1 \\ b_2 \end{Bmatrix} = \begin{bmatrix} S_{11} & S_{12} \\ S_{21} & S_{22} \end{bmatrix} \begin{Bmatrix} a_1 \\ a_2 \end{Bmatrix} \tag{6.11}$$

where the terms are

$$S_{11} = \frac{b_1}{a_1}|_{a_2=0} = \frac{\text{reflected power wave at port 1}}{\text{incident power wave at port 1}} \tag{6.12}$$

$$S_{21} = \frac{b_2}{a_1}|_{a_2=0} = \frac{\text{transmitted power wave at port 2}}{\text{incident power wave at port 1}} \tag{6.13}$$

The condition $a_2 = 0$ (and $a_1 = 0$) can only be achieved when the connecting transmission lines are terminated into their characteristic impedance, Z_0.

Expressions for the terms S_{11} and S_{21} for the equivalent circuit, given in figure 6.5, can be determined using network parameters. Based on the ABCD parameters for a T-network and conversion expressions [30] the terms, S_{11} and S_{21} become

$$S_{11} = \frac{\frac{Z_A+Z_B}{Z_0} + \frac{1}{Z_C}(Z_A - Z_0 - Z_B + \frac{Z_A Z_B}{Z_0})}{\Psi} \tag{6.14}$$

$$S_{21} = \frac{2}{\Psi} \tag{6.15}$$

where

$$\Psi = 2 + \frac{Z_A + Z_B + Z_0}{Z_C} + \frac{1}{Z_0}\left(Z_A + Z_B + \frac{Z_A Z_B}{Z_C}\right) \tag{6.16}$$

the T-network impedances become

$$Z_A = R_l + j\omega L \tag{6.17}$$

$$Z_B = \begin{array}{ll} \frac{1}{j\omega C_s} & \text{Up state} \\ R_c & \text{Down state} \end{array} . \tag{6.18}$$

$$Z_C = \frac{1}{j\omega C_g} \tag{6.19}$$

where ω is the angular frequency ($\omega = 2\pi f$).

6.4.1 Return loss

The return loss is given by S_{11} and is equal to the input reflection coefficient, Γ_{in}, which is a measure of the how much of the incident power wave is reflected at port 1. The return loss can be calculated by taking the logarithm of the magnitude of S_{11}.

$$RL = S_{11}[dB] = -20log|S_{11}| \tag{6.20}$$

Parameter	Symbol	Value
Beam series resistance	R_l	1 Ω
Series capacitance	C_s	4 fF
Shunt coupling capacitance	C_g	30 fF
Inductance	L	100 pH
Contact resistance	R_c	1 Ω

Table 6.3: The values of the equivalent circuit components used in this chapter. Any variations from this are commented in the respective calculations.

As a result, a device poorly matched to its connecting transmission lines will have a return loss, $S_{11} \rightarrow 0\ dB$. Figure 6.16 shows the calculated return loss for the device given in table 6.3.

The relatively complex expression given in eq. (6.14) can be greatly simplified for certain conditions, as several parameters (impedances) become dominant. In the down state, for low frequencies, $f < 3\ GHz$, $-34\ dB < S_{11} < -40\ dB$ and $R_s = 1 - 2\ \Omega$ the term S_{11} can be approximated as [37]

$$|S_{11}| \approx \left| \frac{R_s}{2Z_0} \right|^2 \qquad \text{for } \omega L \ll R_s \tag{6.21}$$

where R_s is the total series resistance of the switch, $R_s = R_l + R_c$. For high frequencies, $f \rightarrow 50\ GHz$ the term can be simplified as

$$|S_{11}| \approx \left| \frac{\omega L}{2Z_0} \right|^2 \qquad \text{for } \omega L \gg R_s \tag{6.22}$$

Using these equation, the required value for R_s and L to achieve a certain return loss, can be estimated. If measurements of S_{11} have been performed, the measured values can be used to calculate the parameters values for a specific device. However, it should be kept in mind that values calculated using this approach will include the resistance and inductance of the input and output t-line of the switch also.

6.4.2 Isolation

If the switch is in the up-state, the term S_{21} is the isolation of the switch. It is a measure of the amount of the incident power wave that leaks through the switch, and is also given in dB. RF MEMS switches have generally high

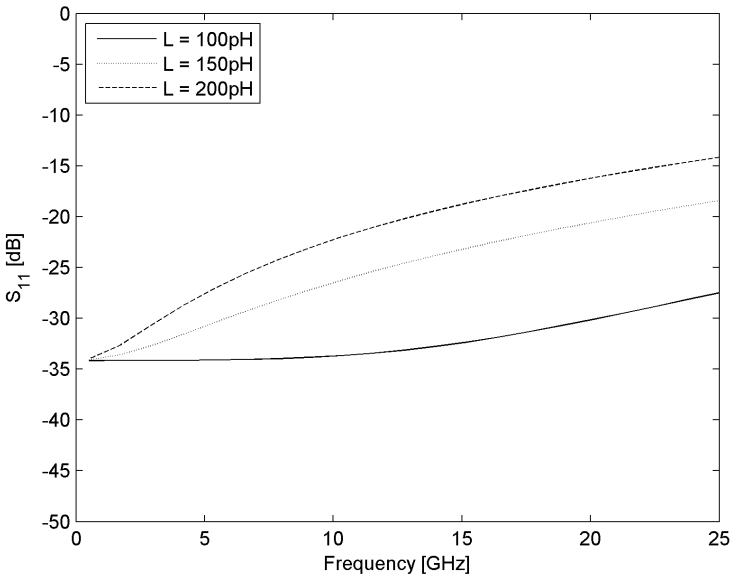

Figure 6.16: Calculated down state return loss, S_{11}, for three inductance values.

isolation, $S_{21} < -20\ dB$. Figure 6.17 shows the calculated isolation using eq. (6.14) for the device given in table 6.3.

If the isolation, $S_{21} \ll 10\ dB$ and the term $2\omega C_s Z_0 \ll 1$, eq. (6.15) can be approximated as [11, 37]

$$S_{21} \approx 2\omega C_s Z_0 \tag{6.23}$$

Similarly to the equations given for the return loss, eq. (6.23) can either be used for design or determining the series capacitance for a specific device.

6.4.3 Insertion loss

In the down-state, when the switch is transmitting, the term S_{21} is the insertion loss of the switch. The insertion loss indicates how much the incident power wave is damped through the switch. Generally for RF MEMS switches $S_{21} > -0.5dB$, which is very low. Figure 6.18 shows the calculated insertion loss for several contact resistances.

For typical values for the total series resistance, $R_s = 1 - 3\ \Omega$, the insertion loss can be calculated as [11]

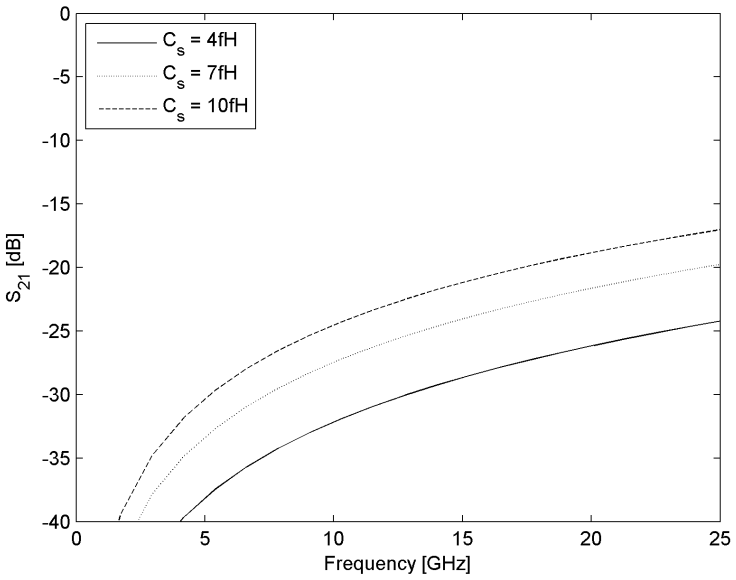

Figure 6.17: Calculated isolation, S_{S1}, for various series capacitances, C_s

$$S_{21} \approx \frac{2}{(2 + \frac{R_s}{Z_0})} \qquad \text{for } \omega L \ll Z_0 \tag{6.24}$$

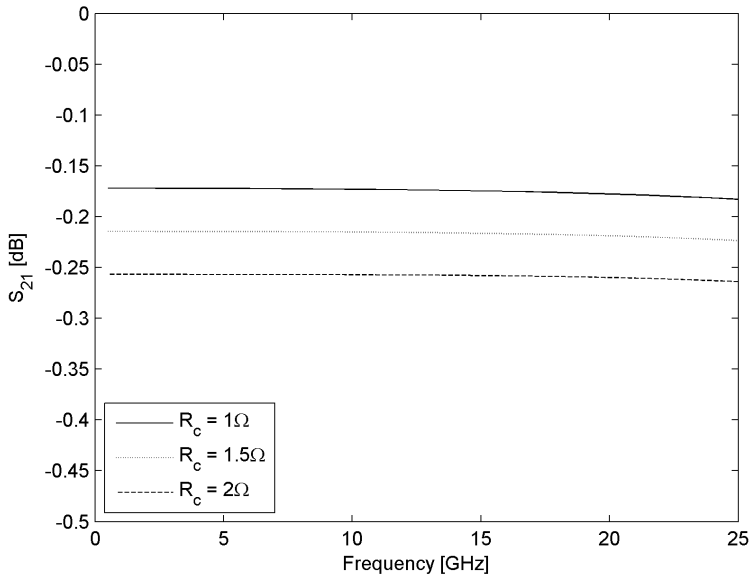

Figure 6.18: Calculated insertion loss, S_{21}, for various contact resistances, R_c.

Chapter 7

Design example

7.1 Introduction

The design of a RF MEMS switch is an iterative process due to the number of design characteristics in both the mechanical and RF domain. This chapter aims to give an overview of how some of these design characteristics influence each other. To do this, a switch will be designed to meet the requirements of a specific project.

The objective of the "Smart microsystems for diagnostics imaging in medicine" (SMIDA) project, is to develop an invasive diagnostic imaging system, that can detect the formation of blood clots that can cause i.e. infarction. In this project, RF MEMS switches will be used in a switching matrix to control an array of capacitive micromachined ultrasonic transducers (CMUT). The requirements for the switch is given in table 7.1.

The intention of this example is only to meet the performance requirements given in table 7.1. If the fabrication process, layout etc. is compatible with the intended project concept, has not been taken into account.

Parameter	Symbol	Value
Actuation time	t_a	$\sim 5\ \mu s$
Release time	t_r	$\sim 10\ \mu s$
Insertion loss	S_{21}	$< 1\ dB$
Isolation	S_{21}	$< 20\ dB$
Band width	BW	500 MHz-2 GHz
Power	P	Low

Table 7.1: Performance requirement for the SMIDA RF MEMS switch.

7.2 Calculations

For the given application, achieving the required switching time is the major challenge. The entry point to the design in this case is therefore the switching time. For another application, which for example requires a very high isolation, a natural entry point would be to look at the required up-state capacitance [Eq. (6.23)].

Based on eq. (5.50) the required resonance frequency of the cantilever beam becomes

$$f_0 \simeq 3.67 \frac{V_{pi}}{V_a 2\pi t_a} = 93 \; kHz \tag{7.1}$$

assuming an actuation voltage, $V_a = 1.25 \cdot V_{pi}$. An increased actuation voltage results in a lower required resonance frequency, but at the same time increases the release time of the switch ($t_r = 1/f_0$).

The resonance frequency of the structure is given by $\omega_0 = \sqrt{k/m_{eff}}$, where the equivalent spring constant, k, is given by eq. (5.18) and the effective mass, m_{eff}, by eq. (5.39). The required frequency can be achieved for a number of geometries, but the value of k should be chosen carefully as it is effects the pull-in voltage, contact force, restoring force etc. The pull in voltage, $V_{pi} \propto \sqrt{g_0^3}$ and is given by eq. (5.9).

Further, some design constraints must be applied based on limitations of the fabrication process described in section 3.3. The minimum width of a trench is assumed to be 2 μm for a beam width of 35 μm. This implies that the minimum achievable electrode gap, $g_0 = 2$ μm. Similarly, the minimum feature size dictates the minimum height of the cantilever beam, $h_1 = 2$ μm (Section 3.3.3).

Table 7.2 presents the geometry of two designs that both have approximately the required resonance frequency, f_0 (Figure 7.1). Figure 7.2 shows that both designs have the same pull-in voltage even though Design # 1 has a higher equivalent spring force compared to Design #2. This is due to, both the resonance frequency and the pull-in voltage are both proportional to $\sqrt{l_{tot}^{-1}}$.

Based on these initial calculations, the required switching time can basically be achieved by either of the designs. A number of characteristics may however be different for the two designs. The increased electrode length may i.e. result in increased damping (Section 5.3.8), which again effects the switching time. The increased beam length will also influence the RF characteristics.

From figure 7.2 it can be seen that by increasing the relative electrode

Parameter	Symbol	Design # 1	Design # 2
Total length	l_{tot}	150 μm	115 μm
Height AB	h_1	3 μm	2 μm
Height BD	h_2	6 μm	6 μm
Metal thickness	t_m	0.5 μm	0.5 μm
Inital gap	g_0	2 μm	2 μm
Contact gap	d	1.5 μm	1.5 μm
Width	w	35 μm	35 μm

Table 7.2: Geometry of two designs.

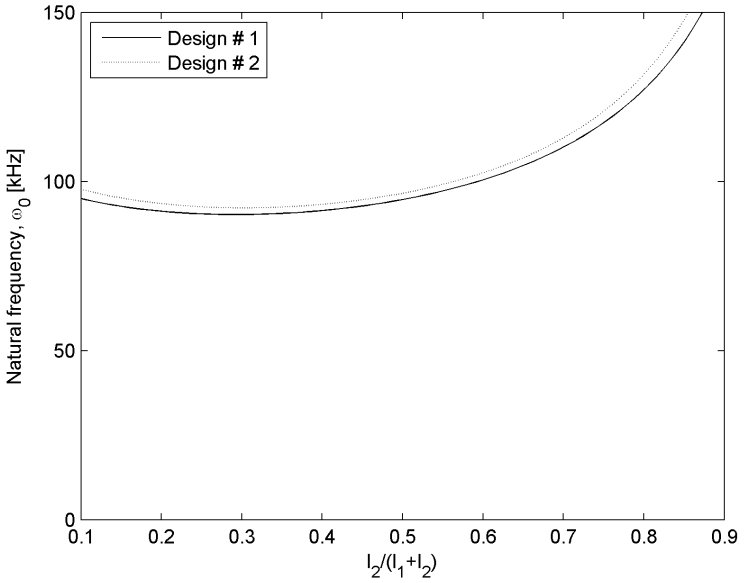

Figure 7.1: Resonance frequency for the two designs given in table 7.2.

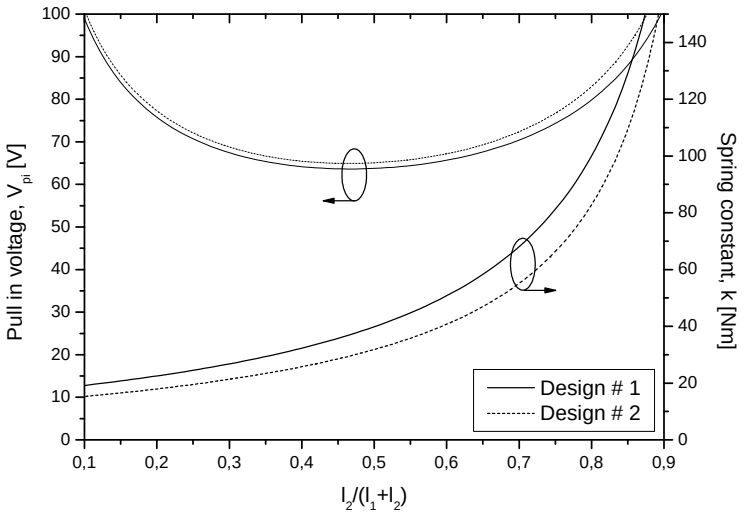

Figure 7.2: Pull-in voltage and equivalent spring force for the two designs given in table 7.2.

length, $l_2/(l_1 + l_2)$, from 0.5 to 0.6 the spring constant can be increased by $\sim 20\%$. At the same time the pull-in voltage remains approximately constant. As the restoring force [Eq. (5.28)] of the cantilever is a linear function of the equivalent spring force, this can be important for the reliability of the switch.

An increased beam stiffness will basically reduce the contact force for a given actuation voltage. However, when the increased stiffness is accompanied by an increased actuation area, estimating the contact force becomes difficult. As these two designs are very stiff, the maximum achievable contact force, F_{cmax} (Section 5.3.6), occurs at a very high actuation voltage. Architect has therefore been used to calculate the contact force. Figure 7.3 shows the calculated contact force for the two designs for two different electrode lengths.

According eq. (5.35) the contact force can be increased by increasing the width of the beam. The conformal metal deposition process however limits this width, especially for narrow trenches.

The actuation time and release time is calculated using the method given in section 5.3.9 and presented in figure 7.4. The results for design # 2 are approximately the same. An effective width, $w_{eff} = 1.5 \cdot w$ is implemented to take into account the increased damping effect described in section 5.3.8. The bouncing that occurs after the switch makes contact will increase the actuation time. This is however disregarded in this design example.

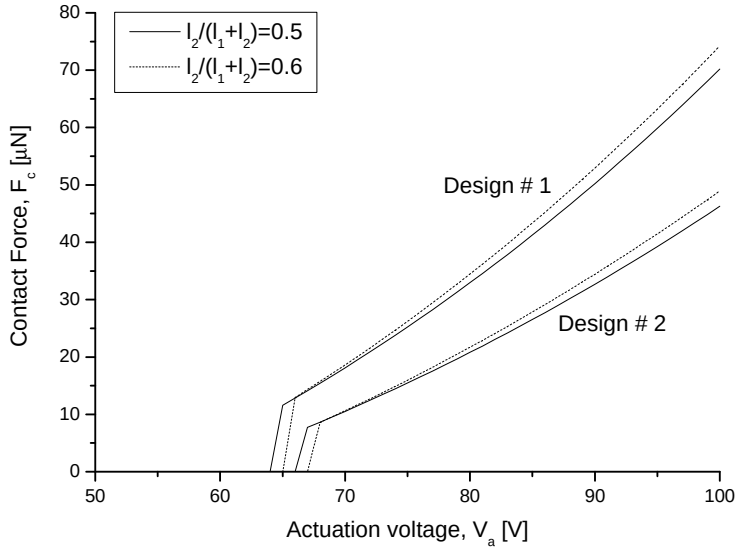

Figure 7.3: Contact forces for two different electrode lengths, l_2.

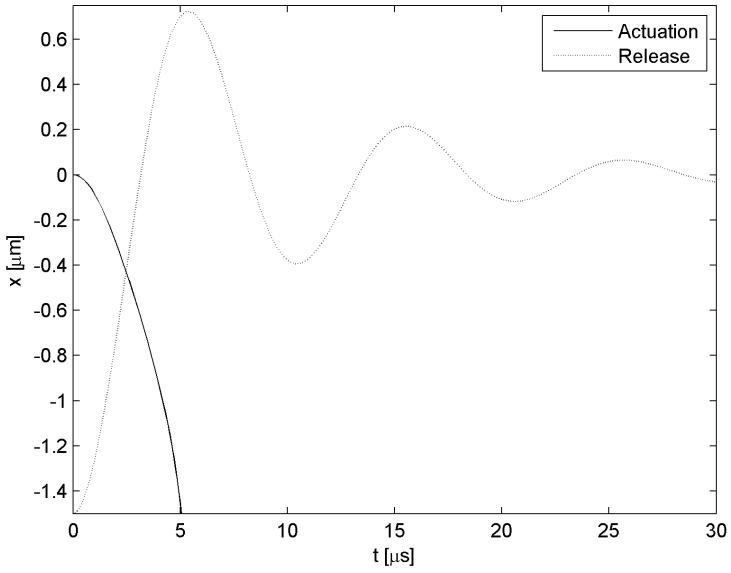

Figure 7.4: Calculated actuation and release time.

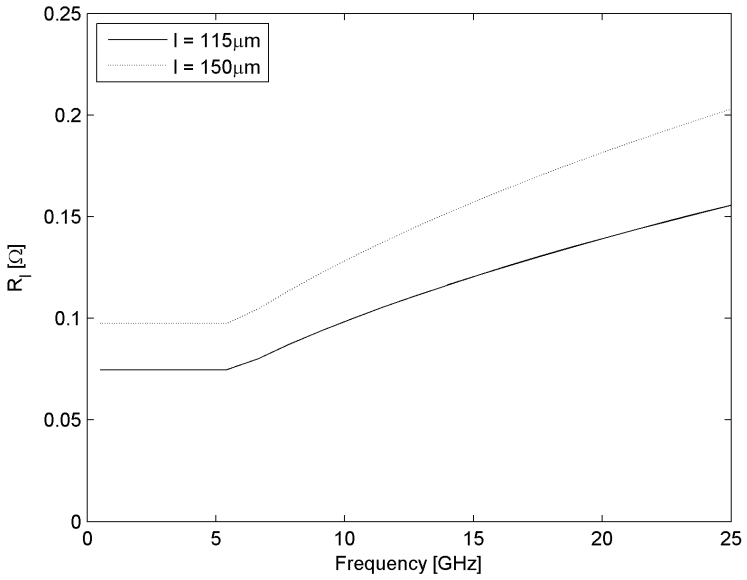

Figure 7.5: Beam series resistance for the two beam designs.

State	Design # 1	Design # 2
Beam series resistance	$R_l \approx 0.2\ \Omega$	$R_l \approx 0.15\ \Omega$
Series capacitance	$C_s \approx 4\ fF$	$C_s \approx 4\ fF$
Up-state capacitance	$C_g = 15 - 17\ fF$	$C_g = 12 - 14\ fF$
Down-state capacitance	$C_g = 28 - 33\ fF$	$C_g = 22 - 26\ fF$
Inductance	$L \approx 40\ pH$	$L \approx 30\ pH$
Contact resitance	$R_c = 0.5 - 2\ \Omega$	$R_c = 0.5 - 2\ \Omega$

Table 7.3: Estimated values for the equivalent circuit parameters.

Figure 7.5 shows the calculated resistance [Eq. (6.3)] for the two designs. The shunt coupling capacitance in the up and down-state are estimated using the parallel plate approximation and the fringing factors given in table 6.1. In the down-state the upper electrode will be at an angle and an average gap, $g \approx 1\mu m$ is used. The up-state series capacitance is estimated based the results presented in section 6.3.2.

By assuming a distance, $W = 20\ \mu m$ between the beam and the ground planes (Figure 6.2), the inductance is calculated using eq. (6.7) and (6.8). The calculated inductance and the other calculate equivalent circuit parameters are given in table 7.3.

The switch Isolation is simulated using eq. (6.15) and is presented in figure 7.6. The simulated isolation for two larger capacitance values is also

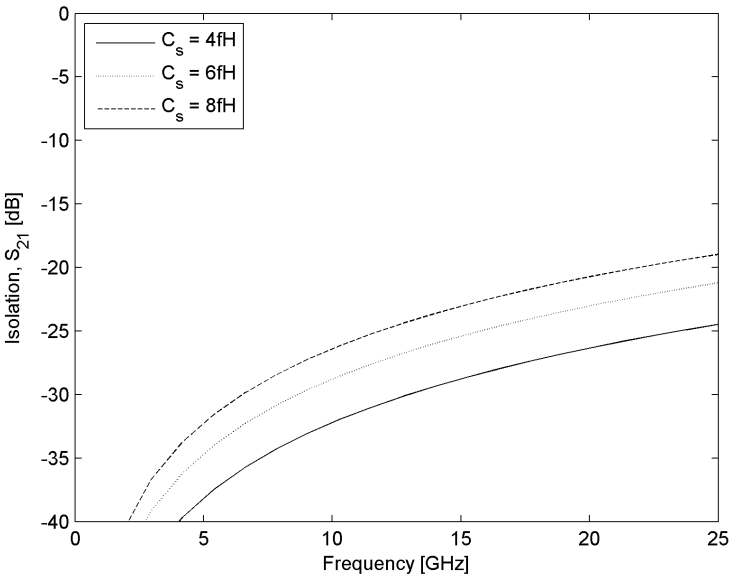

Figure 7.6: Calculated isolation for design #1 for three series capacitance values.

shown. The insertion loss is calculated using the same equation but with parameter values representing the down state. As the insertion loss is largely effected by the total series resistance ($R_l + R_c$), the simulated insertion loss is presented in figure 7.7 with three different contact resistance values.

Figure 7.8 shows the simulated return loss [Eq. (6.14)]. Due to the uncertainty related to the inductance, the return loss has been simulated for several inductance values.

The RF characteristics for both designs are fairly similar. As a result, both designs meet the requirements given in table 7.1. However, design # 2 is regarded as better due to the increased contact force and restoring force achieved. By implementing a relative electrode length, $l_2/(l_1 + l_2) = 0.6$, the restoring force of the switch is further improved.

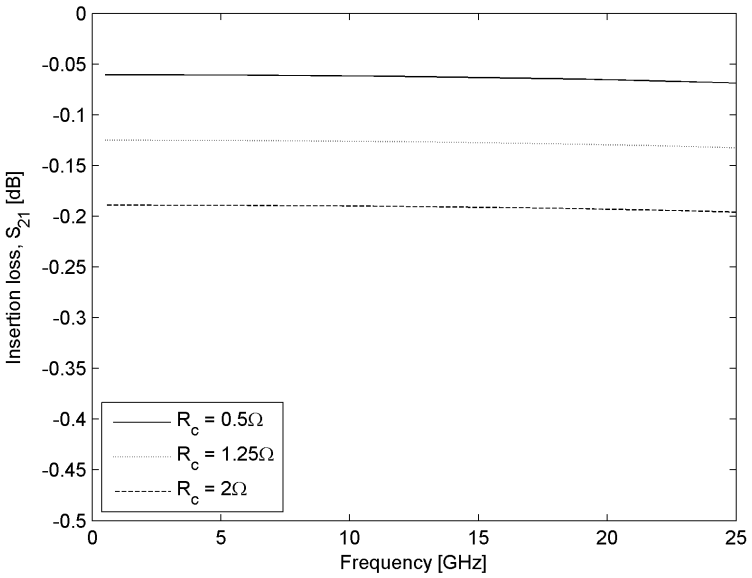

Figure 7.7: Calculated insertion loss for for design #1 for three contact resistance values.

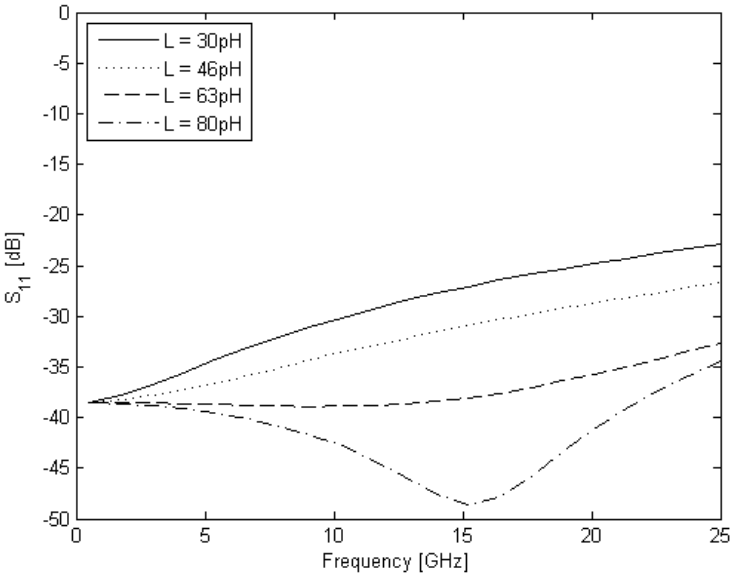

Figure 7.8: Calculated return loss for design #1 for a range of inductance values.

Chapter 8

Comparison of two switch concepts

8.1 Introduction

The intention of this chapter is point out some key differences between the DRIE based switch concept discussed in this thesis and the more traditional switch fabricated using layered surface micromachining. Based on this, some of the advantages and disadvantages of the two concepts will be discussed.

8.2 Fabrication

One of the drawbacks of a layered surface micromachined switch is the number of process steps required. A basic design requires four lithography steps (Section 3.4). In comparison, the DRIE based fabrication process only requires one lithography step in addition to a shadow mask.

The accuracy of the lithography process used for the SOI process must be much higher than what is acceptable for layered surface micromachining. This is due to the DRIE fabricated devices being actuated laterally and a small variation in the height of the cantilever beam will drastically change the structural stiffness. For the same reason, the DRIE process must be well controlled to achieve perfectly vertical sidewalls with minimal lateral etch. As a result of these factors, the minimal feature size for the SOI process is assumed to be 2 μm [31].

Using layered surface micromachining, the thickness of the deposited layers can vary from $< 1\mu m$ to $> 5\mu m$ and is well controlled within $\pm 1 - 2$ % of the thickness. The initial gap, g_0 (Figure 5.8), can therefore be very small and well controlled. For the DRIE based switch concept the initial gap is lim-

ited by the metal deposition process, which requires a certain trench width to achieve metal deposition on the vertical sidewalls. For the same reason the width of the beam is also limited.

For structures fabricated using deposited layers, residual stress is often a problem, which causes warpage and distorted structures. The residual stress is typically caused by difference in thermal coefficient of expansion (extrinsic stress) for the different layers, or non-equilibrium atomic arrangements (intrinsic stress) in the deposited films [5]. For DRIE etched structures this is not a problem as long as the conformal metal is deposited with equal thickness on both sides of the Silicon structure. The intrinsic stress in the Silicon layer is minimal but warping may occur for long slender structures [31].

To remove the sacrificial layer underneath wide structures, a wet etch process is typically required. As a result, special release methods may need to be implemented to avoid problems with stiction (3.4). For the DRIE based switch concept the need for special release methods can be avoided, as only a limited underetch is required and a dry etch can therefore be used.

As described in section 3.3.3, the definition of a contact can be difficult using DRIE. The deposition of a contact material can also be challenging. It is possible to deposit the contact material on the entire switch but this increases the series beam resistance, as the contact materials have generally a higher resistivity than i.e. Au. Therefore it is less complicated to fabricate a contact using a patterned deposited sacrificial layer and deposited contact material (Figure 3.8)

A number of switches have been demonstrated in literature that are fabricated using CMOS compatible surface micromachined process. The process steps required to fabricate the switch concept discussed in this thesis are post-CMOS compatible, but the practical aspects have not been analyzed.

8.3 Mechanical properties

Identifying the advantages and disadvantages related to the mechanics of the two concepts is difficult, as they are very dependent of the specific design. However, some general aspects will be discussed here.

The Young's modulus of Silicon is higher than that of metals with low resistivity. As a result, the effective Young's modulus (Section 5.3.3) of a layered beam (Figure 5.9) is higher then the Young's modulus of applicable metals. An example of a cross-section is given in table 8.1. Based on this the equivalent spring constant, $k_{layered} \approx 2 \times k_{Au}$ [Eq. (5.12)]. The restoring force is increased equally. At the same time, the pull-in voltage is only increase by $\sqrt{2}$ [Eq. (5.9)]. This can be an advantage, as it is desirable that the restoring

Parameter	Symbol	Value
Silicon core height	h	3 μm
Metal cladding layer thickness	t_m	0.5 μm
Effective Young's modulus beam	E	$104GPa$
Effective Density of beam	ρ	$6700kg/m^3$
Young's modulus beam core	E_{Si}	$169GPa$
Density of beam core	ρ_{Si}	$2500kg/m^3$
Young's modulus cladding layer	E_{Au}	$58GPa$
Density of cladding layer	ρ_{Au}	$19300kg/m^3$

Table 8.1: Cross-section used as an example to demonstrate advantages of using a layered cross-section

force is large to overcome any adhesive forces at the contact.

The increased stiffness and reduced mass will also result in a higher resonance frequency ($\omega_0 = \sqrt{k/m_{eff}}$). For the cross-section given in table 8.1, the natural frequency, ω_0, can be increase by a factor $\sim \sqrt{6}$ compared to a Au beam with the same cross-section. Assuming that the beam is not subjected to large damping forces, the switching time is then reduced by the same factor [Eq. (5.50)]

These positive effects assume the same geometry for both the layered beam and the Au beam. However, using layered surface micromachining the width of the beam can be varied, as opposed to the DRIE based process where the width is constant and limited. By implementing a design with a wider actuation area, a fairly stiff beam can be actuated with a relatively low actuation voltage. In order to achieve a large actuation area for the switch fabricated using the DRIE based process, the length of the beam must be increased. This increase in length reduces the effective spring constant, $k \propto l^3$, which effectively reduces the restoring force and the resonance frequency of the beam.

An effective method to reduce the actuation voltage is to reduce the initial gap, g_0, between the upper and lower electrode ($V_{pi} \propto \sqrt{g_0^3}$). As mentioned above, the minimum possible initial gap for the DRIE based switch concept is limited by the fabrication process.

The size of the actuation area and the initial gap is also very important parameters for contact force, as

$$F_{con} \propto \frac{\varepsilon_0 A_a V_a^2}{2g^2} \tag{8.1}$$

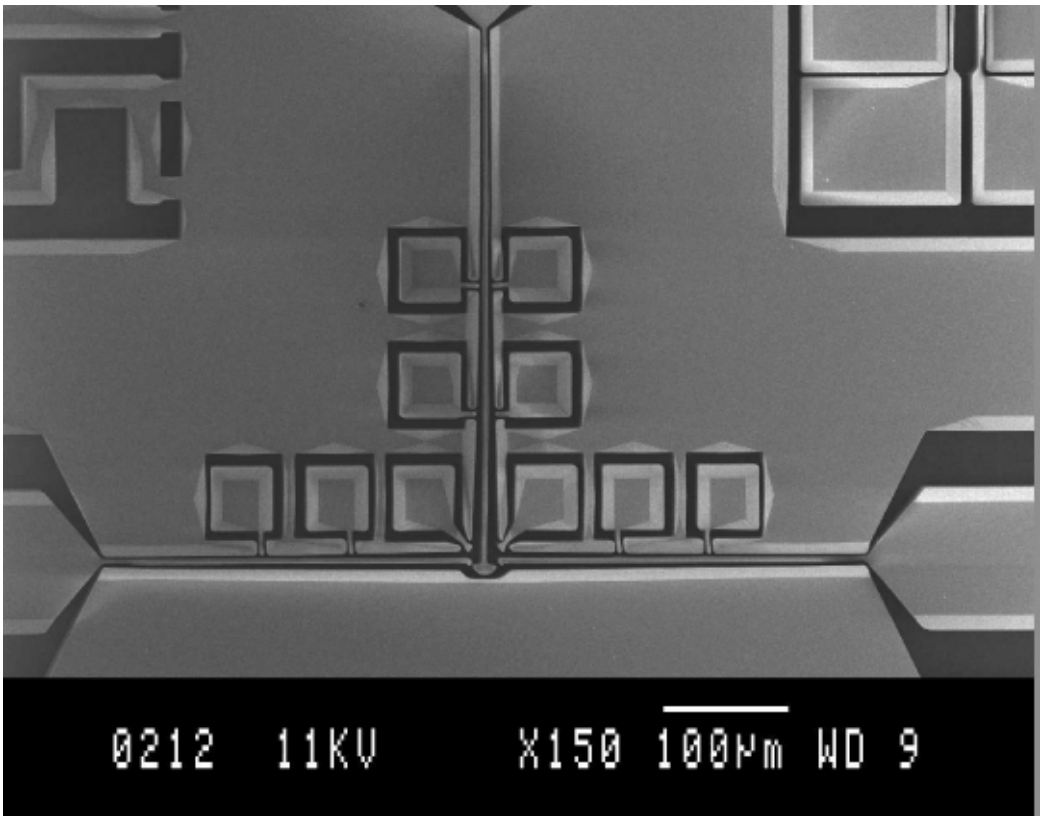

Figure 8.1: SEM-picture of a tri-stable single pole double throw switch with three beams actuated using curved electrodes. (From [14])

The gap g is the electrode gap in the down-state, which can be estimated as an average gap of the angled beam electrode. The average gap, g, increases with the initial gap.

Using a DRIE based fabrication process, complicated structures with e.g. multiple actuation electrodes, actuations in different directions [14] and curved electrodes [17] can be fabricated using few process steps. The same is either not possible or practical, using layered surface machining techniques. Figure 8.1 shows a tri-stable single-pole-double-throw switch with three beams actuated using curved electrodes.

8.4 RF properties

As mentioned in chapter 6, coplanar t-lines are often preferred at higher frequencies, and can improve performance and design flexibility for some

circuit functions. As a result of the current distribution shown in figure 6.3, the DRIE fabricated switch concept is most suited to be implemented as one of the coplanar t-line configurations. A typical series switch fabricated using a layered surface micromachined process, is however more suited to be implemented as a microstrip configuration due to its width and thickness.

The upper operation frequency of series RF MEMS switches is typically limited by the up-state series capacitance (Figure 2.1). Therefore, to take full advantage of the improved high frequency characteristics of a coplanar switch structure, the series capacitance should limited. This can be achieved by increasing the gap between the upper and lower contact. A longer beam with a actuation electrode situated further from the anchor can have a larger contact gap without increasing i.e. the actuation voltage. DRIE switch concept result in increased beam stiffness and reduced residual stress, which means that longer beams can be implemented.

By using DRIE it is also possible to shape the cantilever tip surroundings to reduce the series capacitance (Figure 6.9). Using layered surface micromachining, the series capacitance is reduced by limiting the overlapping area.

Chapter 9

Conclusion

The objective of this thesis has been to model and analyze the characteristics of a laterally actuated series resistive contact RF MEMS switch, fabricated using only a few process steps.

The fabrication process, which is based on DRIE and the deposition of a conformal metal layer, introduces several important limitations on the design of the switch. In order to achieve low conductor loss a metal layer must be deposited on the vertical sidewalls of the defined structures. As a result of this deposition process, certain dimensional limitations must be placed on the switch design. The fabrication of a reliable contact is also assumed to be more challenging compared to a layered surface micromachining approach.

The importance of the contact on the reliability of a metal contact switch is discussed. A model to estimate contact area and resistance is presented, showing the importance of well characterized contact metals in addition to underlining the complexity of the contact physics.

To analyze the mechanical characteristics of the cantilever switching element, analytical methods have been implemented. Using these methods, the parameter dependency of the different design characteristics have be investigated. The analytical methods have also been supported and verified by using both system level and FEM simulations.

A direct comparison between the more traditional layered surface micromachined switch and the laterally actuated switch is difficult as the characteristics are very dependent of the specific designs. However, some general remarks can be made. The lateral switch concept results in a layered beam with increased stiffness and reduced mass compared to metal beam. The advantages this offers are however reduced due to the limited width of the beam and minimum electrode gap caused by the limitations of the fabrication process.

The lateral switch concept allows for the switch to be integrated in a

coplanar transmission line structure. Using a coplanar transmission line structure the characteristic impedance of the switch is well controlled. As a result, the high frequency properties of the lateral switch are assumed to be as good as or better than a series resistive contact switch fabricated using layered surface micromachining. The analysis of the RF characteristics of the lateral switch concept is somewhat limited as a full wave electromagnetic analysis tool was not available. However, using simplified analytical models analyses of variations of the different design parameters and their effect on the RF characteristics have been performed.

Based on the findings of this thesis it is the authors opinion that the lateral DRIE fabricated switch concept is best suited for an application where a high actuation voltage ($V_a \sim 100V$) is available. If a high actuation voltage is not available, a reliable switch with a high contact force and high restoring force can not be achieved.

Chapter 10

Future work

The lateral switch is based on a fabrication process which is immature. Especially the conformal metal deposition process must be further investigated in order to identify limitations, typical variations and their implications on the design. However more importantly, it must be determined if it is possible to fabricate a reliable contact using the fabrication process.

In order to successfully develop a metal contact RF MEMS switch the contact physics must be better understood. This is an active field of research and it is assumed that models to estimate e.g. adhesive forces, the effect of temperature and the number of cycles to failure will be available in the near future.

The increased damping effect identified in section 5.3.8 should be further analyzed. This effect is not only important for RF MEMS switches but also other applications that implement a lateral moving structure fabricated using DRIE.

As mentioned above the RF analysis performed is somewhat simplified. In order to validate the findings of this thesis a full wave electromagnetic analysis should be performed.

A topic which has not been discussed in this thesis is the packaging of the switch. The packaging of RF MEMS devices is very important and has proven to be very challenging due to requirements related to hermeticity, performance and cost requirements.

In this thesis a fairly simple geometry with only one beam and one actuation electrode has been studied. The fabrication process however, allows fabrication of complex geometries. By for example implementing a shear force to overcome adhesion forces at the contact, the restoring force could be reduced. This could again reduce the actuation voltage etc. How this effects the reliability of the contact is however uncertain.

Appendix A

MATLAB code

A.1 Contact modeling

This section includes the source code for the main functions used to model and plot the contact deformation and contact resistance.

```
function [DataTot]=ContactModeling(MatData,GK,Profile)
% Calculates the material deformation and contact resistance
%
% MatData   = material/ surface data
% GK        = Gamma function as a func of knudsen number
% Profile   = Asperity height distribution
close all

%Description of the dataset
V1='n=20 - std=10 nm';

% Calculate contact resistance
[DataTot{1},Rc_M{1},Rc_S{1},reff{1}]=CalcRc(MatData(1),GK,...
    Profile{2},2);

%Plot individual contact radius as a func of total contact force
myxlabel='Total contact force, F_c [N]';
myline={'-b','--b',':r','-.r'};
myxlim=[1E-8 1E-3];
myxlim1=[1 200];
myylim1=[1E-2 1E1];

[x,y,z1]=size(DataTot{1})
figure
for i=1:(z1-1)
    loglog(DataTot{1}(:,2,end),DataTot{1}(:,3,i),myline{1})
end
```

```
xlabel(myxlabel)
ylabel('Contact radius, r [m]')
xlim(myxlim)
legend(V1)

%Plot contact resistance as a func of total contact force
figure
loglog(DataTot{1}(:,2,end),Rc_M{1},myline{1})       %Multi
hold on
loglog(DataTot{1}(:,2,end),Rc_S{1},myline{2})       %Single
ylabel('Contact resistance [\Omega]');
xlabel(myxlabel);
xlim(myxlim)
legend(['Multi a-model'], ['Single a-model'])
hold off

%Plot contact resistance as a func of total contact force for
%uN range
figure
semilogy(Si2u(DataTot{1}(:,2,end)),Rc_M{1},myline{1})   %Multi
hold on
semilogy(Si2u(DataTot{1}(:,2,end)),Rc_S{1},myline{2})   %Single
ylabel('Contact resistance [\Omega]');
xlabel(myxlabel);
xlim(myxlim1)
ylim(myylim1)
legend(['Multi a-model'], ['Single a-model'])
hold off
```

```
function [DataTot]=CalcRc(MatData,GK,Profile,Method)
% Calculates the upper (single) and lower (multi) contact
% resitance envelope curves based on material/ surface properties
% and gamma function determining electron transport regime.
%
% MatData   = material/ surface data
% GK        = Gamma function as a func of knudsen number
% Profile   = Asperity height distribution
% Method    = Determines which material deformation model is used

%Manipulate input data
[mat]=ConvMat2Si(MatData);
z=Profile;
z=z+1000;

%Calculate asperity contact details
d0=max(z);
dec=5;        %number of decades the deflection varies over
```

```
res=100;      %resolution/ number of data points per decade
y0=1.5;       %start for i.e. 2=nmE-2

for i=1:length(z)
    for x=1:dec*res
        y=-y0+x/res;
        d=d0-10^y;
        a(x)=z(i)-d;       %Deflection for each asperity
        if a(x)<=0
            a(x)=NaN;
        end
    end
    if Method==1            %Mat. deformation model used
        [data(:,1,i),data(:,2,i),data(:,3,i),ac]=...
            ElasticPlasticV1(mat,n2Si(a));     %[A,Fc,r]
    elseif Method==2
        [data(:,1,i),data(:,2,i),data(:,3,i),ac]=...
            ElasticPlasticV2(mat,n2Si(a));     %[A,Fc,r]
    elseif Method==3
        [data(:,1,i),data(:,2,i),data(:,3,i)]=...
            Elastic(mat,n2Si(a));     %[A,Fc,r]
    elseif Method==4
        [data(:,1,i),data(:,2,i),data(:,3,i)]=...
            Plastic(mat,n2Si(a));     %[A,Fc,r]
    else
        error('Method must be either "1, 2, 3 or 4"');
    end
    data(:,4,i)=n2Si(a);    %Convert to Si
end

%Total area,contact force and radius
data0=data;
data0(isnan(data))=0;                   %Replace NaN's
DataTot=data0;
DataTot(:,:,length(z)+1)=sum(data0,3);  %Sum the contribution
                                        %from the different a's
%Calculation of contact resistance based on material deformation
[Rc_M,RcD_M,RcB_M,K_M,G_M] = CalcRcMulti(mat,GK,DataTot);
[Rc_S,RcD_S,RcB_S,K_S,G_S,reff] = CalcRcSingle(mat,GK,DataTot);

clear data0 data;
```

```
function [A,Fc,r,ac]=ElasticPlasticV2(mat,a)
% Calculate elastic and plastic material deformation based on
% method described in "Micro-Switches with Sputtered Au, AuPd...
% Electric Contact" R.A. Coutu Jr and "An elastic-plastic contact
% model ..." W.R.Chang
```

```
%Assign parameters
R=mat.R;        %Asperity peak radius
E1=mat.E1;      %Elastic modulus of contact material 1
v1=mat.v1;      %Poisson ratio of contact material 1
E2=mat.E2;
v2=mat.v2;
H=mat.H;        %Meyer hardness of the softer material

Em=((1-v1^2)/E1+(1-v2^2)/E2)^-1;    %Hertzian modulus
K=1.282+1.258*v2;                   %Yield coefficient
Y=0.354*H;                          %Yield strength
ac=R*(pi*K*Y/(2*Em))^2;             %A's critical deformation
flag=0;

for row=1:length(a)
    if a(row)>ac                    %Elastic-plastic
        %Contact area
        A(row)=pi*R*a(row)*(2-ac/a(row));     %(16)

        %Contact radius
        r(row)=(A(row)/pi)^(1/2);

        %Contact force
        Fc(row)=(3+((2/3)*K-3)*(ac/a(row)))*A(row)*Y;      %(18)
%         if flag==0
%             r(row)=NaN;           %Insert a NaN value at the
%             flag=1;               %elastic-plastic transition
%         end
     elseif a(row)~=0               %Elastic
        %Asperity contact area
        A(row)=pi*R*a(row);

        %Contact force
        Fc(row)=4/3*Em*a(row)*sqrt(R*a(row));

        %Contact radius for circular contacts as a func of Fc
        r(row)=(3*Fc(row)*R/(4*Em)).^(1/3);
    end
end
```

```
function [Rc,RcD,RcB,K,G] = CalcRcMulti(mat,GK,data)
% Calculates the contact resistance assuming a multiple asperity
% model.
%
%   mat     = Material data
%   GK      = Function defining e transport regime
```

```
%   data    = Asperity deformation data

%Assign parameters
le=mat.le;      %Mean free path of electrodes
rho=mat.rho;    %Resistivity of contact material

%Calculate R for the individual asperities
[x,y,z]=size(data);
for i=1:(z-1)
    ra=data(:,3,i);    %radius of the individual aspereties
    ra(find(ra==0))=NaN;    %Replace 0's to allow division

    %Knutsen number
    K(:,i)=le./ra;

    %Ballistic e transport
    RcB(:,i)=4*rho*K(:,i)./(3*pi*ra);

    %Diffusive e transport
    RcD(:,i)=rho./(2*ra);

    %Determine e transport regime
    [G(:,i)]=GammaInterp(GK,K(:,i));

    %Wexler resistance for elastic plastic material deformation
    RcB(isnan(RcB))=0;      %Replace NaNs with zeros
    RcD(isnan(RcD))=0;
    G(isnan(G))=0;
    Rci(:,i)=RcB(:,i)+G(:,i).*RcD(:,i);
end

%Calculate total Rc for paralell connection of the Ra
[x,y]=size(Rci);
for row=1:x
    Rc(row,1)=sum(1./Rci(row,(find(Rci(row,:)~=0))))^-1;
end
```

A.2 S-Parameter modeling

The main functions used to perform the S-parameter calculations are given in this section. Vectorization has been used to make the MATLAB code faster and easier to read.

The functions used to model the beam mechanics implements much of the same principles and are therefore not included in this Appendix.

```
function [circuit]=SetupEqCircuit
% The controlling function for calculation of S-parameters of the
% equivalent circuit

close all

%Parameteres
circuit.Rc=1;               % Contact resistance
circuit.Rl=0.2;             % Series resistance
circuit.Cgup=f2Si(15);      % Shunt coupling capacitance up
circuit.Cgdown=f2Si(30);    % Shunt coupling capacitance down
circuit.Cs=f2Si(4);         % Series capacitance
circuit.L=p2Si(50);         % Inductance

circuit.Z0=50;              % Characteristic impedance

circuit.e0=8.854E-12;       % Permitivity
circuit.mu0=4*pi*1E-7;      % Permability
circuit.sigma=4.4E7;        % Conductivity [S/m]
circuit.tm=u2Si(0.5);       % Thickness of cladding
circuit.w=u2Si(35);         % Width
circuit.cw=2;               % Width correction factor (Rl)
circuit.l=u2Si(400);        % Length

circuit.flow=G2Si(0.5);     % Lower frequency
circuit.fhigh=G2Si(25);     % Upper frequency

set(0,'DefaultAxesColorOrder',[0 0 0],...
      'DefaultAxesLineStyleOrder','-|:|--|-.')

%Setup of parameter to vary
y.name='L';                 % Name of parameter to be varied
%y.low=(0.5);
%y.high=(2);
y.low=p2Si(30);
y.high=p2Si(80);
y.res=3;                    % Resolution
y.vary=1;                   % 0=No variation; 1=Vary

%Define meshgrid
xres=20;                                % Datapoints per decade
x=circuit.flow:(circuit.fhigh-circuit.flow)/xres:circuit.fhigh;
xname='f';                              % x variable name

yname=y.name;
if y.vary==1                % A parameter is set to vary
    y=y.low:(y.high-y.low)/y.res:y.high   % Y vector
```

```
    [X,Y]=meshgrid(x,y);

    %Initiate the defined variables with meshgrid matrices
    eval(['circuit.',xname,'=X;']);
    eval(['circuit.',yname,'=Y;']);

    %Find which parameters has been defined to be variable
    names=fieldnames(circuit);
    for i=1:length(names)
        yfound(i)=strcmp(names{i},yname);
    end

    if isempty(find(yfound))
        error('Variable not valid. Valid names:');
        names
    end

    %Define data legend
    switch yname
        case 'L'
            leg='L';
            factor=Si2p(1);
            unit='pH';
        case 'Cgdown'
            leg='C_g';
            factor=Si2f(1);
            unit='fH';
        case 'Cgup'
            leg='C_g';
            factor=Si2f(1);
            unit='fH';
        case 'Cs'
            leg='C_s';
            factor=Si2f(1);
            unit='fH';
        case 'Rc'
            leg='R_c';
            factor=1;
            unit='\Omega';
        case 'Rl'
            leg='R_l';
            factor=1;
            unit='\Omega';
        case 'l'
            leg='l';
            factor=Si2u(1);
            unit='\mum';
        otherwise
            leg='x';
```

```
            factor=1;
            unit='';
    end

    %Define legend
    for i=1:length(y)
        Mylegend{i}=[leg, ' = ',num2str(y(i)*factor), unit];
    end

elseif y.vary==0       % Calculate only for the given set of data
    %Initiate the defined variable with vector
    [X,Y]=meshgrid(x,1);
    eval(['circuit.',xname,'=X;']);
    Mylegend={};
end

%Calculate parameters
[circuit.ZA,circuit.ZBdown,circuit.ZCdown]=CalcZs(X,Y,circuit,...
    Mylegend,'down','calc',1);   %Down state
[ZA,circuit.ZBup,circuit.ZCup]=CalcZs(X,Y,circuit,Mylegend,...
    'up','use',0);                  %Up state
[circuit.S21down]=CalcS21(X,Y,circuit,Mylegend,'down',1);
[circuit.S21down]=CalcS21(X,Y,circuit,Mylegend,'up',1);
%[circuit.S11]=CalcS11(X,Y,circuit,Mylegend,'down',1);
[circuit.S11]=CalcS11(X,Y,circuit,Mylegend,'up',1);
```

```
function [ZA,ZB,ZC]=CalcZs(X,Y,circuit,mylegend,state,para,myplot)
% Calculate the impedanse of the different terms
%   state   = determines if switch is 'down' or 'up'
%   para    = determines if R,C,L is calculated 'calc' or if
%             specified parametes are used 'use'
%   myplot  = Plot figures "1" or not "0"

%Assign variables
f=circuit.f;

Rl=circuit.Rl;
L=circuit.L;
Rc=circuit.Rc;
Cs=circuit.Cs;
Cgdown=circuit.Cgdown;
Cgup=circuit.Cgup;

%Calculate variables
omega=2*pi*f;

%ZA
```

```
if strcmp(para,'calc')
        [Rl]=CalcRl(X,Y,circuit,mylegend,myplot)
end
ZA=Rl+i*omega.*L;

%ZB
trans=X;
trans(:)=1;
if strcmp(state,'down')
    ZB=Rc.*trans;
elseif strcmp(state,'up')
    ZB=1./(omega.*Cs);
end

%ZC
if strcmp(state,'down')
    ZC=1./(i*omega.*Cgdown);
elseif strcmp(state,'up')
    ZC=1./(i*omega.*Cgup);
end

%Plot
if myplot==1
    %ZA
    myxlabel='Frequency [GHz]';
    myzlabel='Z_A [\Omega]';
    myxlim=[0 25];
    myzlim=[0 1];
    figure
    plot3(Si2G(X)',Y',ZA');
    view(0,0)
    box on
    xlabel(myxlabel)
    zlabel(myzlabel)
    xlim(myxlim)
    %zlim(myzlim)
    %legend(mylegend,'location', 'West')

    %ZB
    myxlabel='Frequency [GHz]';
    myzlabel='Z_B [\Omega]';
    myxlim=[0 25];
    myzlim=[0 1];

    figure
    plot3(Si2G(X)',Y',ZB');
    view(0,0)
    box on
    xlabel(myxlabel)
```

```
    zlabel(myzlabel)
    xlim(myxlim)
    %zlim(myzlim)
    %legend(mylegend,'location', 'West')
end
```

```
function [Rl]=CalcRl(X,Y,circuit,mylegend,myplot)
% Calculates the series resistance of beam

%Assign variables
f=circuit.f;

tm=circuit.tm;
w=circuit.w;
cw=circuit.cw;
l=circuit.l;
sigma=circuit.sigma;

%Calculate parameters
[△]=CalcSkinEffect(X,Y,circuit,mylegend,1)

%Calculate
trans=X;
trans(:)=1;

R=l./(sigma.*w.*tm*2).*trans
Rsk=(cw.*l)./(sigma.*w.*△*2)

index=find(Rsk>R);              %Find instances where Rsk>R
Rl=R;
Rl(index)=Rsk(index);           %Replace these instances with Rsk

%Plot%Plot
if myplot==1
    myxlabel='Frequency [GHz]';
    myzlabel='R_l [\Omega]';
    myxlim=[0 25];
    myzlim=[0 0.25];

    figure
    plot3(Si2G(X)',Y',Rl');
    view(0,0)
    box on
    xlabel(myxlabel)
    zlabel(myzlabel)
    xlim(myxlim)
    zlim(myzlim)
```

```
    legend(mylegend,'location', 'NorthWest')
end
```

```
function [S21]=CalcS21(X,Y,circuit,mylegend,state,myplot)
% Calculate the term S_21
%   state   = determines if switch is 'down' or 'up'

%Assign variables
ZA=circuit.ZA;
if strcmp(state,'down')
    ZB=circuit.ZBdown;
    ZC=circuit.ZCdown;

    myzlabel='Insertion loss, S_{21} [dB]';
    myxlim=[0 25];
    myzlim=[-0.5 0];
    pos='SouthWest';
elseif strcmp(state,'up')
    ZB=circuit.ZBup;
    ZC=circuit.ZCup;

    myzlabel='Isolation, S_{21} [dB]';
    myxlim=[0 25];
    myzlim=[-40 0];
    pos='NorthWest';
end
Z0=circuit.Z0;

%Calculate
S21num=2;
S21den1=((ZA+ZB+Z0)./ZC);
S21den2=((ZA+ZB+(ZA.*ZB)./ZC)./Z0);

S21den=2+S21den1+S21den2;
S21=S21num./S21den;
magS21=abs(S21);

%Plot the calculated data as a function of l2/ltot
if myplot==1
    figure
    plot3(Si2G(X)',Y',num2dB(magS21)');
    view(0,0)
    box on
    xlabel('Frequency [GHz]')
    zlabel(myzlabel)
    xlim(myxlim)
    zlim(myzlim)
```

```
    legend(mylegend,'location', pos)
end
```

Bibliography

[1] Wikipedia - the free encyclopedia. www.wikipedia.org.

[2] N. Agraït. Quantum properties of atomic-sized conductors. *Physics Reports*, 377:81–279, 2003.

[3] I. Bahl and P. Bhartia. *Microwave Solid State Circuit Design*. Wiley, 2003.

[4] J. Bouchaud and H. Wicht. RF MEMS: Status of the industry and roadmaps. *2005 IEEE Radio Frequency Integrated Circuits Symposium*, pages 379–384, 2005.

[5] S.A. Campbell. *The Science and Engineering of Microelectronic*. Springer, 1967.

[6] W.R. Chang. An elastic-plastic contact model for a rough surface with an ion-plated soft metallic coating. *Wear*, 212:229–237, 2004.

[7] Ansoft Corperation. Ansoft Maxwell HFSS. www.ansoft.com.

[8] Coventor Inc. *CoventorWare Analyzer-Reference*, 2006 edition.

[9] Coventor Inc. *CoventorWare Architect-Reference*, 2005 rev b edition.

[10] A. Mikrajuddin et al. Size-dependant electrical constriction resistance for contacts of arbitrary size: from Sharvin to Holm limits. *Material Science in Semiconductor Processing*, 2, 1999.

[11] A.Q. Liu et al. Low-loss lateral micromachined switches for high frequency applications. *Journal of Micromechanics and Microengineering*, 15:157–167, 2005.

[12] H. Lee et al. Characterization of metal and metal alloy films as contact materials in MEMS switches. *Journal of micromechanics and microengineering*, 16:557–563, 2006.

[13] H.J. De Lo Santos et al. RF MEMS for Ubiquitous Wireless Connectivity: Part 2-Application. *IEEE Microwave Magazine*, December 2004.

[14] J. Oberhammer et al. Mechanically tri-stable in-line single-pole-double-through all-metal switch. *IEEE Micro Electro Mechanical Systems 2006, Istanbul, Turkey*, pages 898–901, 2006.

[15] J.A. Greenwood et al. Contact of nominally flat surfaces. *Proceedings of the Royal Society of London*, A:295, 1966.

[16] M. Tang et al. A new approach of lateral RF MEMS switch. *Analog Integrated Circuits and Signal Processing*, 40:165–173, 2004.

[17] R. Legtenberg et al. Electrostatic curved electrode actuators. *Journal of microelectromechanical systems*, 6, September 1997.

[18] R.A. Coutu Jr et al. Micro-switches with sputtered Au, AuPd, Au-on-AuPt and AuPtCu alloy electric contacts. *Proceedings of the 50th IEEE Holm Conference on Electrical Contacts and the 22nd International Conference on Electrical Contacts*, pages 214–221, 2004.

[19] S. Majumder et al. Study of contacts in a electrostatically actuated microswitch. *Sensors and Actuators A*, 93:19–26, 2001.

[20] S. Majumder et al. Adhesion and contact resistance in an electrostatic mems microswitch. *Micro Electro Mechanical Systems, 2005. MEMS 2005. 18th IEEE International Conference on MEMS*, pages 215–218, 2005.

[21] T. Veijola et al. Equivalent-circuit model of the squeezed gas film in a silicon accelerometer. *Sensors and Actuators A*, 45:239–248, 1995.

[22] V.K. Varadan et. al. *RF MEMS and their applications*. Wiley, 2003.

[23] W.R. Chang et al. An elastic-plastic model for the contact of rough surfaces. *Journal of Tribology*, 109:257–263, 1988.

[24] J.M. Gere and S.P. Timoshenko. *Mechanics of materials*. Chapman & Hall, 1991.

[25] R. Holm. *Electric Contacts: Theory and Application*. Springer, 1967.

[26] D. Hyman and M. Mehregany. Contact Physics of Gold Microcontacts for MEMS Switches. *IEEE Transactions on components and packaging technology*, 3, 1999.

[27] Coventor Inc. CoventorWare, version 2005. www.coventor.com.

[28] R. Jones and M. Chapman. RF MEMS in mobile phones. *www.rfdesign.com*, September 2005.

[29] E.J.J. Kruglick. Lateral MEMS microcontact considerations. *Journal of micromechanical systems*, 8:264–271, 1999.

[30] R. Ludwig and P. Bretchko. *RF Circuit Design: Theory and Applications*. Wiley, 2003.

[31] MEMScAP. *SOIMUMPs - Design Handbook*, rev 4.0 edition.

[32] W. E. Newell. Miniaturization of tuning forks. *Science*, 161:1320–1326, 1968.

[33] J. Oberhammer. *Novel RF MEMS switch and packaging concept*. PhD thesis, Royal Institute of Technology (KTH), 2004.

[34] D. Peroulis. *RF MEMS devices for multifunctional integrated circuits and antennas*. PhD thesis, The University of Michigan, 2003.

[35] S.S. Rao. *Mechanical vibrations*. Addison-Wesley Publishing Company, 1995.

[36] G.M. Rebeiz. RF MEMS Switches: Status of the technology. *Transducers 03. The 12th International Conference on Solid State Sensors, Actuators and Microsystems*, 2003.

[37] G.M. Rebeiz. *RF MEMS Theory, Design and Technology*. Wiley, 2003.

[38] G.M. Rebeiz. One day-short course on RF MEMS: Switches, varactors and their applications. IMAPS, Norway, September 2005.

[39] J. B. Rizk. *W-Band RF MEMS Switches, Phase Shifters and Antennas*. PhD thesis, The University of Michigan, 2003.

[40] M. H. Sadd and A. K. Stiffler. Squeeze film dampers: Amplitude effects at low squeeze numbers. *Trans. ASME*, pages 1366–1370, 1975.

[41] S.D. Senturia. *Microsystem Design*. Springer, 2001.

[42] Tronic's Microsystems. http://www.tronics-mst.com/memsoi.html.

[43] G.U. Jensen U. Hanke, A.M. Bøifot. IRRFT - Integrated Reconfigurable Radio Front-end Technology. Assesment of RF-performance for various capacitive switches. SINTEF Memo.

[44] G. Wexler. The size effect and the non-local boltzmann transport equation in orifice and disk geometry. *Proceedings of the Royal Society*, 89, 1966.

[45] W.C. Young and R. Budynas. *Roark's Formulas for Stress and Strain*. McGrawHill, 2002.